University of Stuttgart

Institute of Geodesy

Exploring the performances of SAR altimetry and improvements offered by fully focused SAR

Master Thesis

Geodesy and Geoinformatics

University of Stuttgart

Yuwei Wu

Stuttgart, November 2021

Supervisors: Dr.-Ing. Mohammad Tourian
University of Stuttgart

M.Sc. Sajedeh Behnia
University of Stuttgart

Erklärung der Urheberschaft

Ich erkläre hiermit an Eides statt, dass ich die vorliegende Arbeit ohne Hilfe Dritter und ohne Benutzung anderer als der angegebenen Hilfsmittel angefertigt habe; die aus fremden Quellen direkt oder indirekt übernommenen Gedanken sind als solche kenntlich gemacht. Die Arbeit wurde bisher in gleicher oder ähnlicher Form in keiner anderen Prüfungsbehörde vorgelegt und auch noch nicht veröffentlicht.

Ort, Datum Unterschrift

Abstract

With development of the altimetry techniques, the measurement principle has been changed from conventional pulse-limited principle to the delay-Doppler principle since CryoSat-2. The delay-Doppler altimetry presents scientists with the chance to develop new processing schemes and improve products that maximize the benefits of the measurements. Nevertheless, one of the challenges for delay-Doppler Altimetry lies in the complexity of the post-processing, especially the Delay-Doppler processing.

The focus of this thesis is to better understand delay-Doppler and fully focused SAR altimetry. This thesis compares the retrieved waveforms and resultant water level time series with different altimetry principles, processing options and retracking methods. By using platform SARvatore for delay-Doppler altimetry and SMAP for fully focused SAR altimetry, different processing options (data posting rate, Hamming window and zero padding) and different retrackers (SAMOSA family for SARvatore, PTR for SMAP) can be applied and compared.

Our results reveal that the waveforms generated by different configurations have different peaks for SARvatore. For SMAP, with or without zero padding or Hamming window had very little impact, with more differences mainly coming from the different retracking methods. Our results also show that fully focused SAR does not bring a significant improvement when applied to Sentinel-3 data.

In summary, different configurations and retracking methods can significantly affect the shape of waveforms and their derived ranges. According to this thesis's experiments, the configuration with 80 Hz data posting rate, Hamming window, zero padding, extended receiving window and retracker SAMOSA++ offers the best performance.

Contents

List of Figures

List of Tables

Chapter 1

Introduction

1.1 Motivation

With development of the altimetry techniques, the measurement principle has been changed from conventional pulse-limited principle to the delay-Doppler principle since CryoSat-2. The delay-Doppler altimetry begins a new generation in the altimetry community and presents scientists with the chance to develop new processing schemes and improve products that maximize the benefits of the measurements. Nevertheless, one of the challenges for delay-Doppler Altimetry lies in the complexity of the post-processing, especially the Delay-Doppler processing. This is mainly due to the fact that different ways of performing options lead to different waveforms and, therefore, different retracking results. Moreover, different platforms such SARvatore and DeDop have different algorithms for processing and they could differ in terms of their performances.

The focus of this thesis is to better understand delay-Doppler and fully focused synthetic aperture radar (FF-SAR) altimetry. Various processing options are compared and contrasted over different case studies in terms of the retrieved waveform, retracking method, and the resultant water level time series.

1.2 Satellite Altimetry

1.2.1 Altimetry Principles

Altimetry satellites such as CryoSat-2 and Sentinel-3 are equipped with radar altimeters, which can measure the distance between the satellite and the surface of the Earth.

In general, the altimeter contains a nadir-looking antenna, which can transmit radar signals to the Earth at a high frequency. Once the signal reaches to the surface of the Earth, it can be reflected back to the altimeter. The altimeter measures the elapsed time Δt of the round trip between the satellite and the surface. Thus the range, the distance of the satellite to the surface, can be derived roughly as:

$$\hat{\rho} = c \cdot \frac{\Delta t}{2} \tag{1.1}$$

where c is the light speed. However, the radar signals can be decelerated as they travel through the atmosphere, causing significant error in the obtained range. To calculate the signal propagation error, the altimeters of CryoSat-2 and Sentinel-3 comprise two frequencies for range

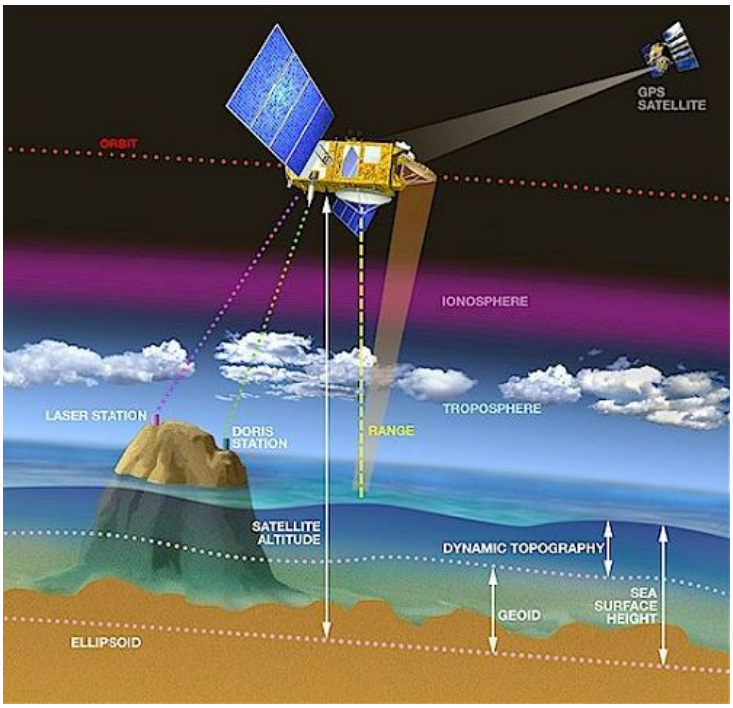

Figure 1.1: *Altimetry Principle [Credit: CNES/D. Ducros]*

measurements, namely the Ku-band (13.575 GHz, bandwidth 350 MHz) and the C-band (5.41 GHz, bandwidth 320 MHz). Additionally, there are also instrumental errors and geophysical disturbances that must be eliminated. The corrected range ρ is obtained by removing all these errors from measured range. With the help of the GNSS and DORIS sensors onboard, the precise orbit altitude of the satellite to the reference surface can be determined. Furthermore, the sea surface height can be therefore derived from the corrected range and the orbit altitude h by:

$$H = h - \rho \tag{1.2}$$

The slant-range resolution is given by:

$$\delta_{SR} = \frac{c\tau}{2} \tag{1.3}$$

where τ is the pulse duration. With the slant-range resolution and look angle of the altimeter, the ground-range resolution which we generally refer as the spatial resolution, can be calculated. For radar altimetry, the pulse compression is used to improve the range resolution by processing the transmitted relatively long pulse in a way that is equivalent to the effective short pulse. The radar system uses chirp signals to overcome the limitation that oscillators cannot generate echoes with sufficient power to reach the ground in a short period of time. The chirp signal is a frequency modulated (FM) signal. By using the chirp signal, the resolution is no longer determined by pulse duration τ but by bandwidth B.

For conventional altimetry, the altimeter transmits a pulse with known power toward the surface and receives a certain power as the signal returns. The pulse leaves the antenna as a widening beam, becoming ever wider the farther it travels. The returned power in time, the

"waveform", is sampled in a tracking window. The information about range can be derived from the waveform. To better understand the shape of a waveform, the four processes of waveform formation are introduced step by step.

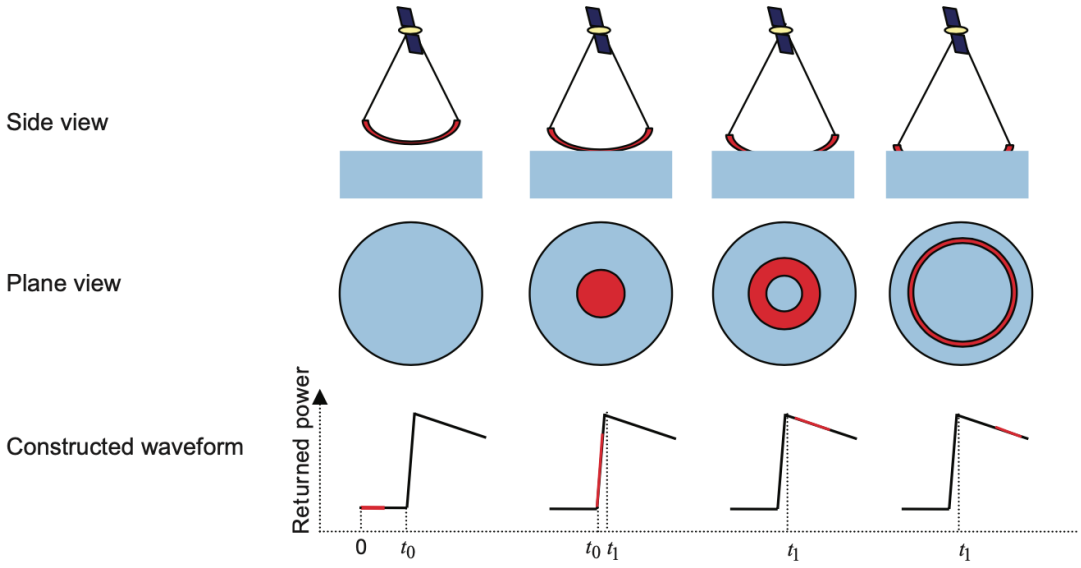

Figure 1.2: *Waveform Formation [Tourian, 2012]*

When the altimeter emits the pulse and the tracking system is activated, a low power noise is received as a result of the parasite reflection of the pulse in the ionosphere and atmosphere and the instrument electronic noise within $0 < t < t_0$. Then the wavefront reaches the surface at $t = t_0$. The pulse illuminates a point and the tracker begins to receive the returned power. During $t_0 < t < t_1$, the returned signal rises up, while the footprint at the surface being a disc spreads with time. This power rise in the tracking window is known as "leading edge." At time point $t = t_1$, the return power increases up to a maximum and the trailing part of the signal begins to hit the surface. During $t > t_1$, the tail of the pulse continues to reach the ground, making a circular ring footprint. The footprint continues to grow larger and thinner over time until it finally vanishes. At the same time, the received power will also gradually become lower with time, exhibiting a descending trend in the waveform.

1.2.2 Retracking

In order to derive range from altimetry measurements, it is required that the true leading edge is identified and located as accurately as possible. This is partially done via the concept of on-board tracking: on reception, the satellite tries to position the leading edge of a waveform onto a specific bin, the tracking bin. However, the tracker range is not precise enough with less calculation time and less information. The preciser range is obtained by the post-processing, which is retracking.

Waveform retracking is the process of calculating geophysical quantities from a waveform. These quantities includes the final altimeter range, backscatter coefficient, wind speed over the ocean and significant wave height (SWH). Because different waveforms over the water

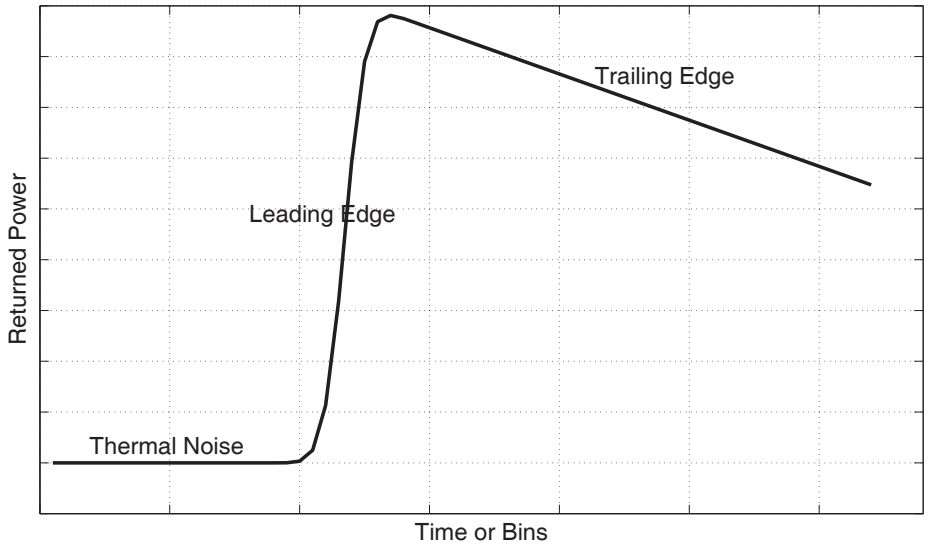

Figure 1.3: *Schematic Altimeter Mean Return Waveform over Ocean Surface [Tourian, 2012]*

surface produce different types of patterns, various algorithms are applied for the calculation of these geophysical quantities. In general, retracking algorithms can be divided into three broad branches [Dinardo, 2020]:

- empirical retracking
- physically-based retracking
- statistical retracking

The empirical retracker calculates parameters based on heuristics that are defined based on retrospective experience or a "guess and try" approach. This is generally applicable in cases where it is difficult to build theoretical models. On the other hand, physically-based retrackers are founded on waveform models, which are usually defined by the characteristics of the sensor and the signal as well as the shape of the waveform itself. In physically-based retracking, the mean returned power waveform $P(t)$ can be expressed as a convolution [Brown, 1977]:

$$P(t) = P_{fs}(t) * q_s(t) * P_{PTR}(t) \tag{1.4}$$

where t is the satellite receiver's time, $P_{fs}(t)$ is the flat surface impulse response, $q_s(t)$ is the surface elevation probability density function (PDF) of specular points within the altimeter footprint, and $PTR(t)$ is the system point target response (PTR) [Brown, 1977; Deng and of Technology. Dept. of Spatial Sciences, 2003]. The physically-based model can be classified downwards according to whether the waveform model is obtained purely numerically or by analysis. Analytical models are more robust, more versatile, and faster than numerical models, because analytical models are closed models under the necessary assumptions and approximations, whereas numerical models are usually more complex [Dinardo, 2020]. Finally, the statistical retrackers define the geophysical quantities by minimizing or maximizing the statistical properties of a set of consecutive waveforms.

1.3 SAR Altimetry Missions

1.3.1 CryoSat-2

CryoSat-2 is the follow-up to the Earth Explorer Opportunity Mission in the European Space Agency's (ESA) Living Planet Programme. The successor to the CryoSat, whose launch failed on October 8, 2005. CryoSat-2 was selected for development in 1999, and was launched on April 8, 2010. The satellite is located at an altitude of 717 km with an inclination of 92° and has a 369 day repeat cycle.

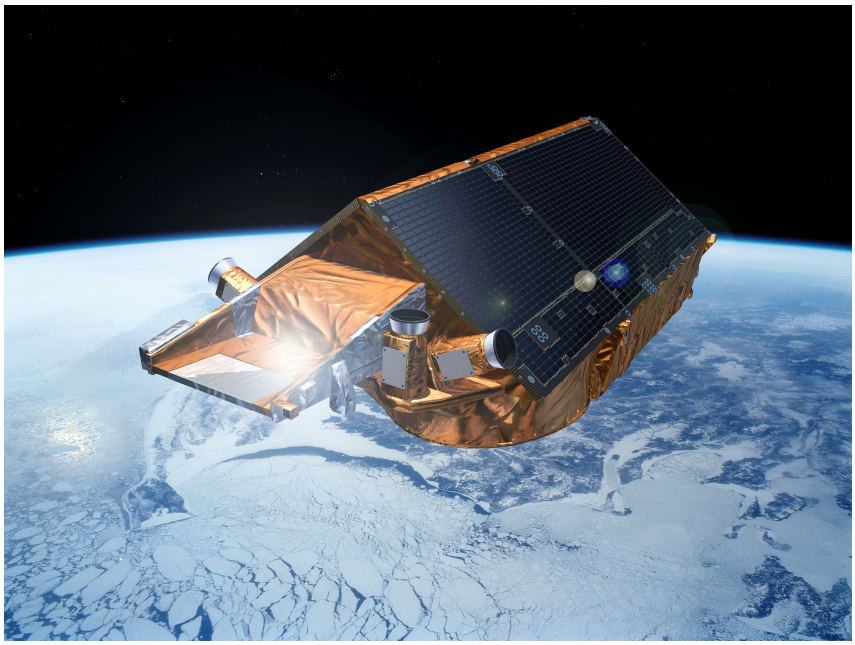

Figure 1.4: *CryoSat in Orbit [*earth online —ESA, *2021]*

CryoSat-2 aims to monitor the thickness of land ice and the most dynamic parts of the Earth's cryosphere and sea ice. It employs synthetic aperture radar (SAR) and interferometry techniques from standard imaging radar missions to improve its accuracy over rugged ice sheet margins and sea ice in polar waters. CryoSat-2 measures the height difference between sea ice and adjacent waters as well as the ice height, and it tracks changes in ice thickness. The measured data help to understand the link between the melting of polar ice and sea level rise, which are significant impacts to climate change.

The SAR interferometric radar altimeter (SIRAL) is the primary instrument on CryoSat and has the capability to meet the measurement requirements for ice height and sea ice freeboard. The SIRAL instrument contains a conventional pulse-limited radar altimeter and a second antenna with synthetic aperture and interferometric signal processing. SIRAL is able to operate in three modes: low resolution mode (LRM), in other words, pulse-limited operation; SAR and SAR interferometry (SARIn or SIN) burst mode [*earth online —ESA*, 2021].

Over the ice sheet gaps and oceans, CryoSat-2 generally operates as a traditional radar altimeter in LRM. In this mode, the pulse repetition frequency (PRF) is limited to 2 kHz and, therefore, LRM has a lower data rate compared to the other two modes Bouzinac et al. [2019]. PRF reffers

to the transmission interval of the pulses. The SAR mode is used over sea ice and a few oceanographic areas. It emits bursts of pulses with PRF of 20 kHz and uses SAR processing to obtain better spatial resolution than LRM. The footprint on the surface is a rectangle of 250 m $\times$ 80 m. SIRAL can operate as an interferometer by using the second antenna. The origin of the echo can be obtained by comparing the different paths of the signal returning to the two antennas [Bouzinac et al., 2019]. Therefore, the SARIn mode is used around the ice sheet margins with slopes and over mountain glaciers.

CryoSat-2 achieved its main mission goals in the cryosphere. The mission provided evidence for the advanced performance of SAR mode altimetry over the ocean (leading to Copernicus Sentinel-3 operating globally in SAR mode). In the past two years, the CryoSat-2 mission has shifted its goal to maintain a time series of unique climate records across the cryosphere and to present attractive scientific and technical objectivess in the fields of swath processing, polar oceanography, cryosphere meteorology, and so on [*earth online —ESA*, 2021].

1.3.2 Sentinel-3

Sentinel-3 is a European Earth observation satellite mission developed to measure sea-surface topography, sea- and land-surface temperatures, and ocean- and land-surface colors with high accuracy and reliability [*Sentinel Online —ESA*, 2021]. Sentinel-3 is composed of two satellites: Sentinel-3A and Sentinel-3B. Sentinel-3A was launched on February 16, 2016, while Sentinel-3B was launched on April 25, 2018. In January 2016, Sentinel-3C and Sentinel-3D joined the program, with Sentinel-3C expected to launch in 2023 [*THE CEOS DATABASE*, 2021]. For optimal coverage, Sentinel-3 is placed in a near-polar, sun-synchronous orbit with a high inclination of 98.65° at the altitude of 814.5 km and has a repeat cycle of 27 days. The orbits of the two satellites are the same, with a phase difference of 140°. The spacecraft is composed of four main instruments:

-ocean and land color instrument (OLCI),
-sea and land surface temperature instrument (SLSTR),
-SAR radar altimeter (SRAL), and
-microwave radiometer (MWR).

OLCI is inherited from Envisat's medium-resolution imaging spectrometer. It is a push-broom imaging spectrometer with five cameras and 21 bands, designed to provide a direct view of the Earth and to monitor ocean conditions and coastal zones. SLSTR is an along-track scanning radiometer developed to retrieve sea surface skin temperatures on a global scale [ESA, 2012]. SRAL is the core instrument of the Sentinel-3 derived from ENVISAT RA-2, CryoSat SIRAL and Jason-2/Posedion-3 heritage, and is seeks to provide range measurements over different types of surfaces. MWR is designed to correct for travel delays of SRAL signals caused by tropospheric water content.

In addition to the main instruments, a Global Navigation Satellite System (GNSS) instrument, a Doppler Orbit determination and Radio-positioning Integrated on Satellite (DORIS) instrument (Sentinel-3A only), and a laser retro reflector are used to determine a precise orbit.

The SRAL can operate in two modes: LRM and SAR mode. Compared to LRM, the SAR mode provides a higher along-track resolution using the delay-Doppler concept [Raney, 1998]. In

Figure 1.5: *Sentinel-3 Satellite and Payloads [Credit: ESA]*

LRM, SRAL operates as a conventional pulse-limited altimeter at a PRF of 1920 Hz with a pattern containing a sequence of six Ku-band pulses (13.6 GHz) and one C-band pulse (5.3 GHz). For a radar cycle of 50 ms, there are 16 patterns, in other words, a total of 84 Ku-band pulses and 14 C-band pulses. In SAR mode, SRAL emits pulses at PRF of 18 kHz. Every 64 Ku-band pulses forms a burst, which is surrounded by two C-band pulses. The duration of the burst cycle is about 12.5 ms, so four burst cycles are equal to an LRM cycle of 50 ms [*Sentinel Online —ESA*, 2021].

1.3.3 Sentinel-6

The Copernicus Sentinel-6 mission continues the Jason satellites' decades-long series of sea level measurement and sea state monitoring until at least 2030. Sentinel 6 stands on the heritage of the Jason series, ESA's CryoSat satellite, and the Copernicus Sentinel-3 mission. The Sentinel-6 mission comprises two identical satellites: Sentinel-6 Michael Freilich launched on November 21, 2020, and Sentinel-6B, to be launched in 2025. The satellites are located in a polar orbit at an altitude of 1,336 km with an inclination of 66°. This orbit allows the mapping for 95% of the Earth's ice-free oceans every 10 days [*Sentinel6 - ESA*, 2021].

The payload for each Sentinel-6 satellite includes a precise orbit determination (POD) suite (GNSS, DORIS, and LRA), a microwave radiometer, and the Poseidon-4 dual frequency (C/Ku-band) nadir-pointing radar altimeter, which enables centimeter-level determination of the sea surface height.

Poseidon-4 is a nadir-pointing dual-C/Ku-band frequency SAR altimeter (only the Ku-band operates in SAR), which includes nine separate measurement modes using two chronograms: an acquisition chronogram and an interleaved chronogram [Donlon et al., 2021]. The interleaved chronogram operates in an open burst configuration with a PRF of 9 kHz. The interleaved (open burst) transmit-and-receive approach means that twice as many samples are available compared to the Sentinel-3 radar altimeter SARL, allowing for a significant improvement in the noise characteristics of the altimeter [Donlon et al., 2021].

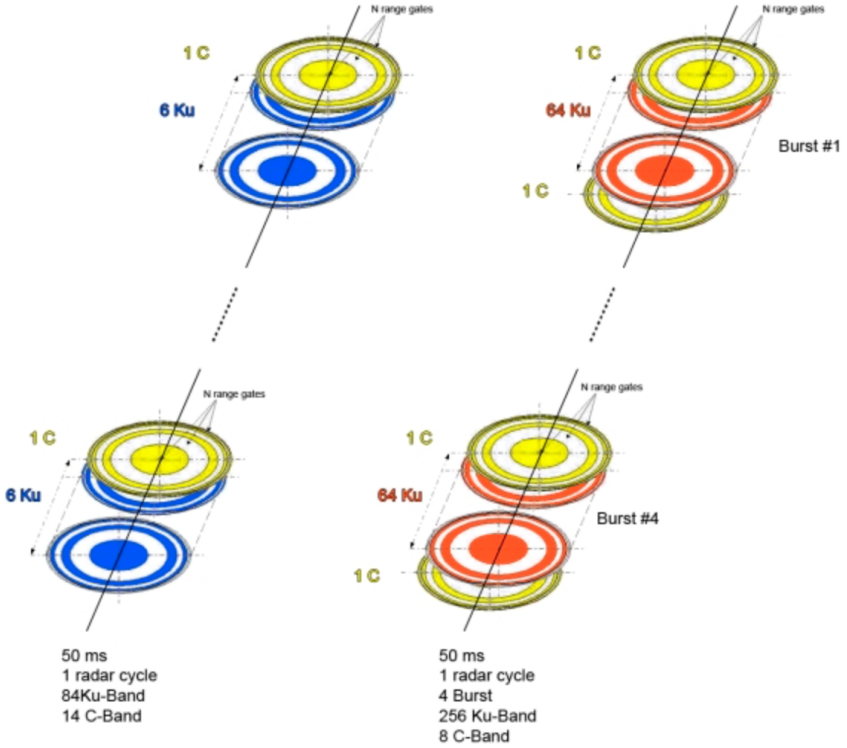

Figure 1.6: *LRM Radar Cycle Transmitting Pattern (left) and SAR Radar Cycle Transmitting Pattern (right) for Sentinel-3 [Credit: Thales Alenia Spazio]*

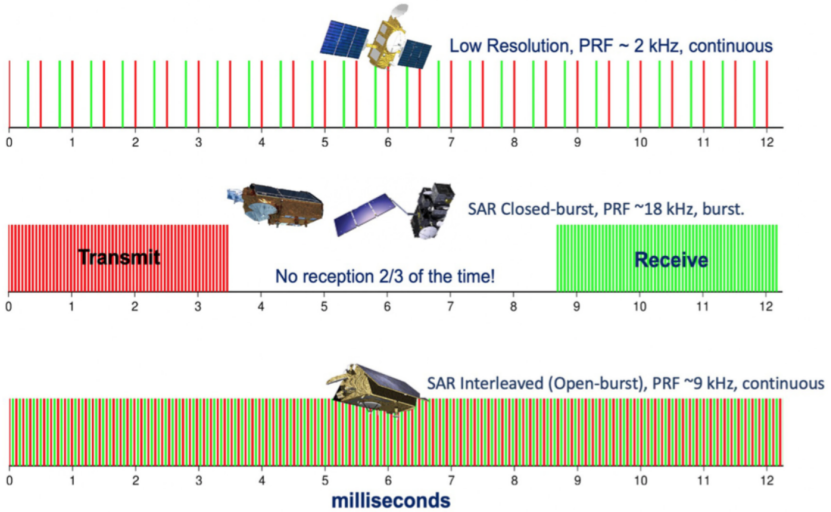

Figure 1.7: *Evolution of Satellite Radar Altimeter Chronograms [Donlon et al., 2021]*

The PRF of Poseidon-4 is adjusted along the orbit with the help of the satellite vertical velocity derived from the DORIS instrument. The worst case scenario for each tracking cycle (50 ms) is an altitude change of 2.5 m. The use of the interleaved chronogram allows SAR mode and LRM heritage acquisitions to run simultaneously to ensure that the introduction of SAR technology into the reference does not introduce bias into the long-term sea-level climate record derived from LRM measurements alone [Donlon et al., 2021].

1.4 Processing Levels and Product Types

Sentinel-3 altimetry data is released at different levels:
-Level-0 is the raw telemetered data, geolocated and dated;
-Level-1 is the corrected data for instrumental and geometrical effects based on Level-0 data; and
-Level-2 is the Level-1 data corrected for geophysical effects.

Level-0

Level-0 processing has two main functions: One is to extract the raw data provided by the instrument source packet in instrumental engineering units and to convert them to international system units. The second function of the Level-0 processing chain is to correct the date and time of the measurement data and to provide the satellite position and the measurement position on the Earth's surface that correspond to the measurement data.

The Level-0 product is an internal product only. It is not available to users and is used only as an input to Level-1 processing.

Level-1

The input data for Level-1 processing are the Level-0 product. The primary functions of the Level-1 processing chain are to apply calibration and geometrical corrections, calculate the tracker range and the sigma0 scaling factor, and derive the waveform.

Specifically, there are three types of Level-1 products provided by the ESA: Level-1A products, Level-1BS products and Level-1B products. The Level-1A products contain geo-located and fully calibrated complex echoes for subsequent data processing, while Level-1BS products contain fully SAR-processed and range aligned complex echoes but without multilooking. Level-1B products contain the same variables as Level-1BS, except for complex in-phase and quadrature echoes and the part about stack characteristics.

In general, the processing of Level-1A to Level-1B consists mainly of all processes starting from the raw telemetered data to build a waveform from a certain illuminated surface.

Level-2

The input data to Level-2 processing are the Level-1 product. The main function of the Level-2 processing chain is to perform retracking to the output waveforms of Level-1 processing, and to compute physical parameters including the retracked altimeter range, backscatter coefficient, and significant wave height.

There are two types of Level-2 products according to the surface covered: water (WAT) and land (LAN) products. The processing algorithm is identical; only the geographical coverage is different.

1.5 Case Study

Itaparica

Itaparica, also known as Luiz Gonzaga, is a reservoir in the middle course of the São Francisco River. It is located in the east of Brazil, 290 km from the Atlantic Ocean, with an area of 834 km^2 and a water storage capacity of approximately 11 billion m^3 [Melo et al., 2016]. The reservoir is the achievement of the construction of the Itaparica Dam in 1988, which has hydroelectric power generation as its main purpose.

The in situ data for Itaparica are from the National Water Agency (ANA) of Brazil. The monitoring station Uhe Luiz Gonzaga (Itaparica) Barramento is located at 9.14°S, 38.31°W with the code number 49042580. The distance between virtual station and in situ station is about 31 km.

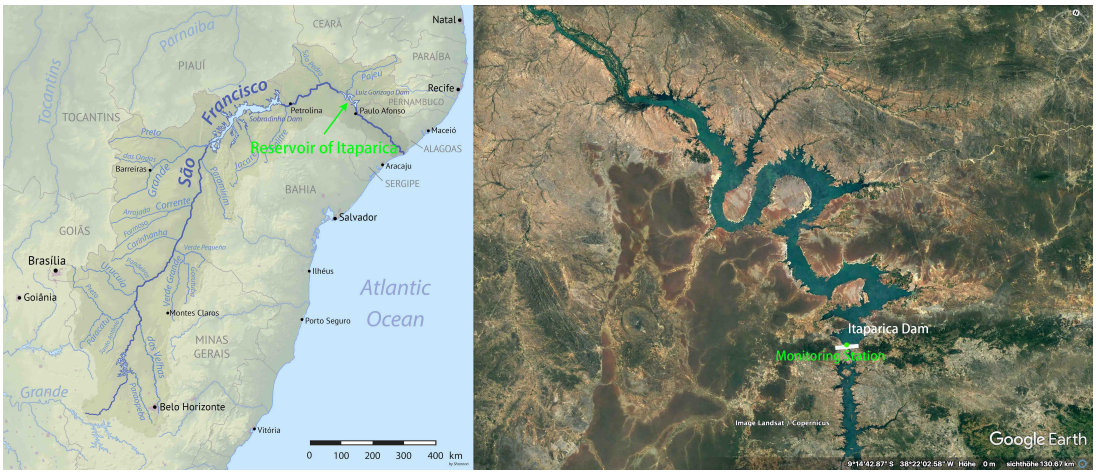

Figure 1.8: *Reservoir of Itaparica [left: Wikipedia© 2021 right: Google Earth© 2021]*

Mississippi

The Mississippi River, located in south-central North America, is the largest water system in North America, with a basin area of about 3 million km^2. Addtionally, it is the longest river in North America, with its source at Lake Itaska in northwestern Minnesota, United States, at an elevation of 446 m. It flows through the central Great Plains and southward into the Gulf of Mexico, with a total length of 3,767 km.

The in situ data for the Mississippi River are retrieved from the United States Geological Survey (USGS). The selected monitoring station is located in Baton Rouge, a city in southeastern Louisiana, on the south bank of the Mississippi River, 250 km from the Gulf of Mexico. The monitoring station is located at 30.44°N, 91.19°W with the code number 07374000. The distance between virtual station and in situ station is about 9 km.

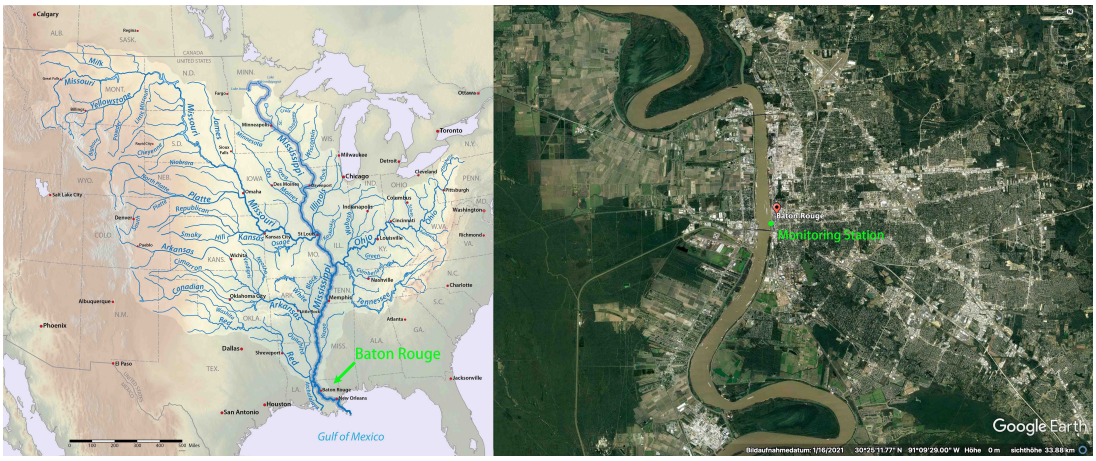

Figure 1.9: *Baton Rouge by the Mississippi River [left: Wikipedia© 2021 right: Google Earth© 2021]*

São Francisco

The São Francisco River is the fourth largest water system in South America and the longest of all rivers in Brazil; it is named after St. Francis of Assisi. It originates in Minas Gerais and flows northward, turning eastward near Pernambuco and Bahia, and finally emptying into the Atlantic Ocean. The river has a total length of 2,830 km and a basin area of 641,000 km^2.

The in situ data are obtained also from the National Water Agency of Brazil. The monitoring station Uhe Sobradinho Montante 4 is located in São Francisco, Minas Gerais, Brasilien, at 15.95°S, 44.87°W and with the code number 44190900. The distance between virtual station and in situ station is 226 m.

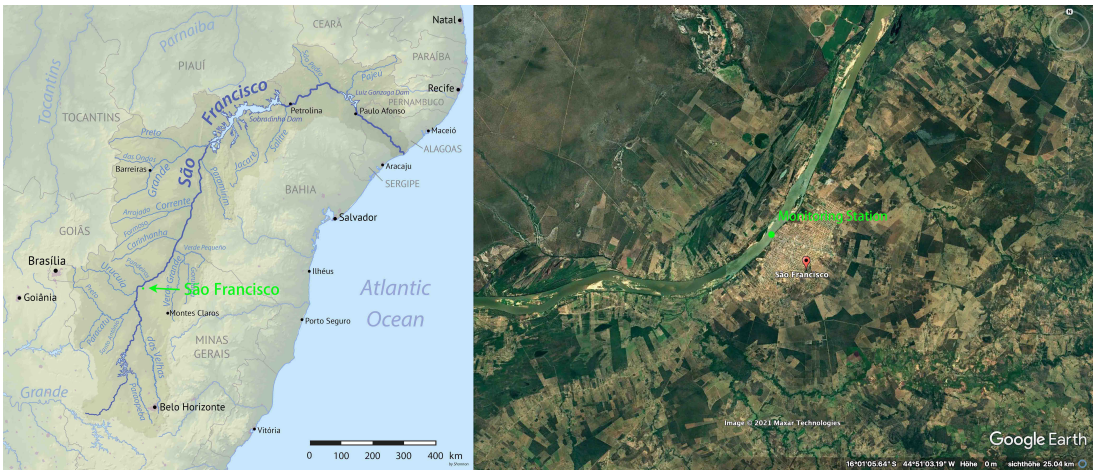

Figure 1.10: *São Francisco by the São Francisco River [left: Wikipedia© 2021 right: Google Earth© 2021]*

Chapter 2

Delay Doppler Altimetry

2.1 Introduction

In conventional pulse-limited altimetry, the altimeter transmits and receives pulses in time sequences. The footprint on the surface goes from a point to a solid circle, after which it gradually becomes a circular ring and then eventually disappears. The waveform is constructed by averaging of the incoherent pulses to deal with inherent speckle noise [Cotton et al., 2008]. Disadvantages of traditional pulse-limited altimetry include the relative waste of radiated power, the fact that most of the radiated power falls outside the pulse-limited region and cannot be used for height estimation, and the dilation of the footprint over rougher terrain [Raney, 1998].

In terms of transmitted pulse, the main difference between conventional pulse-limited altimetry and delay Doppler altimetry is the PRF. For Sentinel-3, SRAL operates in the LRM mode at a PRF of 1920 Hz , while in SAR mode, the PRF is 18 kHz. The much higher PRF allows the pulses to be constructed in bursts, and the pulses within a burst to be correlated because the coherency allows for SAR processing. [*Sentinel Online —ESA*, 2021].

Unfocused SAR data processing should be performed where the altimeter synthesizes a large antenna as it flies forward by exploiting the Doppler characteristics of the return echoes. Delay Doppler altimetry uses delay compensation to reduce the size of the along-track footprint. The transmitted pulse is modulated and then the received signal is correlated with the transmitted pulse. The delays of the specific point on the surface are chosen from each corresponding burst and are summed to produce the waveform after the application of range compensation.

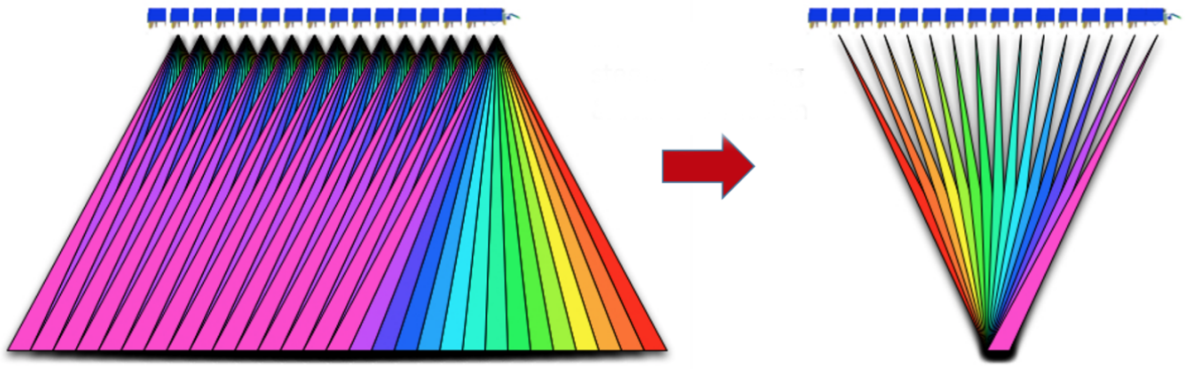

Figure 2.1: *Conceptual Representation of Beam-Steering Processing and Stack Formation for a Given Surface [Credit: ESA].*

In the case of Sentinel-3, the spatial resolution of the LRM mode in both along-track and across-track direction is 1.64 km [*Sentinel Online —ESA*, 2021]. However, in SAR mode using the delay-Doppler concept [Raney, 1998], the spatial resolution in the along-track direction rises to 300 m.

Figure 2.2 illustrates the waveform formation in delay Doppler altimetry. The red color represents the footprint of the conventional altimetry while the green color stands for delay Doppler altimetry. The first part of the figure indicates a case where the signal has not yet reached the surface. As with the situation of waveform formation of conventional altimetry, there is also a thermal noise. As the signal reaches the surface, the returned power arises sharply. The footprint is no longer as a circle but a narrow bin, which explains the sharper echo in the tracking window. Because of the beam stacking, the trailing edge is more concave than that seen in conventional altimetry.

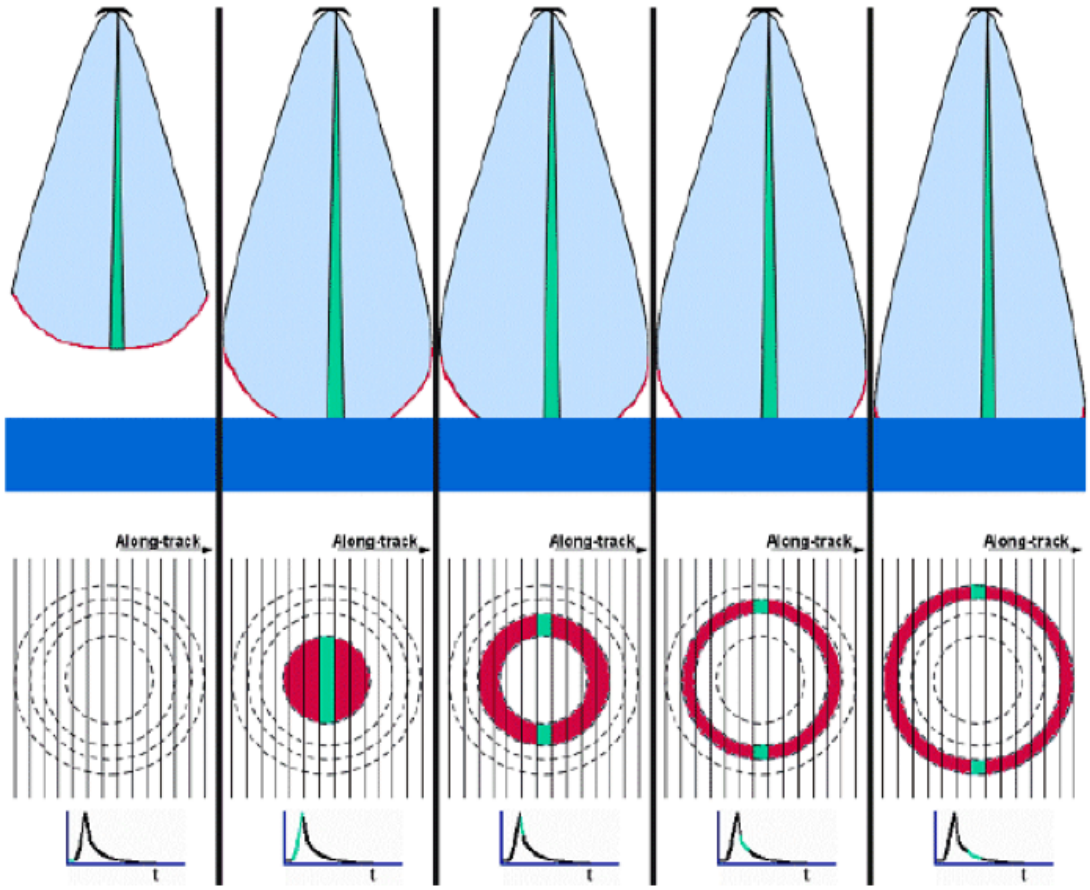

Figure 2.2: *Waveform Formation for SAR Altimetry [Credits: R.K. Raney, Johns Hopkins University Applied Physics Laboratory]*

2.2 Level-1B Processing

In general, Level-1B Processing contains all steps to build a waveform from the raw telemetered data. In the following lines, the details of processing from Level-1A to Level-1B are presented.

2.2.1 Calibration Correction

After extraction from the Level-1A data product, the received burst pulses must to be corrected.

There are five steps of corrections:
1. Computation of tracker ranges corrected for ultra-stable oscillator (USO) frequency drift: The on-board measured USO frequency drift is applied to the tracker range.

2. Computation of tracker ranges corrected for internal path correction: The travel difference between the transmission and the reference lines within the altimeter is applied to the tracker range.

3. Correction of the automatic gain control (AGC) for instrumental errors: AGC is a technique that uses the information from the previous signal level to adjust the gain in anticipation of the next signal. The aim is to ensure that the signal level remains as constant as possible [Bouzinac et al., 2019]. The instrumental error of AGC should be corrected and applied to the tracker range.

4. Correction of power and phase: The phase and power variations are applied to all echoes within the burst. These phase and power corrections are measured on-board through a sequence of calibration echoes in CAL1 calibration mode. [*Sentinel Online —ESA*, 2021].

5. Correction of the waveforms: The calibration mode CAL2 corrects Level-0 waveforms by the gain profile range window (GPRW) instrumental effects. The GPRW accounts for several instrumental effects (e.g., intermediate frequency filters gain response) that have an impact on the Level 0 waveform's power [*Sentinel Online —ESA*, 2021]. Both CAL1 and CAL2 activities are included in the Cyclic Monitoring Reports, which summaries the assessment of the altimeter instrument with a cyclic period of 27 days [*Sentinel Online —ESA*, 2021].

2.2.2 Determining Surface Locations

The purpose of this stage is to reference the measurements of the altimeter to surface locations along the satellite track. These surface positions correspond to the intersection of the Doppler beam with the surface elevation estimate. Based on the satellite Doppler resolution and the surface profile, the spacing between surface locations can be calculated. This prevents the surfaces from being oversampled or exhibiting gaps.

The first surface location is determined by the window delay associated with the first burst of the tracking cycle [Makhoul-Varona et al., 2020]. Then the algorithm is performed iteratively. First, the angular azimuth beam resolution θ is calculated as [Makhoul-Varona et al., 2020]:

$$\theta = \arcsin \frac{\lambda}{2|\mathbf{v_s}| \cdot \tau_B} \tag{2.1}$$

where τ_B is the burst duration, $\mathbf{v_s}$ is the satellite velocity vector and λ is the carrier wavelength. After the calculation of the angular azimuth beam resolution θ, the angles of sight α_i, which are between the nadir direction and the vector from satellite position to each burst surface position, are determined (in Figure 2.3 α_1 to α_3). Then, the processing is taken by comparing the α_i and θ until α_i is greater than θ. After that, the interpolation is performed between that determined surface location with α_j (in Figure 2.3, it refers to α_3) and the previous surface point of that determined surface location. In the case of processing by ESA, this interpolation is done with cubic splines [Makhoul-Varona et al., 2020]. The second comparison is to be taken between α_j^i and θ and end by the time the angular azimuth beam resolution coincides with the angles of sight.

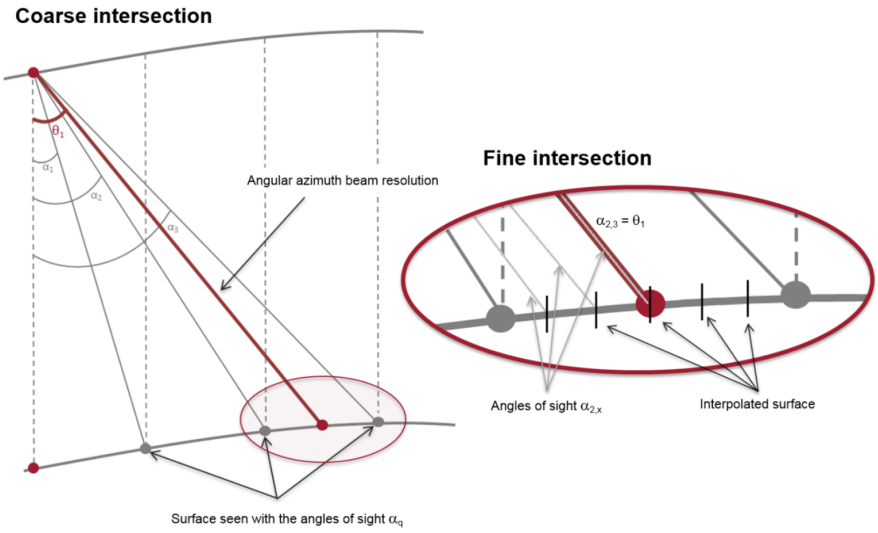

Figure 2.3: *Coarse (left) and Fine (right) Intersection Step of the Surface Locations Algorithm [Credit: isardSAT]*

With the information of associated orbit state from orbit interpolators, the new surface location can, therefore, be also located on the orbit (see Figure 2.4). Furthermore, the window delay of the new surface location is calculated for tracker alignment correction. Then, the process begins again with the obtained new satellite location.

2.2.3 Determining Doppler Beams Direction

To perform the delay Doppler processing later, for each burst, the angles between the satellite velocity vector and the vector between the burst location and all surface locations under the satellite's boresight must be calculated.

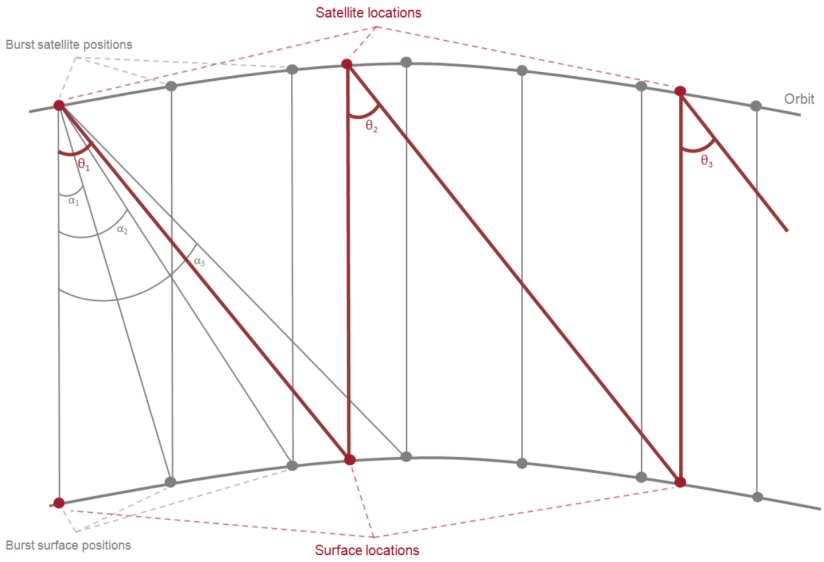

Figure 2.4: *Determination of the Associated Orbit State [Credit: isardSAT].*

The calculation begins with identifying the surface location closest to the nadir direction. Then, N_p surface locations are selected, $N_p/2$ forwards and $N_p/2$ backwards. In the case of Sentinel-3 missions, N_p is 64. These selected surface locations and their indices are stored for later processing. The beam angle θ_c is calculated for each surface locations with the expression [Makhoul-Varona et al., 2020]:

$$\theta_c = \arccos \frac{\mathbf{v_s} \cdot \mathbf{w_{sat \to surf}}}{|\mathbf{v_s}| \cdot |\mathbf{w_{sat \to surf}}|} \tag{2.2}$$

where $\mathbf{v_s}$ is the satellite velocity vector and $\mathbf{w_{sat \to surf}}$ is the vector between the burst location and surface locations.

2.2.4 Delay-Doppler Processing (Beam Steering)

This process is implemented by applying a manipulated phase value to echoes in order to steer the beams towards the computed surface locations. The algorithm generates a set of 64 Doppler beams per burst in the frequency domain, with each Doppler beams steered to a different surface location. The processing is done by applying a Fast Fourier Transform (FFT) in the along-track direction. After processing, the Delay-Doppler map is created; it contains both the delay that the transmitted echo to the tracker and the Doppler frequency shift of that echo.

There are two different methods depending on the accuracy required: exact beam steering and approximate beam steering. The exact method uses all beam angles (64 for Sentinel-3) to guide the beam to each calculated surface position. In contrast, with approximate beam steering, only the center beam angle is used. This means that only the center beam is steered exactly and the other Doppler beams will be steered approximately to their own closest surface positions, so that the other Doppler beams will be equidistant.

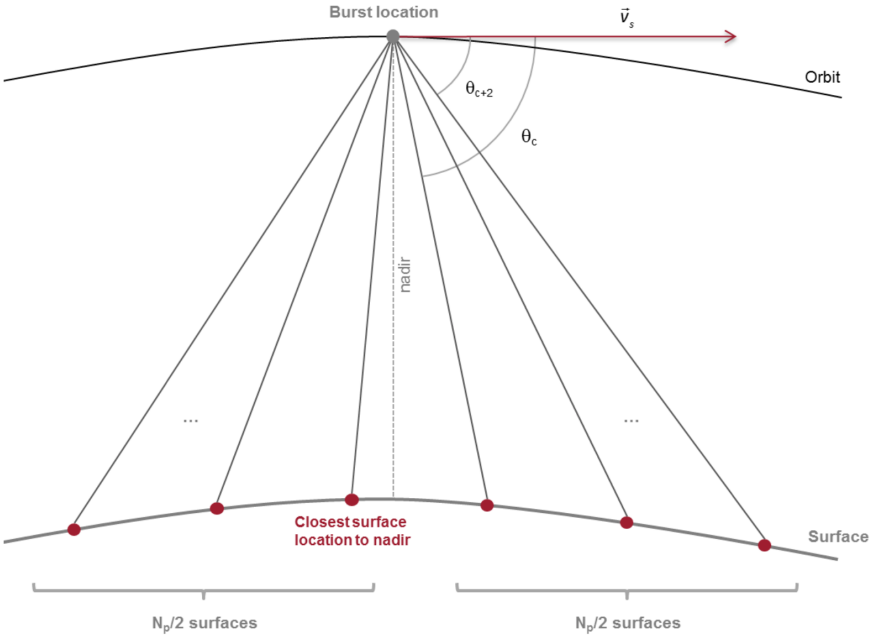

Figure 2.5: *Geometry of the Beam Angles Algorithm [Credit: isardSAT].*

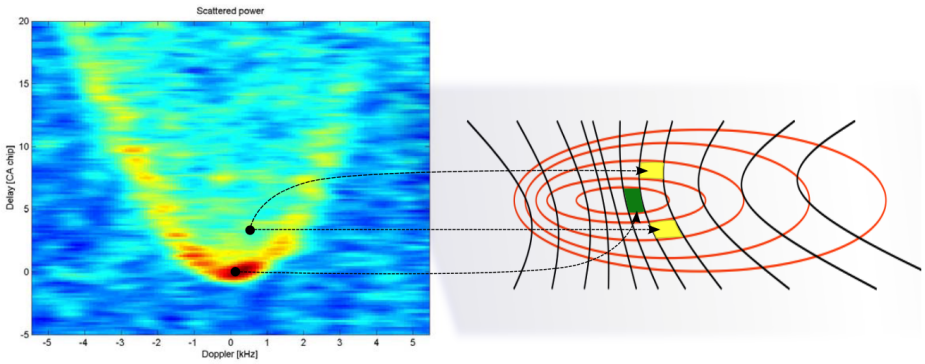

Figure 2.6: *Delay-Doppler Map and Iso-Range and Iso-Doppler Lines on the Surface [Gleason, 2006].*

To apply the FFT, the angles $\theta_{beam}(b,p)$ that are applied to the pulses should be first determined [Makhoul-Varona et al., 2020]:

$$\theta_{beam}(b,p) = \theta_c(b) + \delta\theta_p = \theta_c(b) + \arcsin\frac{\lambda \cdot p}{2|\mathbf{v_s}| \cdot N_p \cdot PRI}\ [rad] \tag{2.3}$$

where

$$\begin{aligned} b &: \text{the index within a burst } b \in [0, N_b - 1] \\ p &: \text{the pulse index } b \in [-\frac{N_p}{2}, \frac{N_p}{2} - 1] \\ \theta_c(b) &: \text{the computed beam angle in section 2.2.3} \\ \delta\theta_p &: \text{the azimuth angular beam resolution} \\ \lambda &: \text{the length of carrier wave} \\ N_p &: \text{the number of pulses in each burst} \\ PRI &: \text{pulse repetition interval} \\ \mathbf{v_s} &: \text{the satellite velocity vector} \end{aligned}$$

And the beamforming is taken as [Makhoul-Varona et al., 2020]:

$$\Phi_b(k,n) = \frac{1}{\sqrt{N_p}} \cdot \sum_{p=0}^{N_p-1} \Phi_w(p,n) \cdot e^{-2j\cdot(\frac{2\pi}{\lambda}\cdot PRI\cdot \mathbf{v_s}\cdot\cos(\theta_c(b))+\frac{\pi\cdot k}{N_p})\cdot p} \tag{2.4}$$

This equation applies to the exact method because each beam is steered according to the corresponding $\theta_c(b)$ and only the central beam is retained for each FFT, while the approximate method utilizes the same equation (Eq (2.4)), but only with single FFT using the central beam angle. Figure 2.7 and Figure 2.8 present the illustration of the exact beam forming and the approximate beam forming.

2.2.5 Beam Stacking

From the DDM, all Doppler beams from different bursts but pointing at the same surface location are collected in one stack. Thus, these stacked Doppler beams illuminate the same surface location at different look angles from different bursts.

2.2.6 Geometry Correction (Range Alignment)

All corrections for geometrical misalignments in range within the same stack are computed and applied. As the beam stacking has been performed, these corrections can be achieved for each stack. Specifically, there are three range corrections: Doppler correction, slant range correction, and tracker alignment correction.

In the case of Sentinel-3, all of theses corrections are applied in the same domain before range compression. By doing so, there is no need to classify the various corrections according to their precise levels, because all corrections are applied as phase shifts.

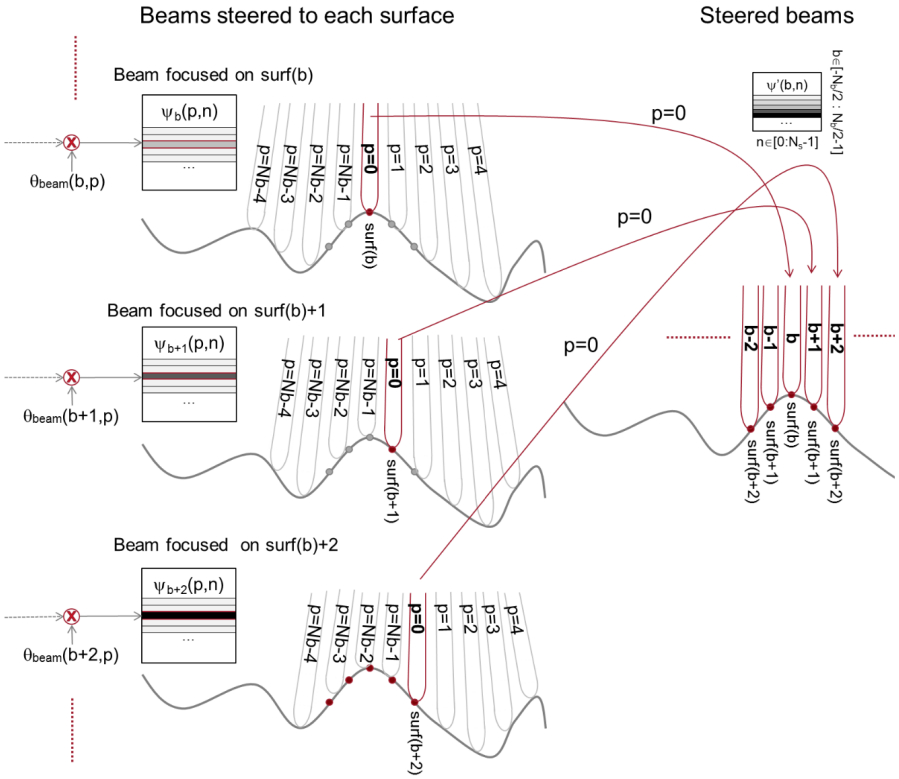

Figure 2.7: *Illustration of the Exact Beam Forming [Makhoul-Varona et al., 2020]*

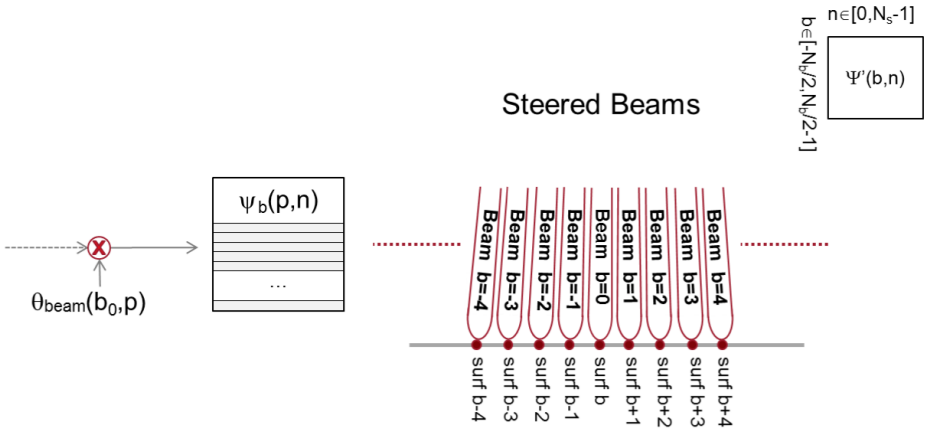

Figure 2.8: *Illustration of the Approximate Beam Forming [Makhoul-Varona et al., 2020]*

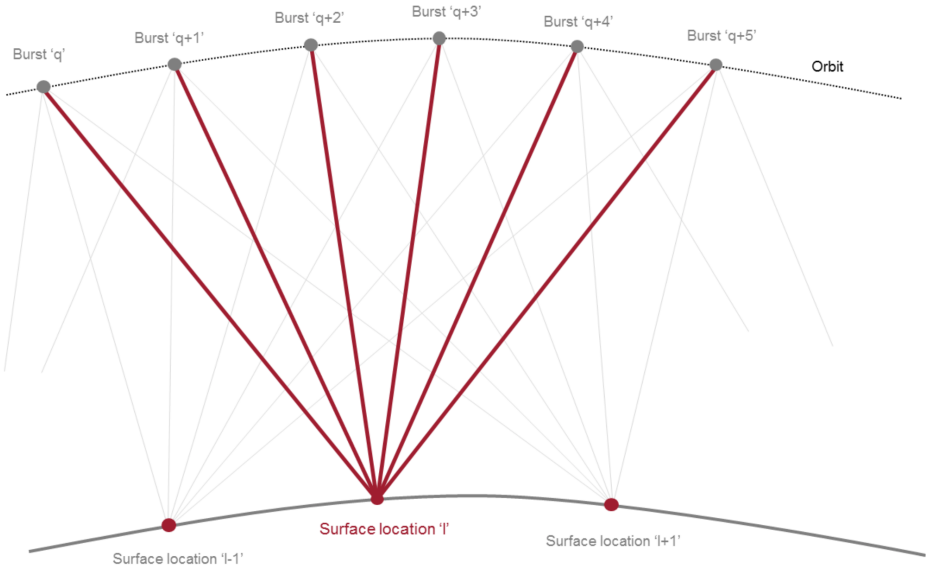

Figure 2.9: *Stacking Process for Surface Location I [Credit: isardSAT]*

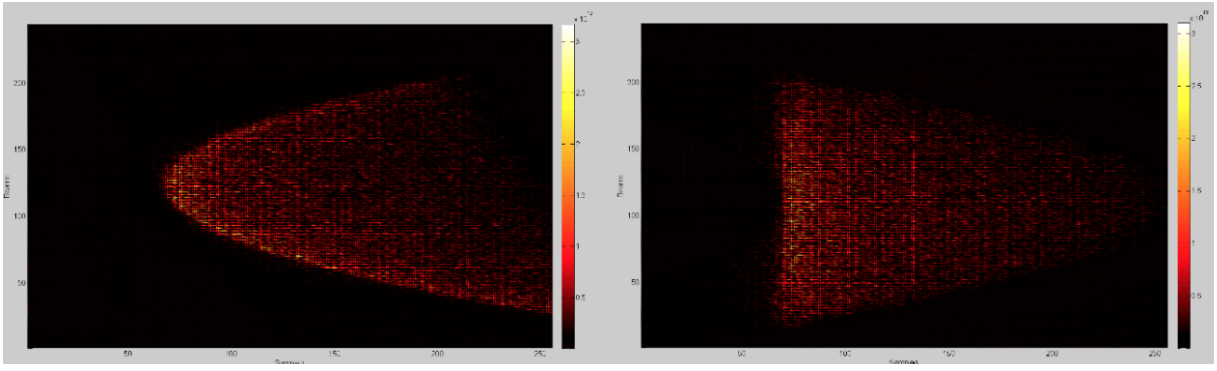

Figure 2.10: *(left) Stack Without Geometry Corrections, (right) Stack With Geometry Corrections Applied [Makhoul-Varona et al., 2020]*

Doppler Correction

The purpose of this correction is to compensate for the Doppler effect due to the movement of the satellite during the transmission and reception of the echo. After beam stacking, the information of each pulses within the stack still exhibits Doppler effects for each processed burst. The Doppler correction, therefore, is applied to lead all pulses in that stack, which means to the same Doppler bin for that processed burst. For each Doppler beam, the Doppler frequency shift is computed for the compensation of the Doppler effect. The frequency shift in meters $\Delta r_D(b')$ is computed as [Makhoul-Varona et al., 2020]:

$$\Delta r_D(b') = \underbrace{\frac{c}{2} \cdot \left[\underbrace{\frac{\tau}{B} \cdot \overbrace{\left(-\frac{2}{\lambda} |\mathbf{v_s}(b')| \cos\theta_c(b') \right)}^{\text{Doppler}}}_{\text{range-delay}} \right]}_{\text{range-shift}} [m], b' \in [0, N_{bs} - 1] \tag{2.5}$$

where

$|\mathbf{v_s}(b')|$: the modulus of the satelites's velocity at the given burst position
c : the speed of light
τ : the pulse of duration
B : the transimitted bandwidth
N_{bs} : the number of beams pointing to that specific surface

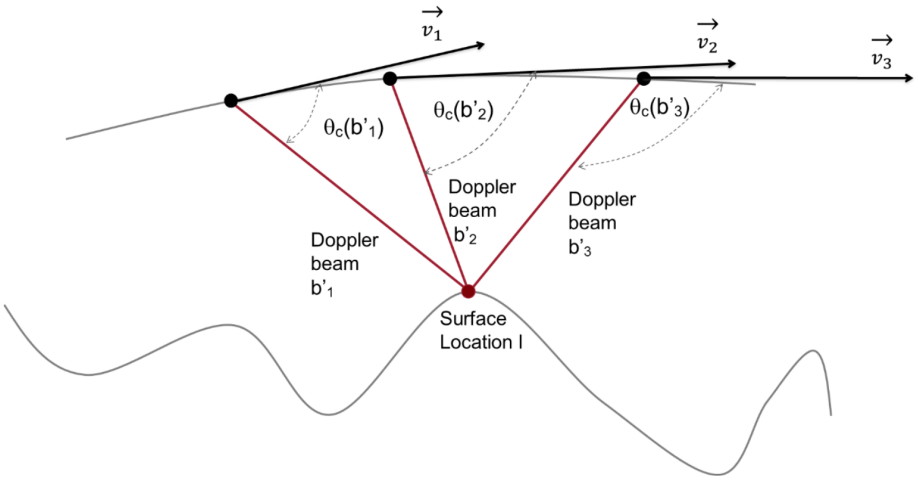

Figure 2.11: *Doppler Shift Effect [Credit: isardSAT]*

Slant Range Correction

Slant range correction refers to range cell migration correction (RCMC). The range migration due to the different radial distances from each surface location to corresponding burst centers is applied. Figure 2.12 indicates the geometry of the slant range correction. For the ranges of the surface location I, the difference $\Delta r(b')$ is computed as:

$$\Delta r(b') = |\mathbf{r}(b'_i)| - |\mathbf{h}(l)| \; [m] \tag{2.6}$$

with $\mathbf{r}(b'_i)|$ being the range to the surface location for each burst position and $|\mathbf{h}(l)|$ being the real surface height.

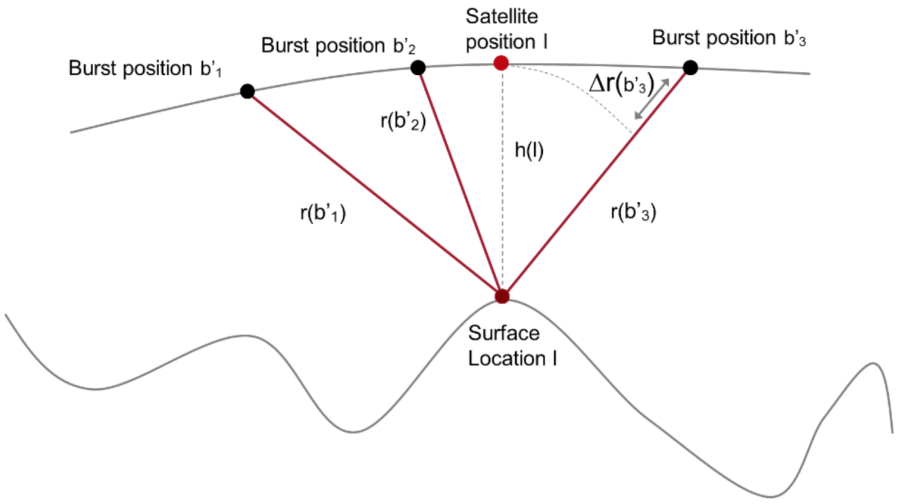

Figure 2.12: *Slant Range Correction [Credit: isardSAT]*

Tracker Alignment Correction

Tracker alignment correction refers to the correction of window delay misalignment. The range misalignment due to the different tracker shifts for Doppler beams within one stack is compensated. In Section 2.2.2, the window delay is already calculated for each surface locations. Thus, the differences between the reference surface location to all burst positions in the stack are computed [Makhoul-Varona et al., 2020]:

$$\Delta S_{wd}(b') = \frac{\tau_{wdref} - \tau_{wd}(b')}{T_0} \; [samples] \tag{2.7}$$

where τ_{wdref} is the reference window delay, $\tau_{wd}(b')$ is the window delay with the b' beam and T_0 is the clock period.

2.2.7 Range Compression

This stage performs a range compression of the Doppler beams in the stack, which is the conversion of Doppler beams from the pulse-width time domain to the frequency domain. This is implemented as a range FFT in the across-track direction. As an option, the zero-padding can be applied before range compression. The details of zero-padding are discussed in the section 2.4.1.

2.2.8 Multi-Looking

This algorithm computes the incoherent summation of all Doppler beams within one stack in the along-track direction. The implementation is to square the signals first and then take the average. The result of this operation is a Level-1B waveform.

In the case of processing by ESA, the calculation of multi-looked waveform required two scaling: iq scaling and AGC scaling. For Level-1BS Product, the scale factor of iq scaling is *iq_scale_factor_l1bs_echo_sar_ku* and the scale factor of AGC scaling is *agc_ku_l1bs_echo_sar_ku*. The multi-looked waveform W_{ML} is performed by a summation of single-looked waveforms $\overline{W}_{k,l}$ within the stack:

$$W_{\mathrm{ML}}(k) = \sum_{n=1}^{N_{eff}} \overline{W}_{k,l}(k,n) \tag{2.8}$$

where N_{eff} is the number of effective single-looked waveforms.

2.3 Level-2 Processing

Level-2 processing consists of applying various retracking algorithms to Level-1 waveforms and computing geophysical corrections for the measurements. In the case of Sentinel-3 missions, four retracking algorithms are applied in the SAR mode based on different topographical conditions to Level-1 waveforms, namely, ocean retracking, offset center of gravity (OCOG) retracking, ice sheet retracking, and sea-ice retracking.

2.3.1 Ocean retracking

An ocean retracker is an analytical retracker for open ocean and coastal zones. The algorithm consists of fitting the theoretical multi-looked waveform model to real Level-1B SAR waveform using the Levenberg-Marquardt method. The theoretical waveform model is inherited from the SAMOSA project. The single-look model is given by [SAMOSA5]:

$$\overline{W_{k,l}} = P_u(\alpha_p^2\sqrt{2\pi})\sqrt{g_l}\,\Gamma_{k,l}(0)\left\{f_0(g_l k) + \frac{\sigma_z}{L_\Gamma}\cdot g_l \cdot \frac{\sigma_z}{L_Z}T_k \cdot f_1(g_l k)\right\} \tag{2.9}$$

The parameters are described by MSSL et al. [2019]:

$$f_0(\xi) = \int_0^{+\infty} e^{-\frac{1}{2}(\xi - v^2)^2}\mathrm{d}v = \frac{\pi}{2\sqrt{2}}\left(\frac{1}{4}\xi^2\right)^{1/4}\left[\mathrm{I}^{\mathrm{sc}}_{-\frac{1}{4}}\left(\frac{1}{4}\xi^2\right) + \mathrm{sign}(\xi)\cdot \mathrm{I}^{\mathrm{sc}}_{\frac{1}{4}}\left(\frac{1}{4}\xi^2\right)\right] \tag{2.10}$$

$$f_1(\xi) = \int_0^{+\infty} e^{-\frac{1}{2}(\xi - v^2)^2}(\xi - v^2)\mathrm{dv} \tag{2.11}$$
$$= \frac{\pi}{2\sqrt{2}}\left(\frac{1}{4}\xi^2\right)^{3/4}\left[\left(\mathrm{I}^{\mathrm{sc}}_{\frac{1}{4}}(\frac{1}{4}\xi^2) - \mathrm{I}^{\mathrm{sc}}_{-\frac{3}{4}}(\frac{1}{4}\xi^2)\right) + \mathrm{sign}(\xi)\cdot\left(\mathrm{I}^{\mathrm{sc}}_{-\frac{1}{4}}(\frac{1}{4}\xi^2) - \mathrm{I}^{\mathrm{sc}}_{\frac{3}{4}}(\frac{1}{4}\xi^2)\right)\right]$$

where

k : the index defined by $k = k' - k_0$ with $k' \in [-\frac{N_p}{2} + 1, \frac{N_p}{2}]$ and $k_0 = t_0 B_r$ (B_r is Bandwidth)

l : Doppler frequency index

σ_z : surface roughness

P_u : the waveform power amplitude

g_l, L_z, L_r, T_z and $\Gamma_{k,l}(0)$ are computed by system parameters. $\mathrm{I}^{\mathrm{sc}}_v$ is the scaled spherical modified Bessel function of the first kind and order v:

$$\mathrm{I}^{\mathrm{sc}}_v(z) = e^{-|z|}\cdot \mathrm{I}_v(z) \tag{2.12}$$

2.3.2 OCOG retracking

First used in both the ENVISAT and CryoSat-2 missions [*Sentinel Online —ESA*, 2021], the OCOG retracker is used in the SAR mode for sea ice margins. The method is empirical and starts from the estimation of OCOG amplitude. The OCOG retracker bin can be calculated by OCOG amplitude. The range correction is then computed as the difference between the OCOG retracker bin and the nominal tracking point.

The OCOG amplitude P_{OCOG} is computed as [MSSL et al., 2019]:

$$P_{OCOG} = \sqrt{\frac{\sum_{i=0}^{N_s-1} P^4[i]}{\sum_{i=0}^{N_s-1} P^2[i]}} \tag{2.13}$$

The OCOG retracker bin is:

$$i_{OCOG} = (i_0 - 1) + \frac{P_{OCOG} - P[i_0 - 1]}{P[i_0] - P[i_0 - 1]} \tag{2.14}$$

where i_0 refers to the index of the first bin containing more power than P_{OCOG}. The OCOG retracker bin is:

$$\delta R_{OCOG} = (i_{OCOG} - i_{TP}) \times d_{bin} \tag{2.15}$$

where d_{bin} is the size of a range window bin in meters and i_{TP} is the index of the nominal tracking point. The OCOG corrected range is computed as:

$$R_{OCOG} = R_{tr} + \delta R_{OCOG} + d_{CoG} + \frac{ct_{FFT}}{2} First\ bin \tag{2.16}$$

First bin refers to the first gate appearing in the window, and d_{CoG} is the CoG correction.

2.3.3 Ice Sheet Retracking

The ice-sheet retracker is inherited from the CryoSat-2 mission. The algorithm is taken by fitting the retrieved Level-1B SAR waveform analytically to an echo model, which has a modified Gaussian form and consists of five sections. The amplitude and the retracker bin can be derived from the fitted waveform.

The echo modell is given by:

$$P(t) = ae^{-f(t)} \tag{2.17}$$

where f_i is a five-part function that describes the shape of the waveform. The five functions are [MSSL et al., 2019]:

$$f_1(t) = g(t - t_0) + (m - g(t_0 - n\sigma)) \text{ where } t < t_0 + n\sigma \tag{2.18}$$

$$f_2(t) = b_0 + b_1(t - t_0 - t_1) + b_2(t - t_0 - t_1)^2 + b_3(t - t_0 - t_1)^3 \text{ where } t + n\sigma < t < t_0 + t_2 \tag{2.19}$$

$$f_3(t) = \frac{1}{\sigma(t - t_0 - t_1)} \text{ where } t_0 + t_2 < t < t_0 - t_1 \tag{2.20}$$

$$f_4(t) = \frac{1}{\sigma}(t - t_0 - t_1) + a_2(t - t_0 - t_1)^2 + a_3(t - t_0 - t_1)^3 \text{ where } t_0 - t_1 < t < t_0 - t_3 \tag{2.21}$$

$$f_5(t) = \left(- \log \left[\frac{ce^{-\alpha(t-t_0)}}{a\sqrt{t - t_0}} \right] \right)^{1/2} \text{ where } t > t_0 + t_3 \tag{2.22}$$

The unknown parameters of the modell can be derived by applying the Levenberg-Marquart method. With these parameters, the amplitude of the ice sheet is calculated as:

$$P_{IceSheet} = a \times \max(P) \tag{2.23}$$

The ice sheet retracker bin is given as:

$$\delta R_{IceSheet} = d_{bin} \times (i_{\text{IceSheet}} - i_{\text{TP}}) \tag{2.24}$$

Finally, the ice sheet's corrected range is computed as:

$$R_{IceSheet} = R_{tr} + \delta R_{IceSheet} + C + d_{CoG} \tag{2.25}$$

where C is the geophysical and meteorological corrections.

2.3.4 Ice Retracking

This retracking method is a heritage of the ice-2 retracker (also called ice erf re-tracker) implemented in both the ENVISAT and CryoSat-2 missions. It is a physical-based retracker. The expression of the return power is given [Brown,1977]:

$$Vm(t) = \frac{P_u}{2} \cdot \left[1 + \mathrm{erf}\left(\frac{t-\tau}{\sigma_L}\right)\right] \cdot \exp[s_T \cdot (t-\tau)] + P_n \tag{2.26}$$

with

$$\mathrm{erf}(x) = \frac{2}{\sqrt{\pi} \cdot \int_0^x e^{-t^2} \mathrm{dt}} \tag{2.27}$$

where

τ : the epoch
σ_L : the width of the leading edge
P_u : the amplitude
s_T : the slope of the logarithm of the trailing edge
P_n : the thermal noise level

2.3.5 Sea Ice Retracking

The sea ice retracker is designed for sea-ice waveforms and was first used in the CryoSat-2 Mission. It is a simplified version of the ice sheet retracker using only three-part fitting functions. The waveform is modeled into three parts, which are the leading edge, the trailing edge, and a linking part between the leading and the trailing edges.

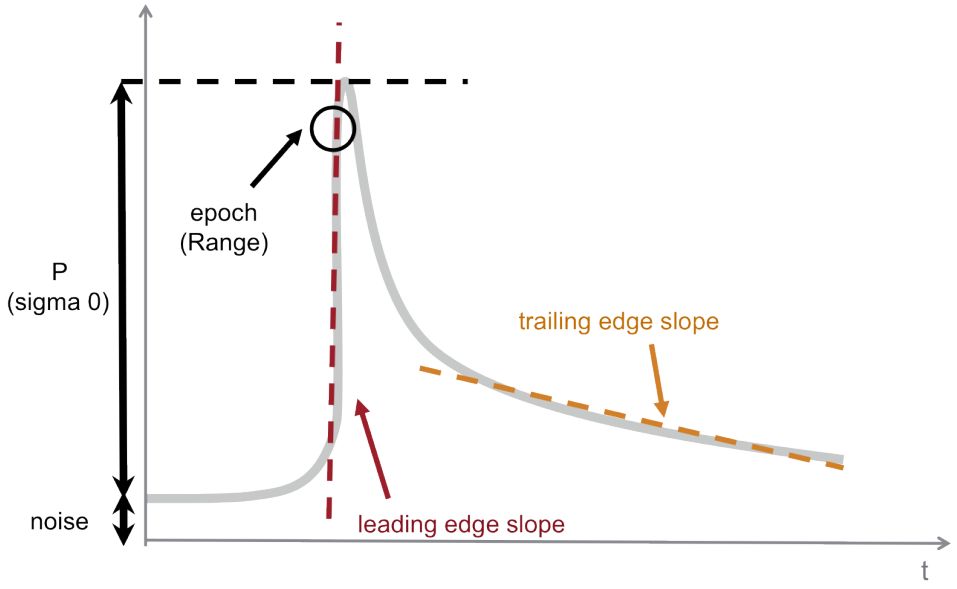

Figure 2.13: *Schematic Description of Leading Edge and Trailing Edge [Credit: isardSAT]*

The echo modell is [MSSL et al., 2019]:

$$P(t) = f(t, \alpha) \tag{2.28}$$

where $f(t, \alpha)$ is a three-part function. The leading edge is described by $f(t, \alpha)$:

$$f_1(t, \alpha) = a_0 e^{-\left[\frac{t-t_0}{\sigma}\right]^2} \tag{2.29}$$

The linking part is given by:

$$f_2(t, \alpha) = a_0 e^{-\left[-\frac{3k\sigma-2c}{2\sigma t_b^2 c}(t-t_0)^3 - \frac{-5k\sigma+4c}{2\sigma t_b c}(t-t_0)^2 + \frac{1}{\sigma}(t-t_0)\right]^2} \tag{2.30}$$

where

$$t_b = k\sigma^2 \tag{2.31}$$

$$c = \sqrt{kt_b} \tag{2.32}$$

And the trailing edge is fitted by:

$$f_3(t, \alpha) = a_0 e^{-k(t-t_0)} \tag{2.33}$$

In summary, the echo modell is:

$$P(t) = \left\{ \begin{array}{lll} P_1(t) & for & t < t_0 \\ P_2(t) & for & t_0 < t < t_b \\ P_3(t) & for & t_b < t \end{array} \right\} \tag{2.34}$$

The range correction for a sea ice retracker is:

$$\delta R_{fit} = (i_{fit} - i_{TP}) \times d_{bin} \tag{2.35}$$

The corrected range is computed by:

$$R_{fit} = R_{tr} + \delta R_{fit} + C + d_{CoG} \tag{2.36}$$

2.4 Platforms for processing SAR altimetry

2.4.1 SARvatore

The grid processing on demand (G-POD) service, SARvatore (SAR versatile altimetric toolkit for ocean research and exploitation) for Sentinel-3, is a web platform that provides online services to process SRAL Level-1A data in Sentinel-3 SAR mode to Level-1B and Level-2 products. The service is based on the Sentinel-3 SARvatore processor prototype, a heritage of the CryoSat-2 SARvatore processor prototype [*GPOD User manual*, 2021].

The input values for the SARvatore service are Level-1A data, which are stored in the G-POD server and can be selected by the geographical area of interest, by specifying latitude, longitude, time, or relative orbit number (RON). The output data are available as Level-2 products, which contain waveforms and range integrated powers (RIPs), and as Level-1B products,

Figure 2.14: *Interface of Selecting Input Data*

Option Name	Option Value	Official S3	Inland Water
Data Posting Rate	- 20 Hz - 80 Hz	- 20 Hz	- 20 Hz
Range Walk Correction	- No -Yes	- No	- No
Hamming Weighting Window	- Only in coastal zone - Yes, apply it - No, do not apply it	- No	-Yes
Exact Beam-Forming	- Approximated - Exact	- Approx.	- Approx.
FFT Zero-Padding	- Yes - No	- No	-Yes
Radar Receiving Window Size	- 128 range bins - 128×2 range bins - 128×3 range bins - 128×4 range bins	- 128 range bins	- 128×2 range bins
Antenna Pattern Compensation	- No - Yes	- No	- No
Dump SAR Stack Data in Output	- No - Yes, with only power - Yes, with power and phase		

Table 2.1: *Level-1 Processor Options*

Option Name	Option Value
Restrict the Retracking on Specific Surfaces	- Process all - Process only open sea points - Process only water points
PTR Width Alphap Parameter	- LUT - Constant
SAMOSA Model Generation	- Use SAMOSA2 - Use SAMOSA3 - Use SAMOSA+ - Use SAMOSA++
Dump Rrange Integrated Power (RIP) in Output	-No -Yes
Dump SAR Echo Waveforms in Output	-No -Yes
Single-Look or Multi-Look Model	- Multi-look - Single-look
Choose the Default Tide Model	- FES2014b - TPXO8 - TPXO9
Choose the Default Mean Sea Surface Model	- DTU18 - DTU15 - CLS-CNES15

Table 2.2: *L2 Processor Options*

which include SAR stack data, generated in standard NetCDF and that can be read by any NetCDF tools.

Table 2.1 and Table 2.2 present the options provided by the SARvatore service, which offer several sets of configurations such as Official S3, Inland Water, et cetera. The Level-1 processor settings for both configurations are indicated in Table 2.1. The same parts of these two configurations for the Level-2 processor are underlined, with the difference being that Official S3 uses SAMOSA2 while Inland Water uses SAMOSA+.

Level-1B Processor

Data Posting Rate

The SARvatore service provides with two options for data posting rate: 20 Hz and 80 Hz. According to Dinardo et al. [2018], 80 Hz is chosen because it corresponds to the burst repetition interval (BRI) of the CryoSat-2 and Sentinel-3. Fixing the grid center location at the burst center avoids interpolating the ground locations of satellite orbits at 300 m intervals. The grid step is changed from 300 m to 80 m [Dinardo, 2020].

Range Walk Correction

Range walk is the changing range migration during the burst acquisition, and its compensation can be added to delay-Doppler processing aiming at increasing the accuracy of the Level-1B waveforms [Scagliola et al., 2021]. Exact Doppler beam steering should also be applied when applying range walk correction. The range walk correction is applied necessarily only over the ocean where waves are moving. In case of inland water altimetry, this correction should not be necessary.

Hamming Window

The Hamming window is a low-pass filter in time domain defined by Richard W. Hamming. The window function is applied prior to delay-Doppler processing, which is an FFT in the along-track direction. The purpose of applying the Hamming window is to mitigate the effect of side-lobes ambiguity. However, at the same time, the Hamming window leads to a widening of the main beam, which results in a decrease of the resolution from 300 m to 400 m in the along-track direction [Dinardo et al., 2018]. Additionally, the peak power is also reduced. Figure 2.15 indicates the comparison of azimuth impulse response with and without the Hamming window. The black line represents the response without the Hamming window, while the red line represents the response with the Hamming window. The Hamming window is recommended to be used in the situation of specular surface where the nadir echo contains strong energy [Bouzinac et al., 2019]. Figure 2.16 illustrates an example for sea ice, with the two graphs above representing an azimuth FFT of a single burst and a beam stack map without the Hamming window and the two graphs below representing the situation with the Hamming window.

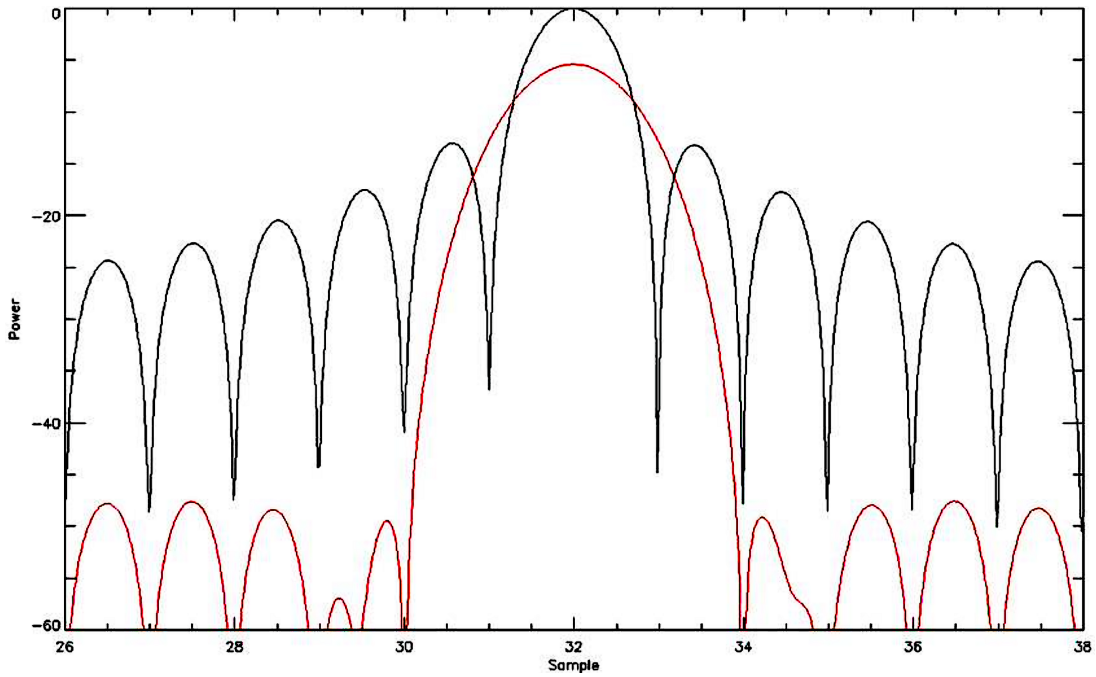

Figure 2.15: *Comparison of Azimuth Impulse Response With and Without Hamming Window (black: without Hamming Window red: with Hamming Window)[Bouzinac et al., 2019]*

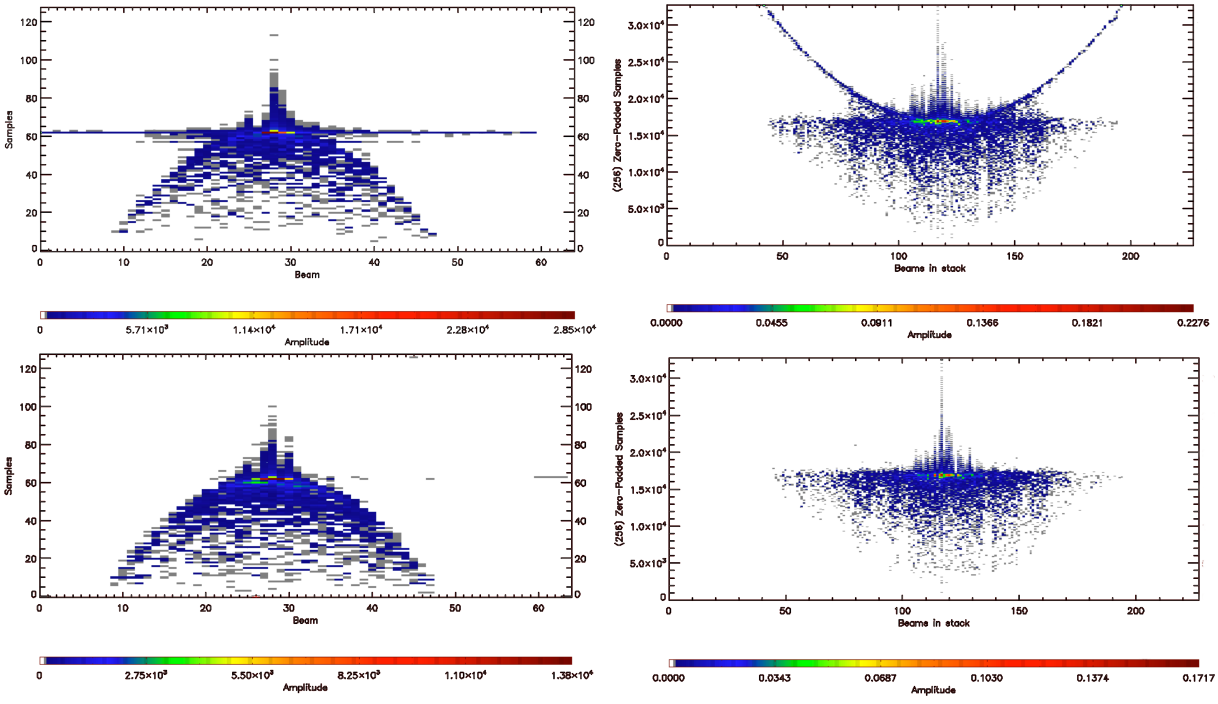

Figure 2.16: *Azimuth FFT of a Single Burst and Beam Stack Map With and Without Hamming Window (left: Before RCMC right: After RCMC) [Bouzinac et al., 2019]*

Zero Padding

Zero padding refers to adding zeros to the end of a time-domain signal so that the total number of samples is equal to the next higher power of two. In case of Sentinel-3, the original number of the sample is 128, and zero padding is the addition of 64 zeros before and after the data, thus making the total number of samples to 256. Zero padding is applied prior to range compression in order to oversample the waveform and, hence, avoid aliasing effects in the case of peaky waveform.

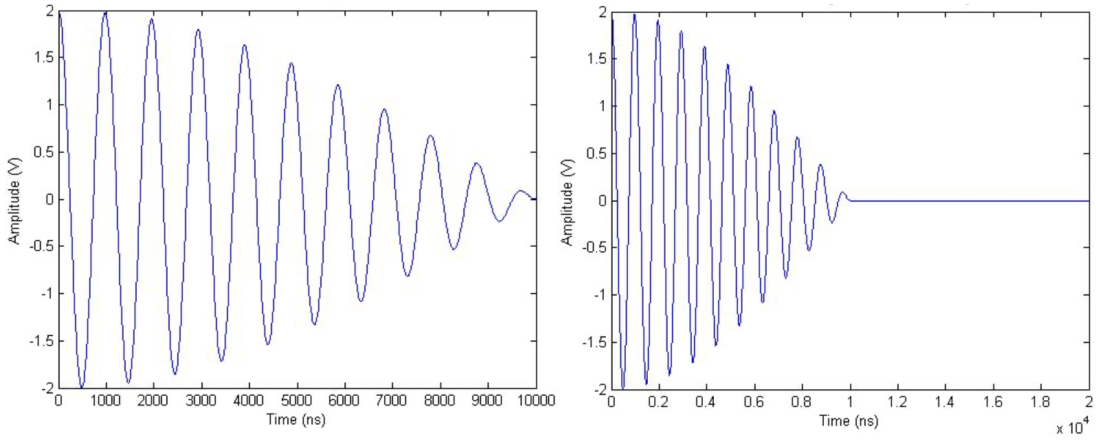

Figure 2.17: *Zero Padding in Time Domain by Adding Zeros [*bitweenie*, 2021]*

Extended Radar Receiving Window

In this situation, the double extension of the receiving window consists of using a larger receiving window of 512 samples (with zero-padding) to store the stack data in range dimension after the slant range compensation.

Level-2 Retracker

The SARvatore provides four Retrackers: SAMOSA3, SAMOSA2, SAMOSA+, and SAMOSA++. These four trackers are based on the SAMOSA model, a physically-based model that provides a complete description of SAR altimeter returned waveform, allowing the returned waveform to be represented as maps of reflected power in delay-Doppler space [Dinardo, 2020].

SAMOSA3 and SAMOSA2

The SAMOSA model was first introduced by Ray et al. [2015]; it assumes that the sum of the power of all the scatters across the sea surface follow the Brown model [Brown, 1977]. Furthermore, four approximations are made that are described in Ray et al. [2015] to arrive at a closed-form expression of the waveform. The waveform is expressed finally as:

$$P_{k,l} = KB_{k,l}\sqrt{g_l}\left[(1 + T_{k,l}k_{off})f_0(g_l\kappa) + T_{k,l}g_l\sigma_s^2 f_1(g_l\kappa) + \lambda_s\frac{g_l^3\sigma_s^3}{6}(3f_1(g_l\kappa) + f_3(g_l\kappa))\right] \quad (2.37)$$

with

$$K = \frac{\lambda_0^2 N_b^2 L_x L_y}{4\pi h^4} \sqrt{2\pi} A_g^2 \sigma_g^2, \quad \sigma_s = \frac{\sigma_z}{L_z} \tag{2.38}$$

$$k_{off} = \frac{\langle z \rangle - z_{EM}}{L_z} \quad \kappa = k + k_{off} \tag{2.39}$$

$$g_l = [\sigma_g^2 + (2\sigma_g l L_x^2 / L_y^2)^2 + \sigma_s^2]^{-1/2} \tag{2.40}$$

$$f_n(\xi) = \int_0^\infty dv (v^2 - \xi)^n e^{-(v^2-\xi)^2/2} \tag{2.41}$$

$$B_{k,l} = \int_{-\infty}^{\infty} dz \frac{e^{-z^2/2\sigma^2}}{\sqrt{2\pi}\sigma} \Gamma_{k,l}(z) \tag{2.42}$$

$$L_x = \frac{ch f_p}{2 v_t f_c N_b}, \; L_y = \sqrt{\frac{ch}{\alpha s \tau_u}}, \; L_z = \frac{c}{2 s \tau_u} \tag{2.43}$$

$$T_{k,l} = \frac{L_z}{B_{k,l}\sigma^2} \int_{-\infty}^{\infty} dz \frac{e^{-z^2/2\sigma^2}}{\sqrt{2\pi}\sigma} z \Gamma_{k,l}(z) \tag{2.44}$$

Where

k, l : Cell(k,l) reffers to range k of beam l
v_t : the tangential velocity of the satellite in the Earth-centered frame
s : the chirp slope
τ_u : the usable pulse length
f_c, f_p : the center frequency and pulse repetition frequency
λ_0 : the width of the leading edge
N_b : the number of pulses in a burst
h : the presumed distance between the instrument and the sea surfaces as estimated by the altimeter's onboard tracker
A_g, σ_g : parameters of Gaussian apparoximation of Υ^2
$\langle z \rangle, \sigma_z$: the mean sea height and its standard derivation
z_{EM} : electromagnetic bias

The system is defined in a right-hand coordinate system with the origin at the specular point on the sea surface. The z-axis is normal to the surface and the x-axis is in the plane formed by the satellite velocity and z-axis. The point(x, y, z) is refer to the initial location of the scatterer. The expression of f_0 and f_1 are introduced in Equation 2.10 and Equation 2.11.

The SAMOSA3 retracker uses only the zero-order term of the model and the SAMOSA2 retracker uses both the zero and the first-order terms.

SAMOSA+

SAMOSA+ is the abbreviation of the SAMOSA-based marine SAR retracker; it was first introduced in Dinardo et al. [2018]. While it was based on the original SAMOSA model, two additions were implemented to the model to overcome the performance deficiencies of the SAMOSA2 and SAMOSA3 retracker in coastal areas, inland waters, and sea ice by breaking the assumption of a non-coherent backscattering surface on which the physical model is based.

The first innovation is the selection of the first guess of the epoch for range determination. It is not governed by the position of the waveform peak, but by the peak position of the moving point-wise product in a subset of 20 consecutive waveforms. The off-nadir effect is mitigated by applying the correlation power. Figure 2.18 illustrates the utility of the new method in avoiding land contamination. The upper red line reveals the first guess epoch from the waveform's maximum while the lower blue line indicates the first guess epoch from the point-wise product.

In the SAMOSA2 and SAMOSA3 retrackers, the mean squared slope (MSS) is set to zero, which means that the reflecting surface is considered as an infinite diffuse surface on the footprint. Both the SAMOSA2 and SAMOSA3 trackers are designed for ocean surfaces where the backscatter profile is assumed to be uniform at near-nadir incidence. Thus, the second improvement of the SAMOSA+ retracker lies in the treatment of specular waveforms: The mean squared slope is not treated as a constant in the fitting algorithm, but as one of the parameters that needs to be estimated. With this algorithm, the SAMOSA+ retracker has the ability to simultaneously fit the sharp waveforms generated by bright targets and the broad diffuse waveforms generated over the ocean [Dinardo, 2020].

SAMOSA++

The SAMOSA++ retracker [Dinardo, 2020] refers to the SAMOSA-based pan-thematic SAR retracker. Based on the SAMOSA+ retracker, the SAMOSA++ retracker adds new information extracted from the Range Integrated Power (RIP) to the SAMOSA model. The RIP is derived from the summation in the range direction of the beam stack map and reveals the backscattering profile in the along-track direction. By fitting the RIP waveform using the Gaussian model, the term $\Gamma_{k,l}(0)$ of function Γ (Equation 25 in Ray et al. [2015]), the product of the gain and the radar cross section, can be rewritten as the product of the RIP in along RIP_{az} and RIP in across track RIP_{act} directions [Dinardo, 2020]:

$$\Gamma_{k,l}(0) = RIP_{az}(x_l) \cdot RIP_{act}(y_k) \tag{2.45}$$

Where x_l is the along track coordinate and y_k is the across track coordinate. Figure 2.19 illustrates the contribution of $\Gamma_{k,l}(0)$ derived from the RIP information to different shapes of waveforms. Regardless of whether $\Gamma_{k,l}(0)$ behaves as a circular Gaussian or possesses sharp peaks, the SAMOSA++ retracker is always be able to cope with returned waveform shapes.

It should be added that the Gaussian model sometimes does not fit the RIP waveform due to the relatively sharp shape of the RIP in the coastal regions. Instead, a functional model consisting of a sum of four Gaussians is used to fit the RIP [Dinardo, 2020].

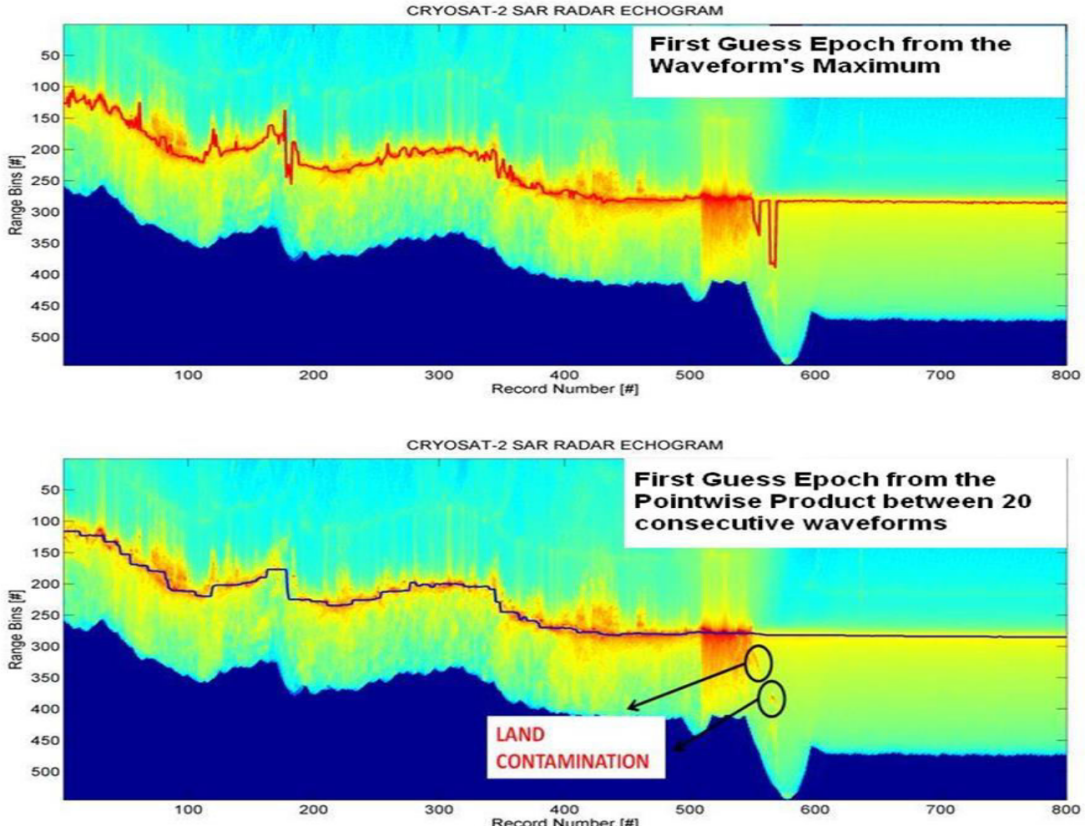

Figure 2.18: *CryoSat-2 SAR Echogram in the German Bight with a Land-Sea Transition [Dinardo, 2020]*

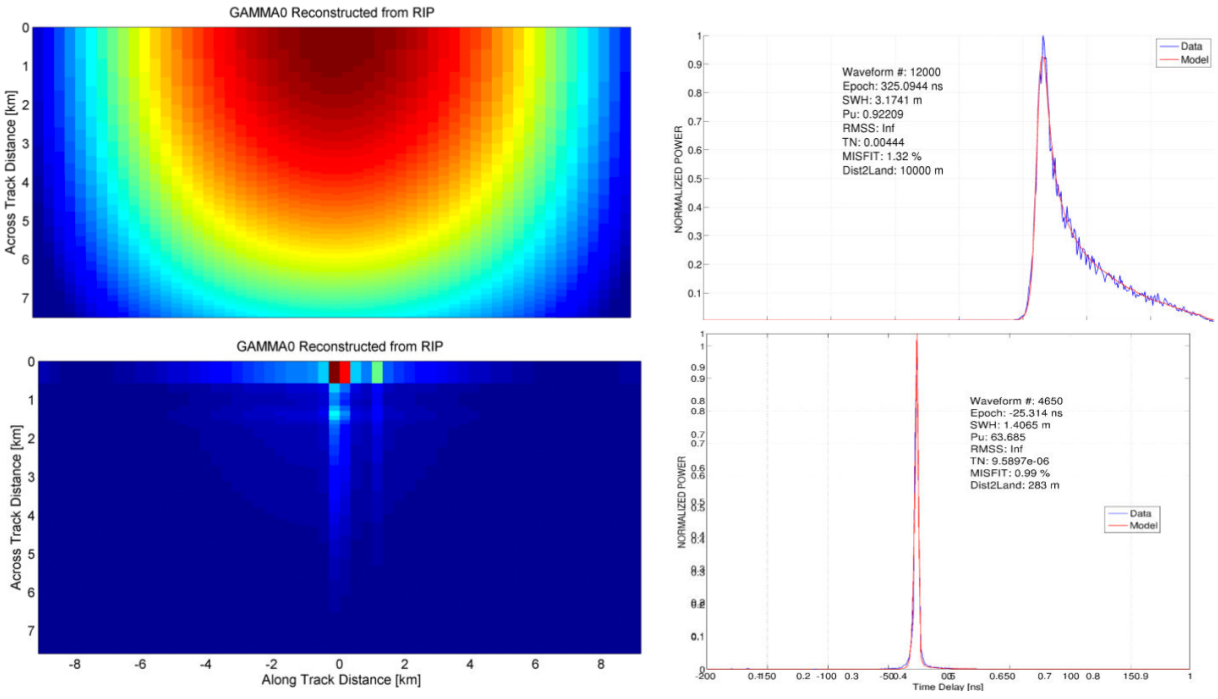

Figure 2.19: *Different $\Gamma_{k,l}(0)$ Contributes to Different Shapes of Waveforms [Dinardo, 2020]*

2.4.2 DeDop

DeDop is an open source toolbox funded by the ESA. The DeDop tool processes Level-1A product to a Level-1BS product and a Level-1B Product. Compared to the SARvatore service product or standard official product, DeDop provides with additional setting options for Level-1B processing. The DeDop tool comprises both a command-line interface, the DeDop Shell, and a graphical user interface, the DeDop Studio. The main goal of the tool is to make it easy to configure and run, and to provide some analysis functions to check and compare the Level-1B results [*DeDop User manual*, 2021]. Because DeDop does not provide Level-2 product, this thesis will not use DeDop to process the data.

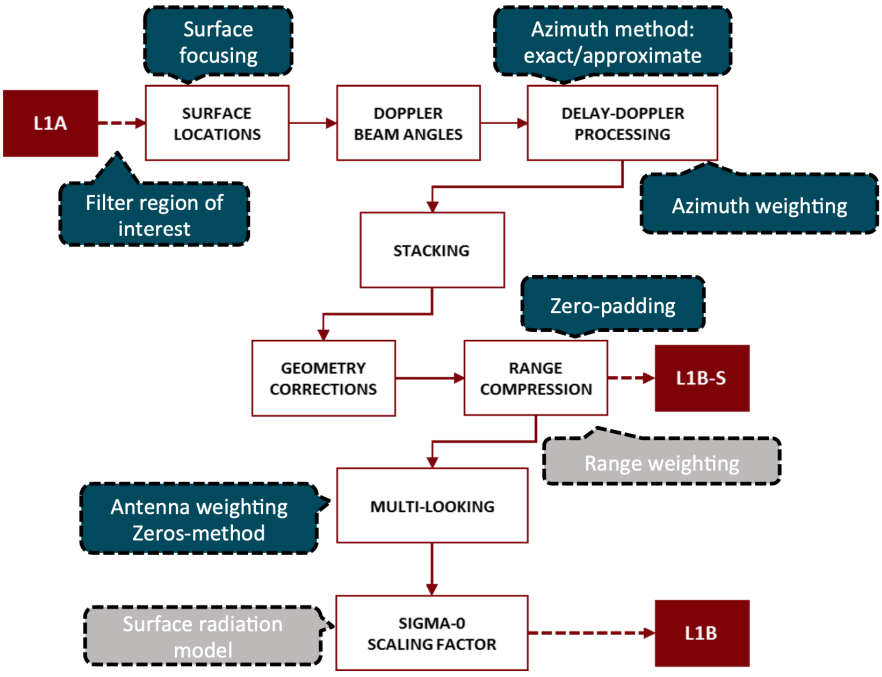

Figure 2.20: *Blockdiagram of DeDop*

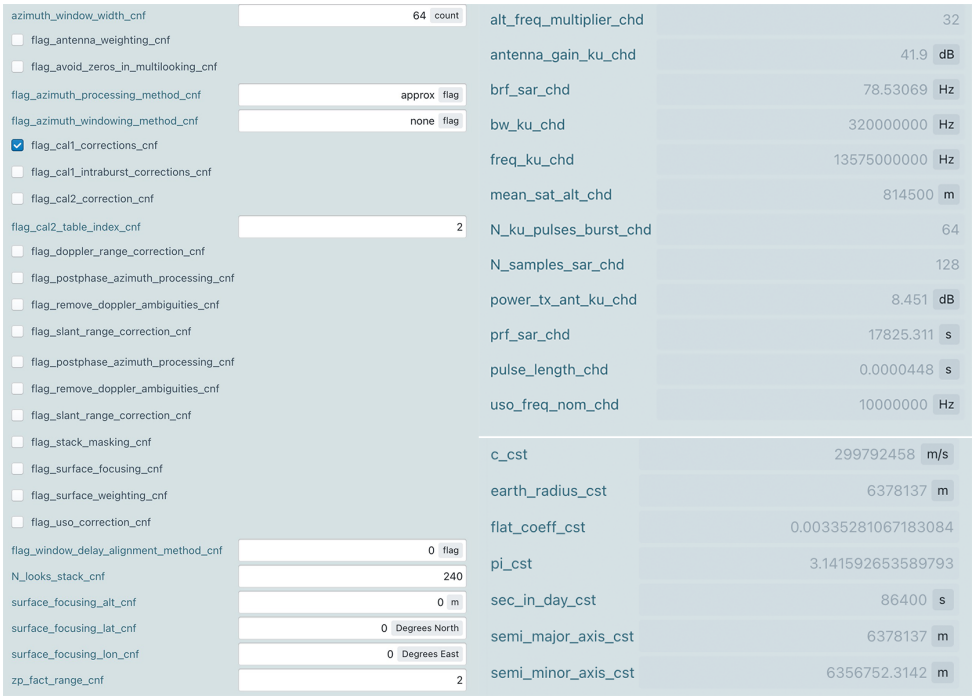

Figure 2.21: *A Snapshot from DeDop with Different Options that can be Configured*

Chapter 3

Fully Focused SAR

3.1 Introduction

As mentioned in Section 1.3.2, the duration of one burst cycle in SAR mode is 12.5 ms, or 80 Hz. Since the delay-Doppler processing is specific to each burst (64 echoes within each burst), its data rate is restricted to a maximum of 80 Hz. In recent years, the so-called fully focused SAR (FF-SAR) has been applied to process CryoSat-2 and Sentinel-3 data. Compared to delay-Doppler processing, FF-SAR is able to process different bursts with proper delay and phase compensation, thus increasing the along-track resolution up to its theoretical limit, which is half the antenna length. Furthermore, the effective number of looks (ENL) also rises with the number of multilooks [Egido and Smith, 2017].

The brief introduction of processing steps following Egido and Smith [2017] is given. The processing begins with the definition of illumination time, that is, to determine how much data needs to be synthesized. The main purpose of FF-SAR processing is to align the delay and phase of these radar echoes within the illumination time in order to coherently combine them.

Based on the deramp-on-receive technique and considering that the satellite is moving during the transmission and reception of the radar signals, the intermediate frequency (IF) or beat signal is described with $\tau' = \tau - d$ as [Egido and Smith, 2017]:

$$s_{IF}(t,\eta) = s_t(t-d) \cdot s_r(t,\eta)^* \tag{3.1}$$

$$= \exp\left(2\pi j\left(f_c\tau' - \alpha\tau' t + \frac{\alpha}{2}\tau'^2\right)\right) \tag{3.2}$$

where

t : fast time
τ : slow time
f_c : carrier frequency
α : chirp rate
v_r : the relative velocity of the platform with respect to the scatterer at the center of the radar pulse
d : delay of the transmitted signal

Fast time refers to the different time slots composing a pulse repetition interval (PRI) and slow time updates every PRI [Ilioudis, 2021]. Same as the delay-Doppler processing, RCMC is applied after an along-track FFT. The geometrical corrections are applied during the target illumination time, the delay for any point can be described as [Egido and Smith, 2017]:

$$\tau'(\eta) = \gamma_i + 2\frac{\delta R_i(\eta)}{c} \tag{3.3}$$

With γ_i is defined as the minimum two way travel time to the target referenced to the tracker range and $\delta R_i(\eta)$ is a function of slow time for the range migration, which can be calculated according to the satellite orbit positions [Egido and Smith, 2017]. By adding the range displacement causing from the Doppler frequency shift, the total range cell migration is

$$\delta R_i(\eta) - cf_D(\eta)/\alpha \tag{3.4}$$

With $f_D(\eta)$ is the Doppler frequency and α is the chirp rate. Applying all the corrections to Eq. (3.1), the corrected signal at ith scatterer on the surface is [Egido and Smith, 2017]:

$$\begin{aligned} s_{i,RCMC}(t,\eta) &= s_{i,IF}(t,\eta)\exp\left(2\pi j\left(\frac{2\alpha\delta R(\eta)}{c} - f_D(\eta)\right)t\right) \\ &= \exp\left(2\pi j\left(f_c\tau_i'(\eta) + \alpha\gamma_i t + \frac{\alpha}{2}\tau_i'(\eta)^2\right)\right) \end{aligned}$$

The relative range phase (RRP) is defined as the first term on the complex exponential, which amount to the phase rotation due to range migration.The second term is the continuous wave (CW) phase. The third term on the complex exponential is the residual video phase (RVP).

After correcting the range cell migration, the range compression is implemented as a range FFT in the cross-track direction, so that the proper phase correction can be applied in frequency domain. The phase errors need to be analyzed in both RRP and RVP, where RVP effects are removed by checking the position of the target in the complex radar map and RRP effects are removed by applying the RRP couterrotation to the signal according to delay history. Finally, the single-look waveform is obtained by summing over the range- and phase-aligned echoes within the coherent processing time.

3.2 SMAP

SMAP is a standalone altimeter data processor written in Python 3 (3.7.3). It can accomplish fully focused SAR processing (time-domain back-projection algorithm) for Sentinel-3 Level-1A products. The program provides with different configurations to process Level-1A data.

The input data are standard Sentinel-3 Level-1A products, a configuration file, a LTM CAL2 ascii file, which is provided by program and available for both Sentinel-3A and Sentinel-3B, and optionally a shapefile to restrict the processing to specified areas. The bounding box in configuration file can also restrict the processing area. In addition to bounding box, the options consisting in configuration file are shown in Table 3.1. The output data includes the L1B product and L2 product in NetCDF format.

The program provides a sample configuration for hydrological study which is also shown in Table 3.1. The study in this thesis focuses on zero padding and hamming window, so four configurations are set up based on the default Hydro configuration, see Table 4.2.

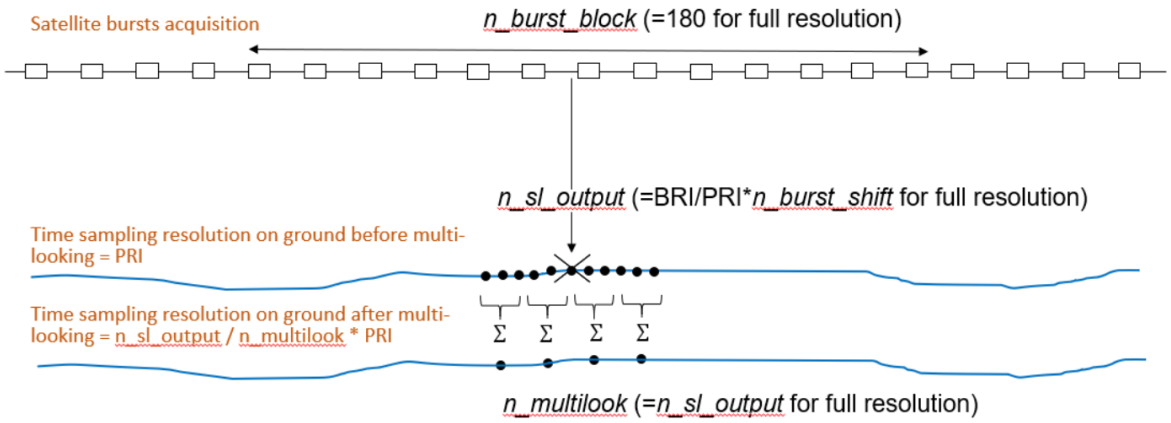

Figure 3.1: *Generation of Multilooks with FFSAR from One Data Block [Credit: CLS Team]*

Illumination time

FF-SAR processing of SMAP runs on a data block consisting of a number of bursts and shifts the bursts along the input file, processing the data in sequence (see Figure 3.1). The illumination time defines the time of the synthetic aperture, i.e., the size of the data block. 2.3 s refers to the 180 bursts for one data block.

The along-track resolution between single looks is given by [CLS Team]:

$$\delta_{AlongTrack}(SingleLook) = \frac{0.886 \cdot wavelength \cdot altitude_{sat}}{2 \cdot v_{proj} \cdot illumination\ time} \tag{3.5}$$

where v_{proj} is the satellite velocity projected on ground.

Posting Rate

Posting rate defines the along-track resolution between multi-looks, which is also the final along-track resolution for the output data. The along-track resolution between multi looks can be calculated by [CLS Team] as:

$$\delta_{AlongTrack} = \frac{v_{proj}}{posting\ rate} \tag{3.6}$$

where v_{proj} is round 8441 m/s. The along track resolution for output data with posting rate 640 Hz is about 13 m.

Option name	Option value	Hydro
Processing		
Name of one l1b processing	ffsar_bp	ffsar_bp
Name of l2 processing (retracker)	- OCOG_SAR - PTR - MultiPTR	- OCOG_SAR - PTR - MultiPTR
L1b options		
Illumination time	0.08 - 2.3 [s]	2.3 [s]
Zero Padding	1, 2	2
Hamming Window in range	- No - Yes	- Yes
Hamming Window in azimuth	- No - Yes	- Yes
Posting Rate	20 - 17825 [Hz]	640 [Hz]
Extension Factor in range	1, 2	1
L2 options		
Threshold for the OCOG retracker	0 - 1	0.8
Number of estimates in the MultiPTR retracker	0 - 10	3

Table 3.1: *SMAP Options*

PTR and MultiPTR

A point target response (PTR) retracker is a numerical retracker using experimental algorithm [Tourain et al., 2021]. PTR retracker fits the main peak of waveform by modeling the radar PTR as a square sinc function. The model is appropriate for retraking single point waveforms [CLS team]. MutliPTR retracker fits multi peaks of waveform with PTR retracking and indicates the number of peaks to be retracked. The retracker return retracking parameters for each individual peak.

Chapter 4

Result and Discussion

In this chapter, the water level time series are generated over Itaparica, Mississippi and São Francisco. Meanwhile, for each location, the waveforms of two selected points in this area with different retrackers and different processing configurations are created. Three groups of data are used in this chapter for comparison:
- the official product of Sentinel-3
- the SARvatore product of Sentinel-3
- the SMAP product of Sentinel-3

The official products are processed by program AltBundle+. AltBundle+ is a matlab-based program developed by University Stuttgart using Level-2 products to generate water level time series, outliers, radargram stack, etc.

For SARvatore product, there are 7 configurations with 4 retrackers (SAMOSA2, SAMOSA3, SAMOSA+ and SAMOSA++). The configurations are listed as:

Option Name	Inland Water 80 Hz	Inland Water 20 Hz	Default 80 Hz	Default 20 Hz	Hamming Window	Zero Padding	Range Walk
Data Posting Rate	- 80 Hz	- 20 Hz	- 80 Hz	- 20 Hz	20 Hz	20 Hz	- 20 Hz
Range Walk Correction	- No	- No	- No	- No	- No	- No	- Yes
Hamming weighting Window	-Yes	-Yes	- No	- No	- Yes	- No	- No
Exact Beam-Forming	- Approx.	- Approx.	- Approx.	- Approx.	- Approx.	- Approx.	- Exact
FFT Zero-Padding	-Yes	-Yes	- No	- No	- No	- Yes	- No
Radar Receiving Window Size (range bins)	- 128X2	- 128X2	- 128	- 128	- 128	- 128	- 128

Table 4.1: *SARvatore Config Options*

For Itaparica, the configuration Inland Water 80 Hz and Inland Water 20 Hz are inherited from configuration Inland Water from Table 2.1. And the configuration Default 80 Hz and Default 20 Hz are from configuration Official S3 in Table 2.1. The configuration Hamming Window, Zero Padding and Range Walk are based on the configuration Default 20 Hz with corresponding changes.

For SMAP product, the configurations are based on the configuration Hydro in Table 3.1. The 4 configurations are shown in the Table 4.2 below. Config 1 stands for the standard Hydro configuration, which means with Zero Padding and Hamming Window in both range and azimuth. Config 2 represents the configuration without Zero Padding and Hamming Window, while Config 3 applies only Zero Padding and Config 4 applies only Hamming Window.

Option name	Config 1 zp = 2, hm = 1	Config 2 zp = 1, hm = 0	Config 3 zp = 2, hm = 0	Config 4 zp =1, hm = 1
Zero Padding	2	1	2	1
Hamming Window in range	- Yes	- No	- No	- Yes
Hamming Window in azimuth	- Yes	- No	- No	- Yes

Table 4.2: *SMAP Config Options*

Each case study has a location map. First we compare the water level time series of each case study under 5 different processing assumptions. Then we compare waveforms in different configurations and retrackers in the same configuration. For Itaparica, we also provide additional DDMs and RIPs of selected points in this area.

4.1 Itaparica

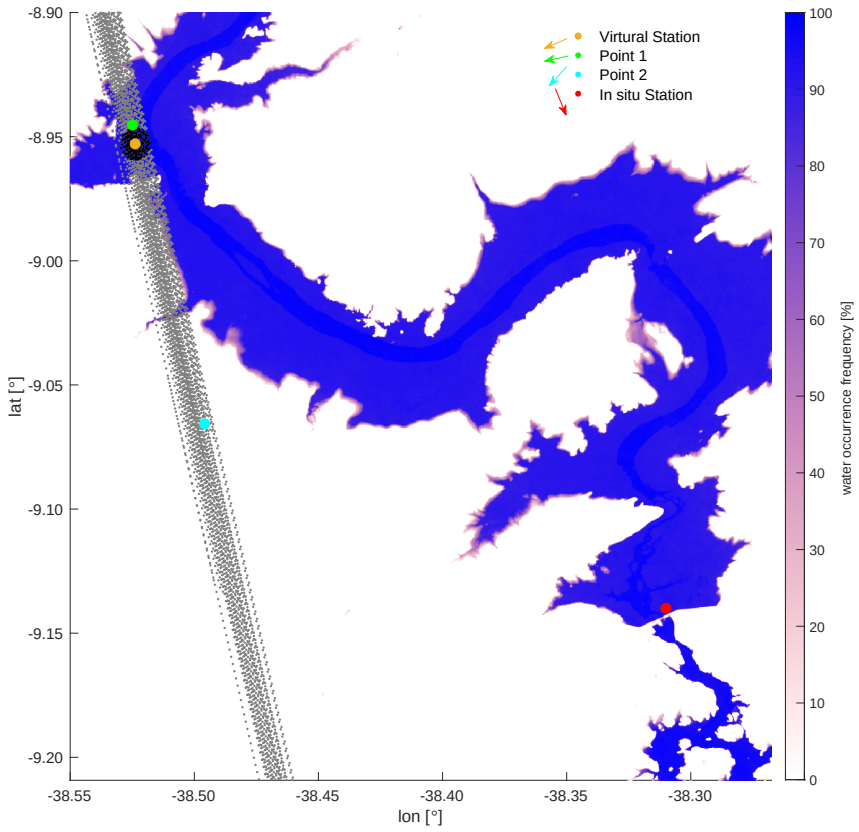

Figure 4.1: *Location of Itaparica*

The water level time series from June 2016 to October 2020 are shown in Figure 4.2 to Figure 4.6. Figure 4.2 shows the water level time series with different retrackers and same configuration Inland Water 80 Hz using SARvatore. We can see that the overall trend of each result is same as

in situ data, but there is a difference of about 1 m with the in situ data. Compared to in situ data, the obtained results with 4 retrackers have a greater fluctuation. Specifically, the results for SAMOSA+ and SAMOSA++ are more stable than those for SAMOSA2 and SAMOSA3. As can be seen from the figures, at the beginning of 2019 and the beginning of 2020, both SAMOSA2 and SAMOSA3 provide results that differ from the reference value by about 3 m. Compared to the results with different SAMOSA retrackers, the result of AltBundle+ with OCOG have about the same performance until 2020. Starting in mid-2020, the result of official product with OCOG falls exactly on the line of in situ data, while other results have a greater difference.

Figure 4.3 presents the results with different configurations in Table 4.1 and same retracker SAMOSA++ using SARvatore. The results for all groups show the same trend for most of the time, with the main differences in 2016 and 2020, and these poorer results are from groups SARvatore Default 80 Hz (orange), SARvatore Default 20 Hz (purple) and SARvatore with Hamming Window (grey). It can also be seen from the graph that between 2017 and late 2019, the configurations SARvatore Default 20 Hz and SARvatore with Hamming Window (grey) lead to a significant overestimation of water level, while the differences for the other groups are not large.

Figure 4.4 represents the water level time series with different retrackers and same configuration (with zero padding and hamming window) using SMAP. From the figure we can see that MultiPTR2 and MultiPTR3 deliver generally better results than the other three groups. As with SARvatore, the individual SMAP results also significantly differ from the in situ data after 2020, with a maximum difference of about 3 m. Figure4.5 shows the results with different configurations and same retracker OCOG using SMAP. The configurations yield low disparity in results, with all 4 configurations giving the same significant difference in results in late 2017 and early 2019. Figure 4.6 shows the difference between the best result of SARvatore and the best result of SMAP. Compared to SARvatore and SMAP, official Product with OCOG offers a better result.

Figure 4.7, Figure 4.8 and Figure 4.9 indicate the bias, RMSE and correlation for each configuration and each retracker, respectively. Overall, SARvatore's results are better than SMAP's. The bias of SARvatore is between 0.65 m and 1.7 m, while the bias of SMAP is more than 3 m for the other 4 retrackers except for OCOG which is around 1.2 m. In terms of SARvatore itself, the Range Walk with SAOMSA2 offers the best result with the best RMSE 0.5138 m and the best correlation 0.8103. And for SMAP, the best result is from Config 3 (zp=2 hm=0) with the best RMSE 0.8549 m and the best correlation 0.7077.

Figure 4.10, Figure 4.11 and Figure 4.12 show the along track profiles of Itaparica.

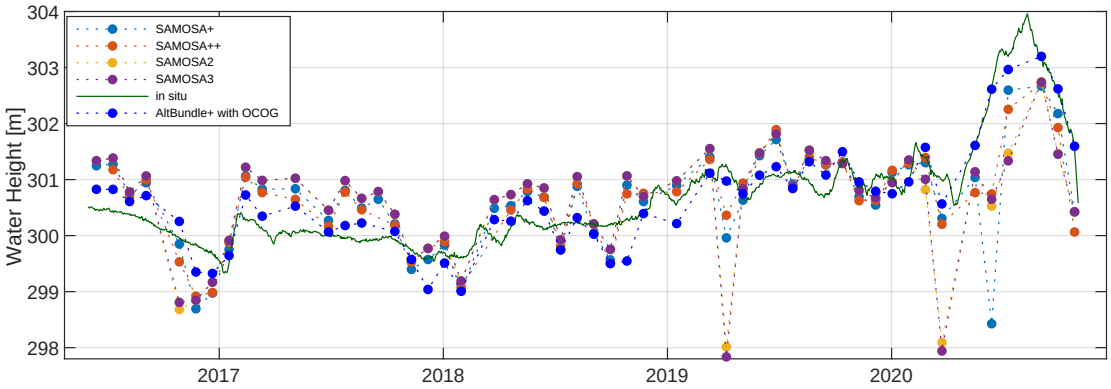

Figure 4.2: *SARvatore with Different Retrackers (Config-Inlandwater 80 Hz) of Itaparica*

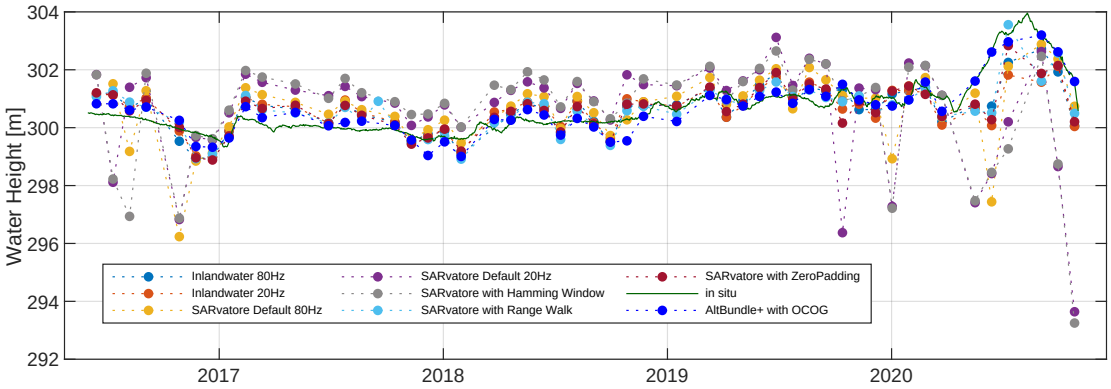

Figure 4.3: *SARvatore with Different Configs (Retracker-SAMOSA++) of Itaparica*

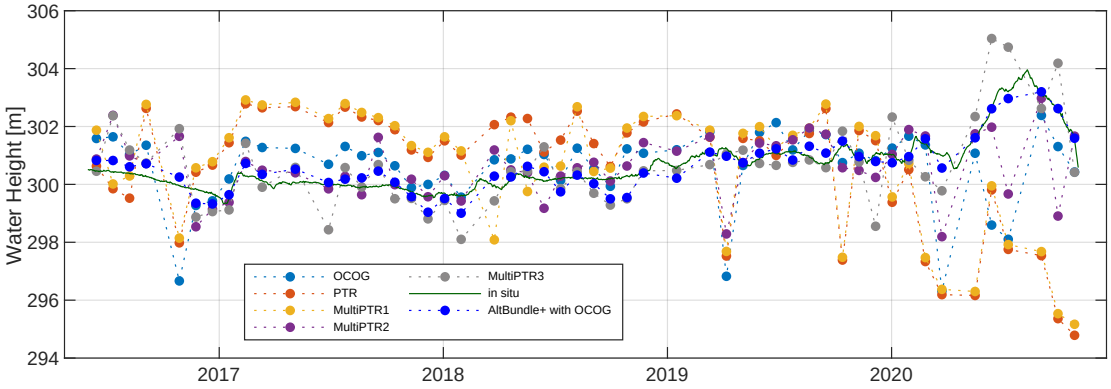

Figure 4.4: *SMAP-FFSAR with Different Retrackers but Same Config zp=2 hm=1 of Itaparica*

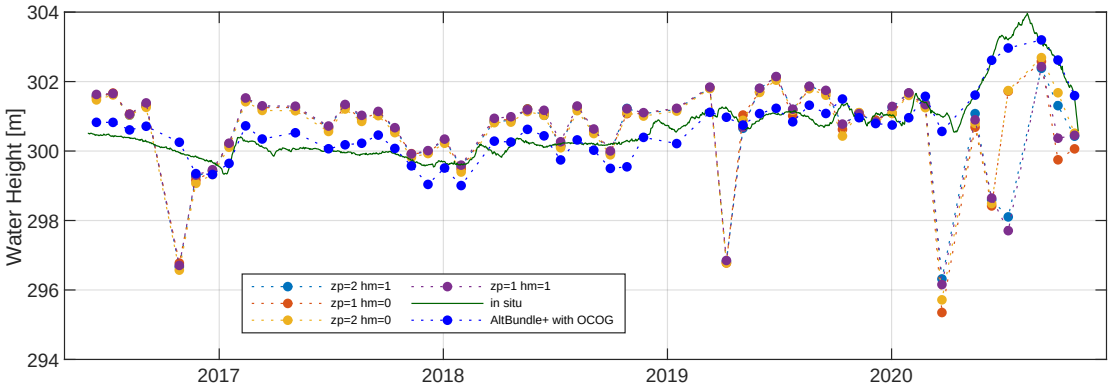

Figure 4.5: *SMAP-FFSAR with Different Configs and Same Retracker OCOG of Itaparica*

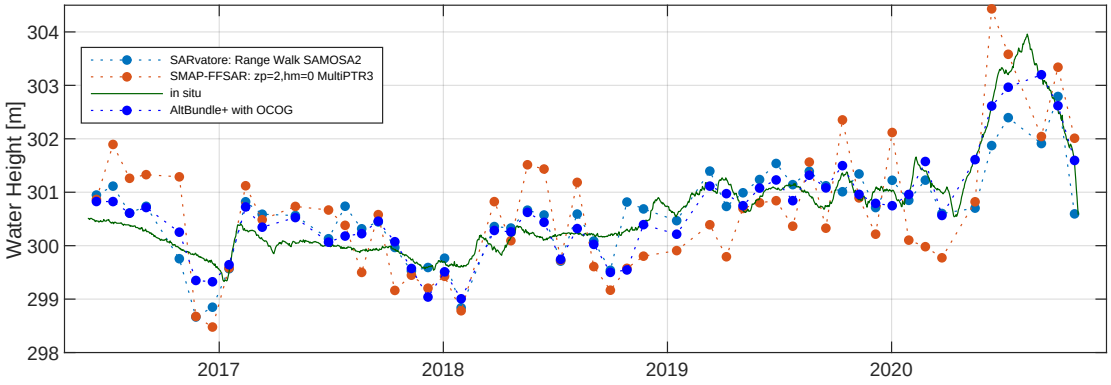

Figure 4.6: *SARvatore vs SMAP of Itaparica*

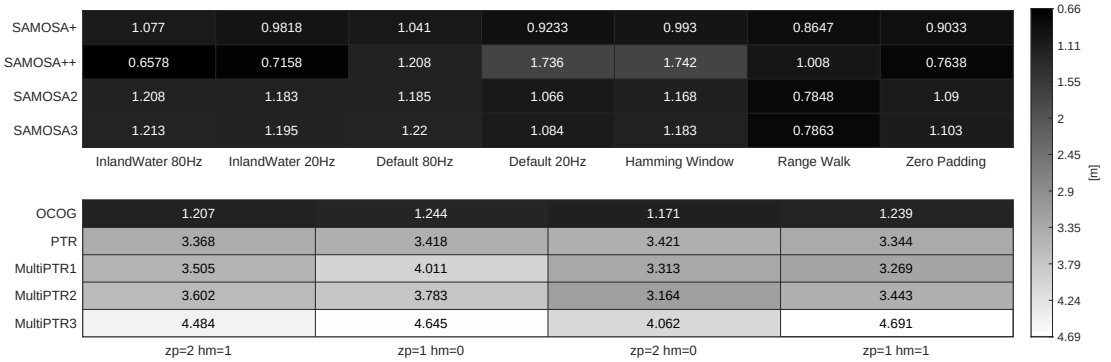

Figure 4.7: *Bias[m] with Different Configs and Different Retrackers of Itaparica (with Official OCOG* 0.5299 *m)*

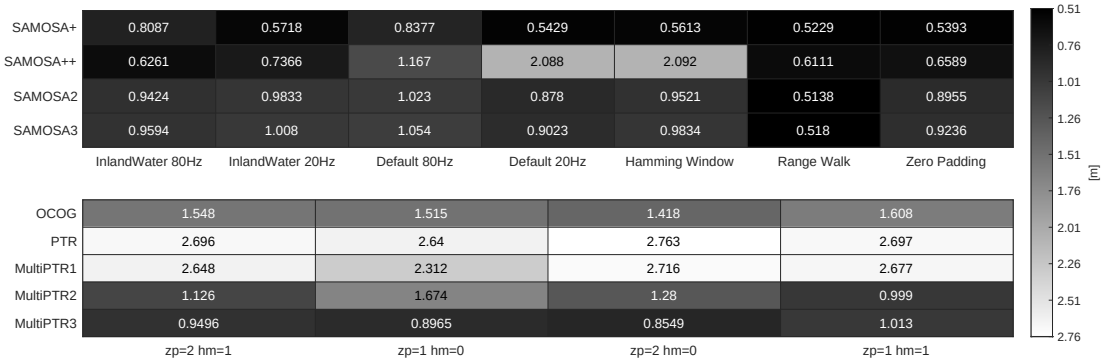

Figure 4.8: *RMSE[m] with Different Configs and Different Retrackers of Itaparica (with Official OCOG* 0.3236 *m)*

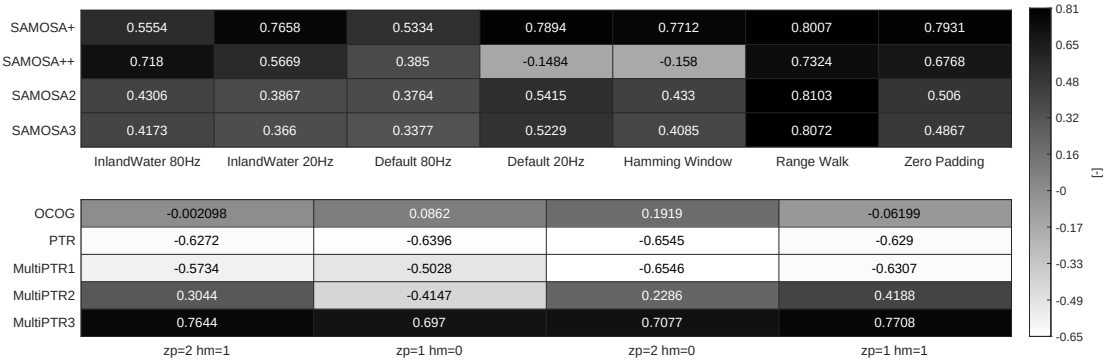

Figure 4.9: *Correlation of In situ Data with Different Configs and Different Retrackers of Itaparica (with Official OCOG* 0.9343

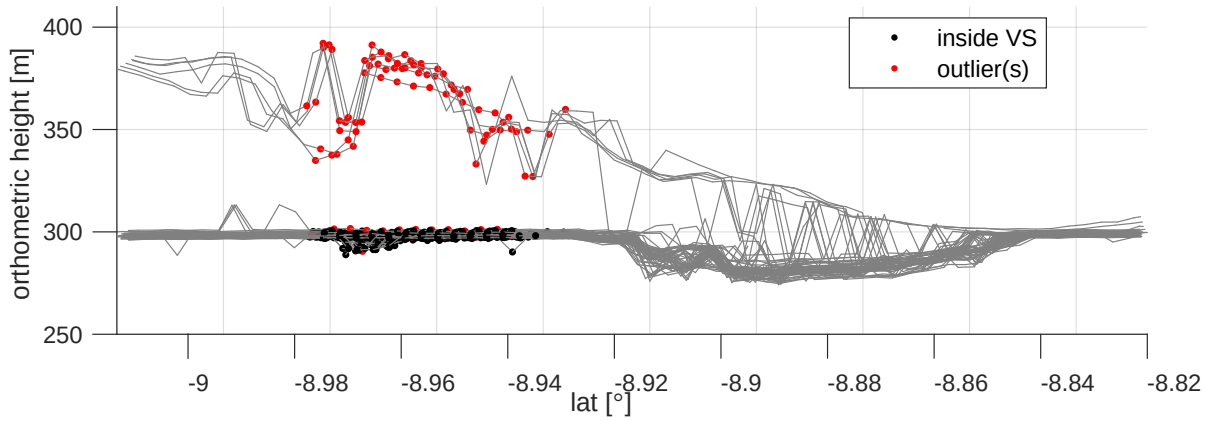

Figure 4.10: *Along Track Profile of Itaparica with Official Product (Retracker: OCOG)*

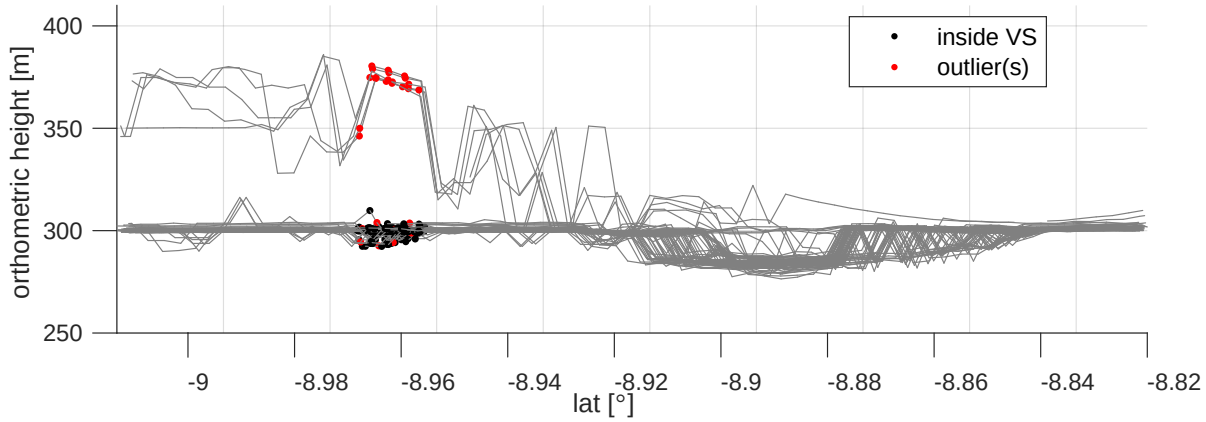

Figure 4.11: *Along Track Profile of Itaparica with SARvatore (Config: Default 20 Hz with SAMOSA++)*

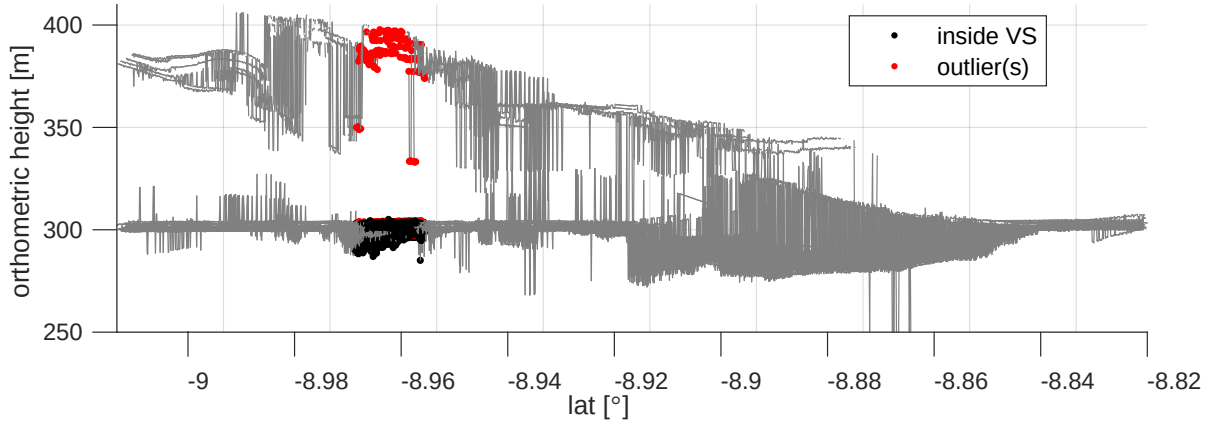

Figure 4.12: *Along Track Profile of Itaparica with SMAP (Config: zp=1, hm=0 with OCOG)*

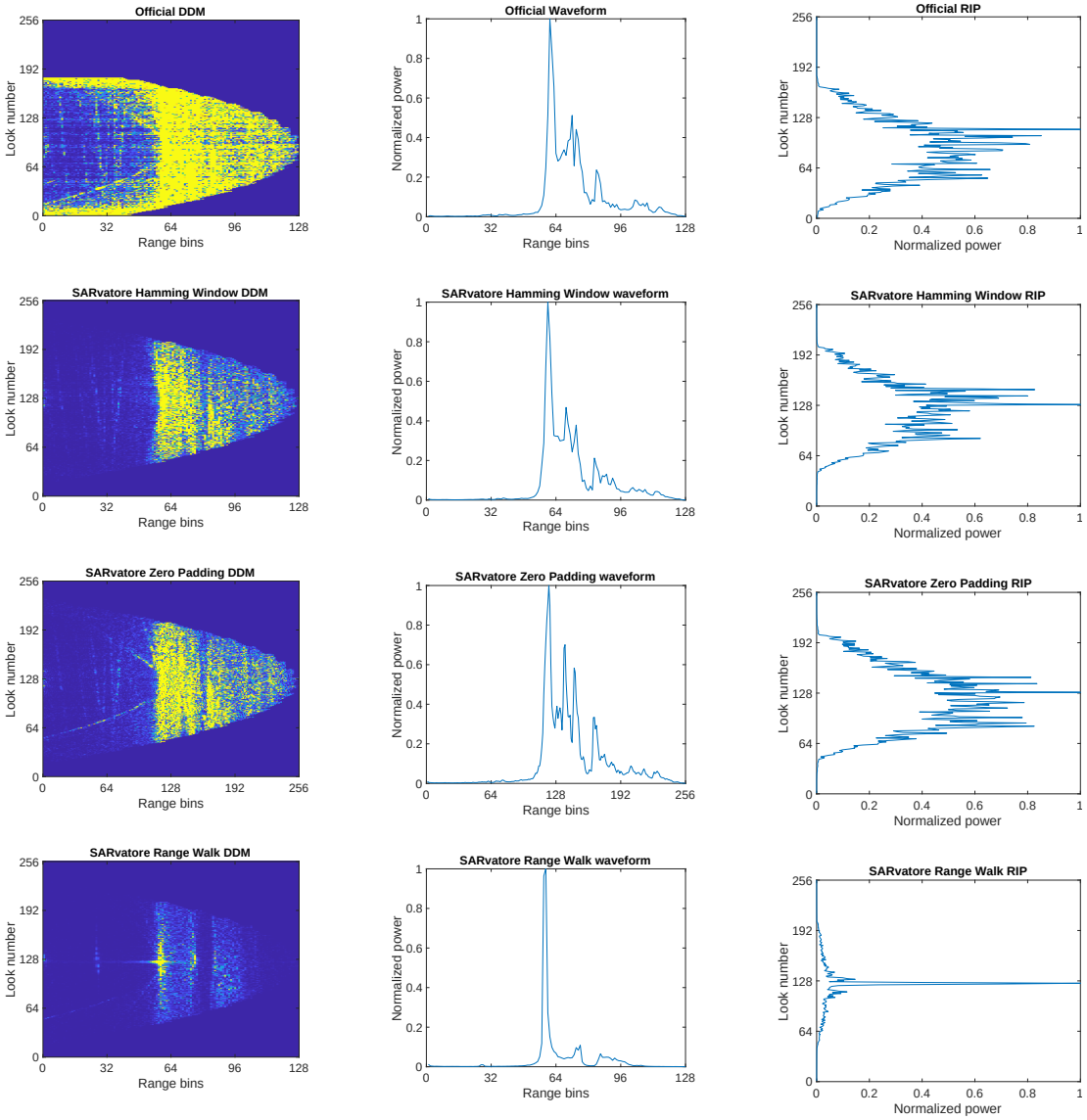

Figure 4.13: *DDM, Waveform and RIP of Point 1 with Different Configs (first)*

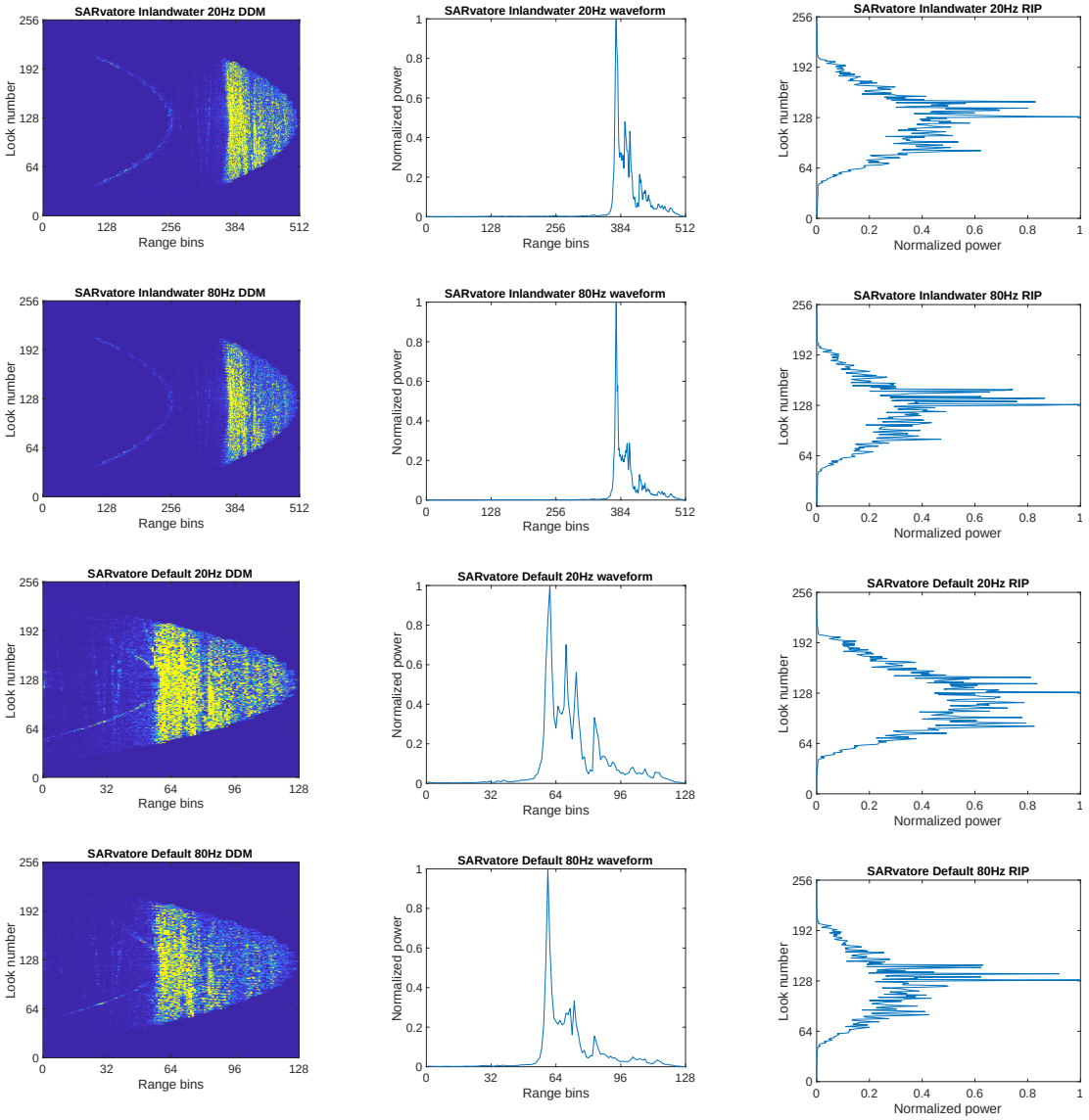

Figure 4.14: *DDM, Waveform and RIP of Point 1 with Different Configs (second)*

Two points are selected to analyze the waveforms and retrackers, with their locations depicted in Figure 4.1. The DDM, waveform and RIP of point 1 with different configurations using SARvatore are represented in Figure 4.13 and Figure 4.14. From these plots, it can be concluded that the resulting DDM can vary greatly depending on the steps taken to process the data, and the resulting waveforms and RIPs are therefore very different.

The first point is located in the center of the lake. Figure 4.15 to Figure 4.17 show the waveforms of point 1 with different configurations. It can be seen that the waveforms generated by different configurations are similar except for the Range Walk. And the positions of the peaks are not the same for configurations expect for Inland Water 80 Hz and Inland Water 20 Hz.

Compared to other configurations, The option Extension Window of Inland Water 20 Hz and Inland Water 80 Hz are set to 128×2. The consequence of this is that the length of range bins is doubled. In order to better compare waveforms, only the second half of Inland Water's waveform is taken. Figure 4.18 and Figure 4.19 show waveforms with different configurations using SMAP. Although the overall waveform trend is different for each configuration, the figures reveal that neither zero padding nor hamming window has significant effect on the position of the waveform peaks. Figure 4.20 indicates the comparison of waveforms between SARvatore, SMAP, and the official product. To make the comparison fair, the minimal configuration is used for both. From the figure, we can see that despite using the same configuration, the waveforms of the three are not identical, but the peak positions of SARvatore and official product are very similar.

Figure 4.21, Figure 4.22 and Figure 4.23 represent the different retrackings for the official product, SARvatore and SMAP. It is clear to see that the different retrackers offer very similar retracker bins in case of official product and SARvatore, while in the case of SMAP, the retracker bins have significant differences.

The second point is far away from lake Itaparica (see Figure 4.1), in that circumstances, neither SARvatore nor SMAP offers meaningful results, therefore there is also no retracking result. On the contrary, the official product works normally in this case and provides a waveform which is then successfully retracked. Figure 4.24 to Figure 4.29 illustrate the waveforms with different configurations and Fiugre 4.30 to Figure 4.32 represent the respective retracking.

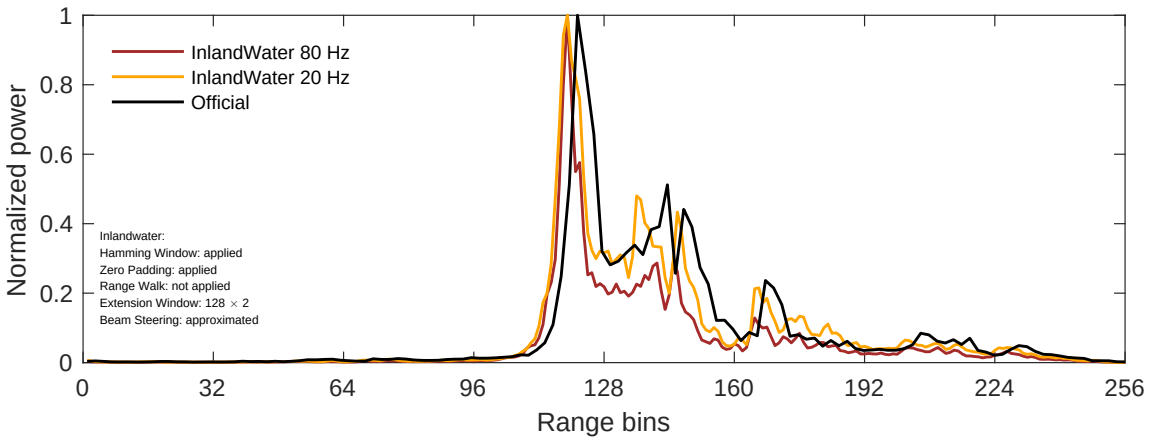

Figure 4.15: *SARvatore Waveform with Config Inlandwater of Point 1 from Itaparica*

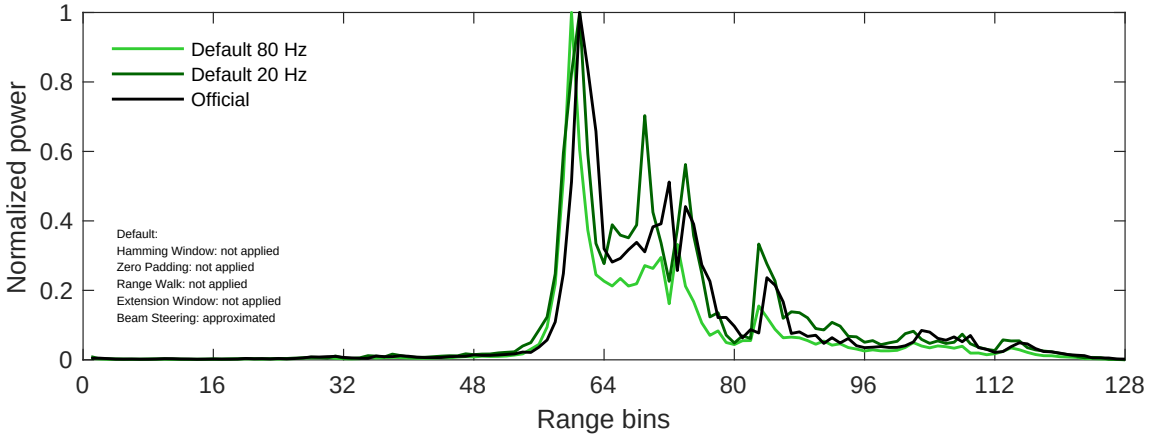

Figure 4.16: *SARvatore Waveform with Default Config of Official S3 Product of Point 1 from Itaparica*

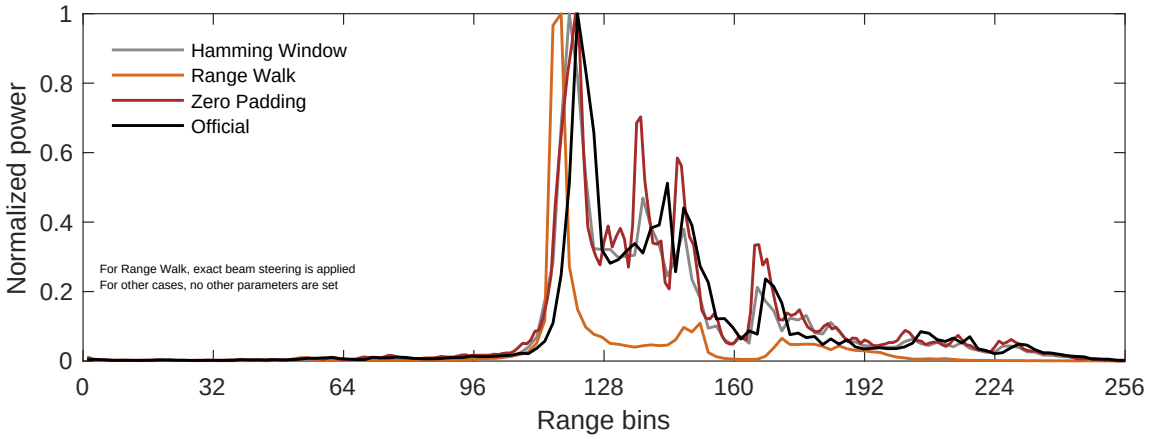

Figure 4.17: *SARvatore Waveform with Different Settings versus the Official Waveform of Point 1 from Itaparica*

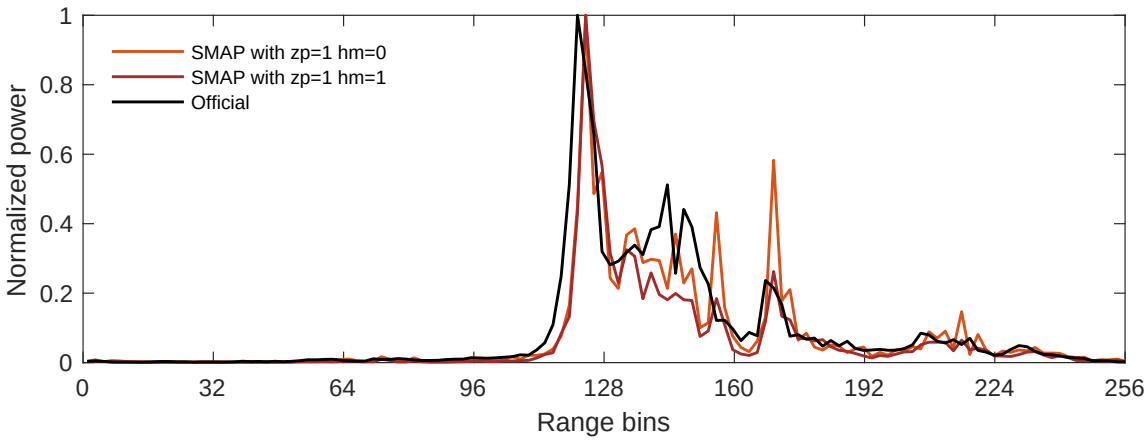

Figure 4.18: *SMAP Waveform With and Without Hamming Window of Point 1 from Itaparica*

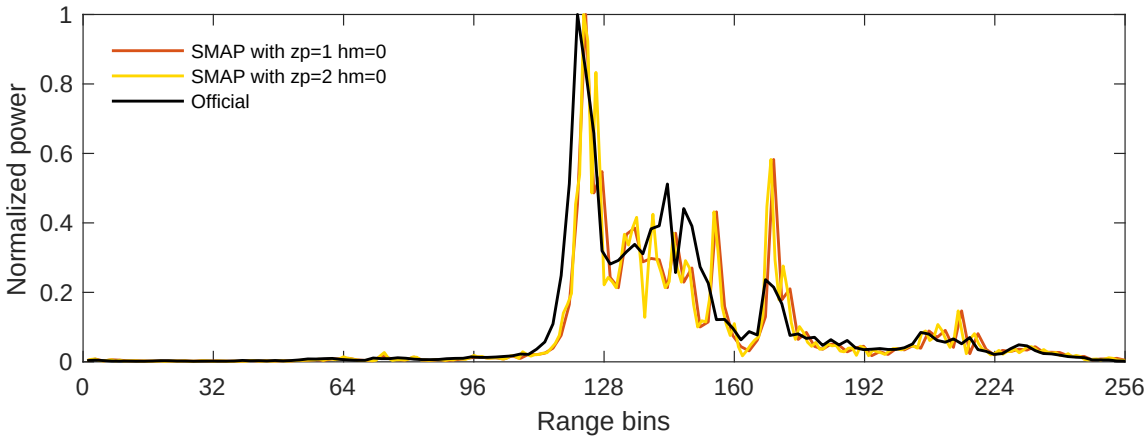

Figure 4.19: *SMAP Waveform With and Without Zero Padding of Point 1 from Itaparica*

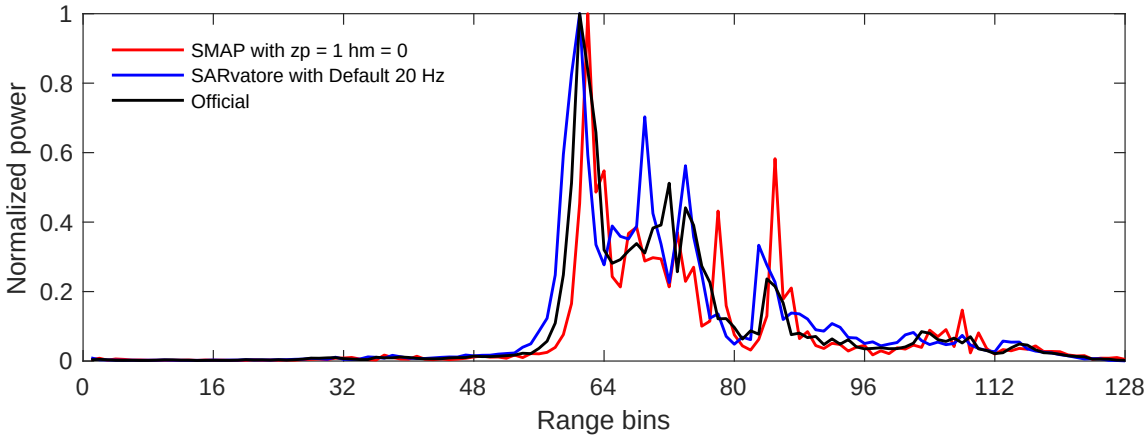

Figure 4.20: *SARvatore Waveform versus SMAP Waveform of Point 1 from Itaparica*

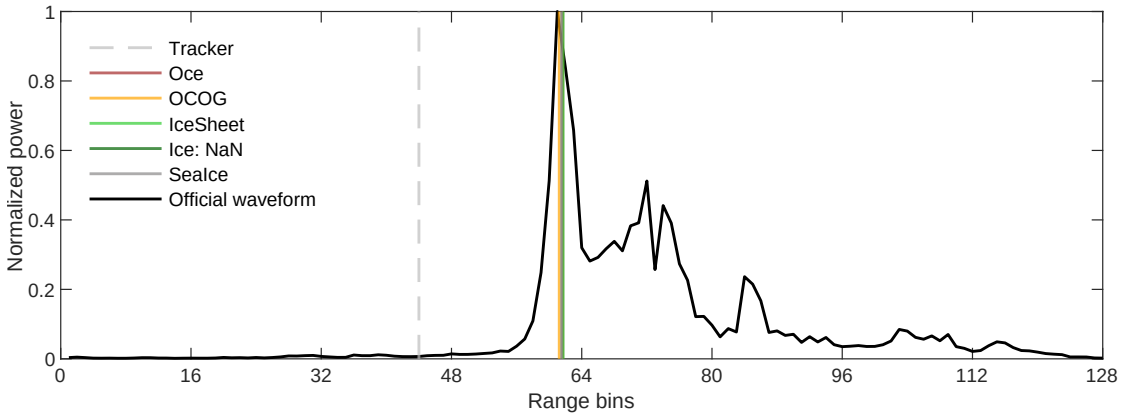

Figure 4.21: *Retracking for Official Waveform of Point 1 from Itaparica*

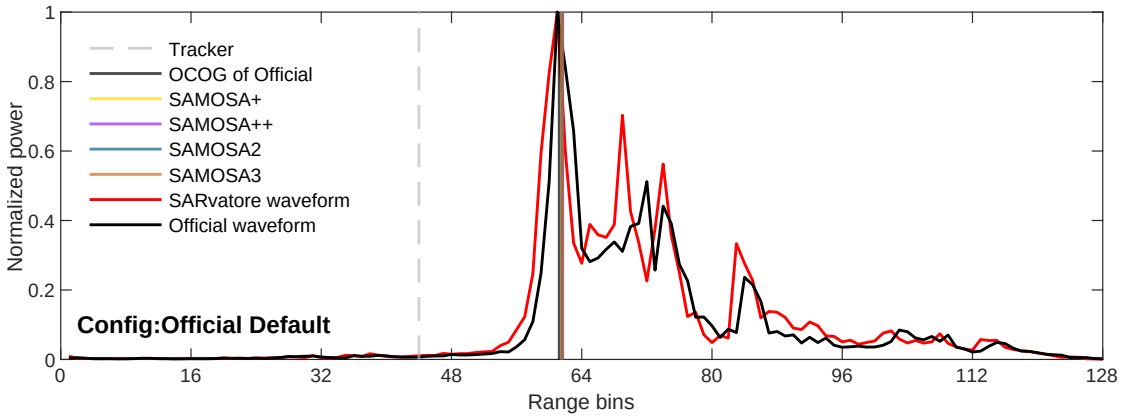

Figure 4.22: *Retracking for SARvatore Waveform of Point 1 from Itaparica*

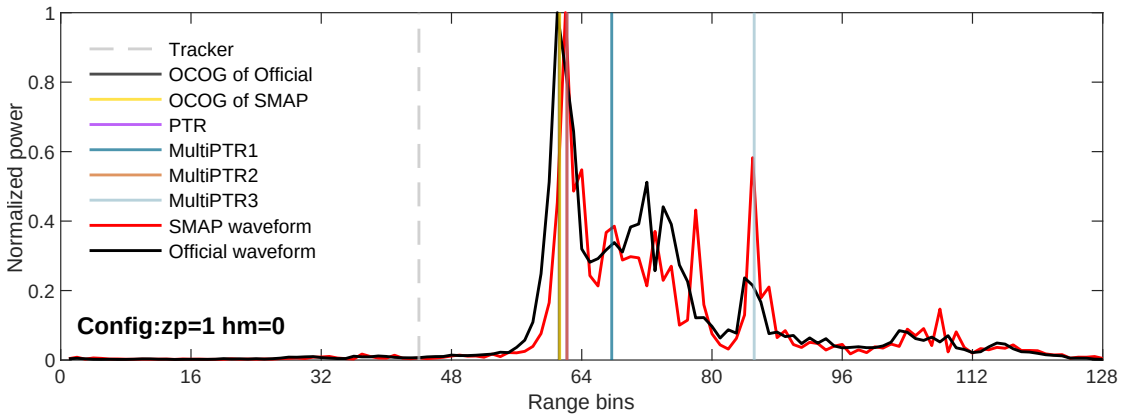

Figure 4.23: *Retracking for SMAP Waveform of Point 1 from Itaparica*

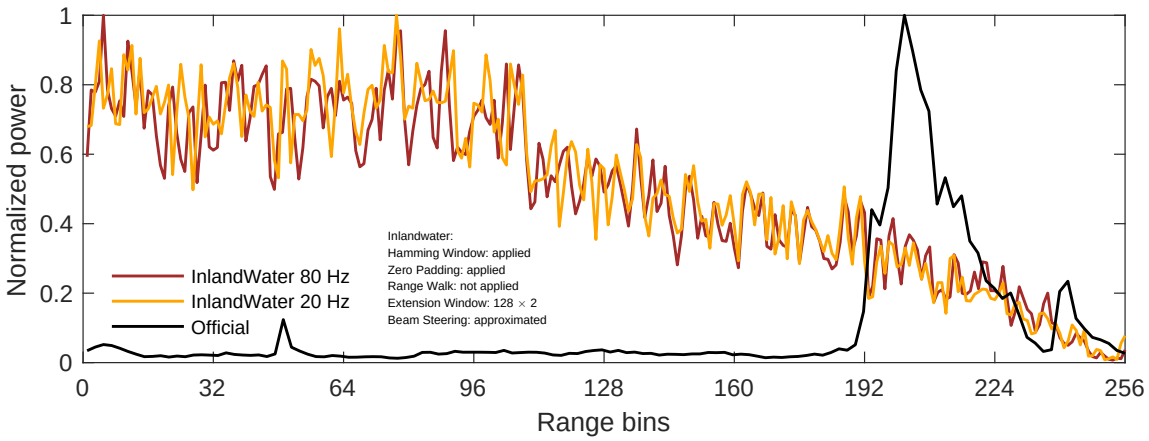

Figure 4.24: *SARvatore Waveform with Config Inlandwater of Point 2 from Itaparica*

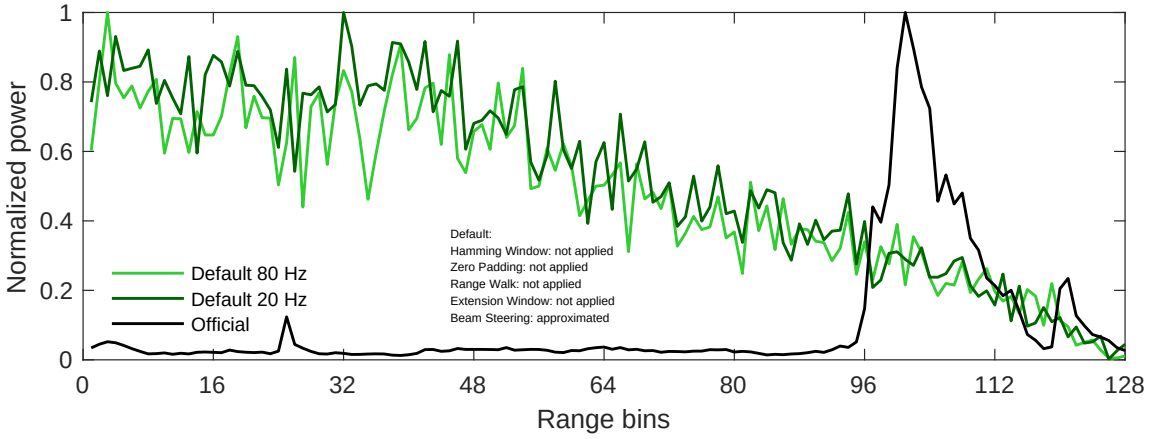

Figure 4.25: *SARvatore Waveform with Default Config of Official S3 Product of Point 2 from Itaparica*

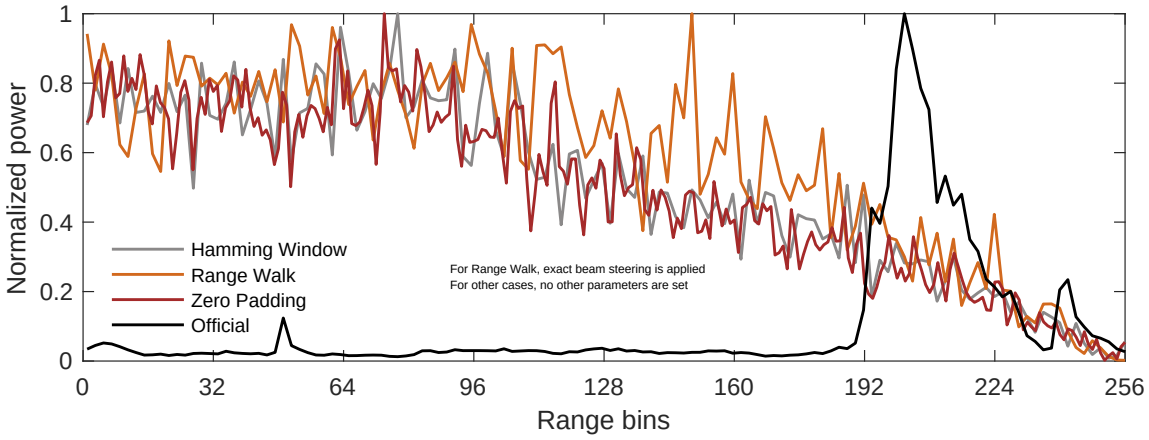

Figure 4.26: *SARvatore Waveform with Different Settings versus the Official Waveform of Point 2 from Itaparica*

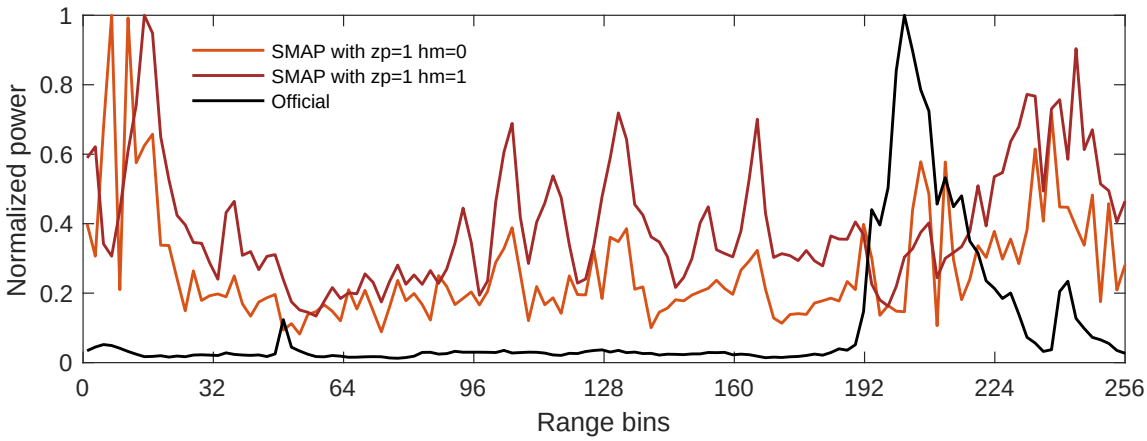

Figure 4.27: *SMAP Waveform With and Without Hamming Window of Point 2 from Itaparica*

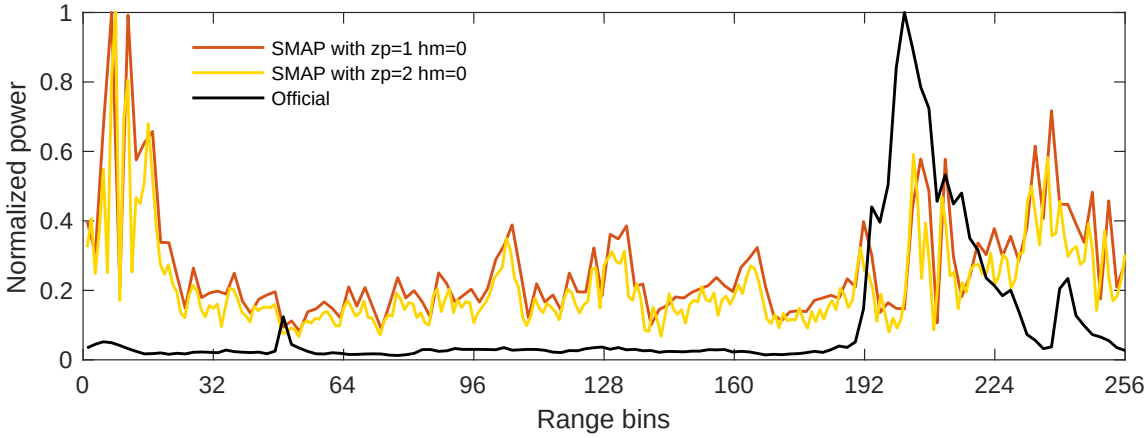

Figure 4.28: *SMAP Waveform With and Without Zero Padding of Point 2 from Itaparica*

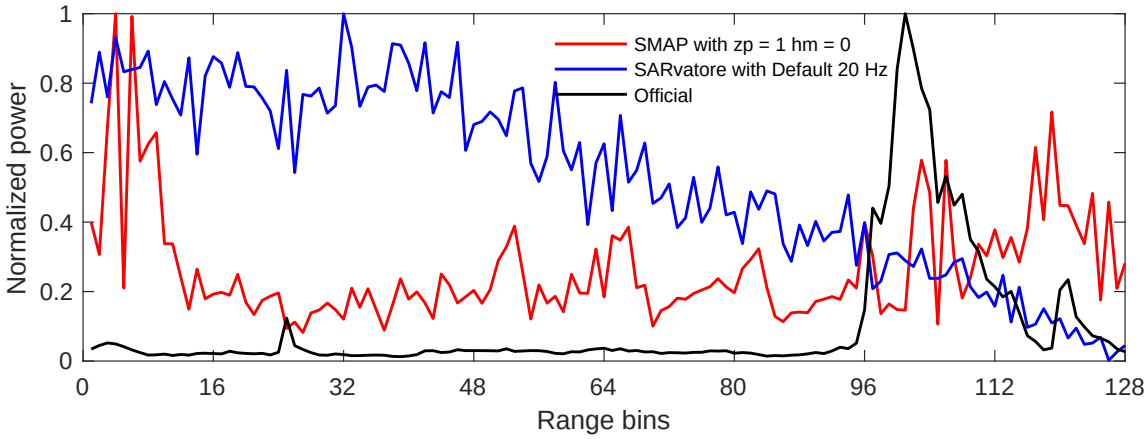

Figure 4.29: *SARvatore Waveform versus SMAP Waveform of Point 2 from Itaparica*

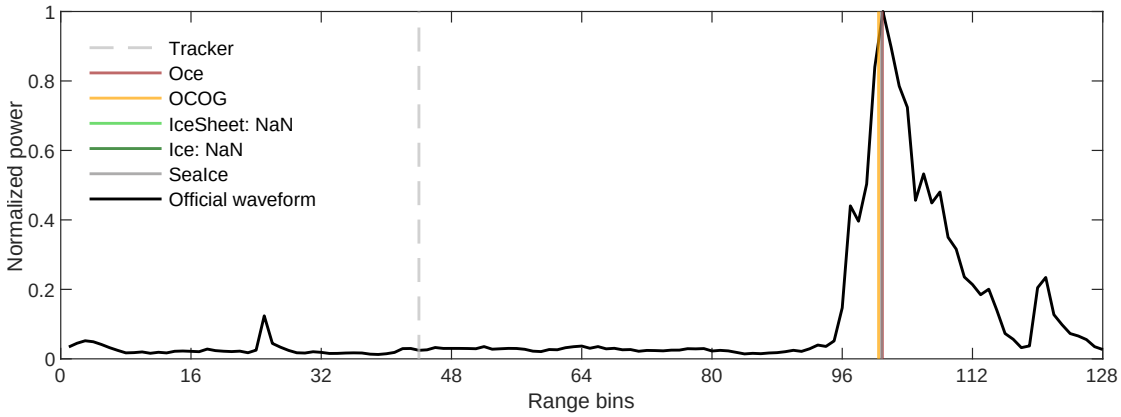

Figure 4.30: *Retracking for Official Waveform of Point 2 from Itaparica*

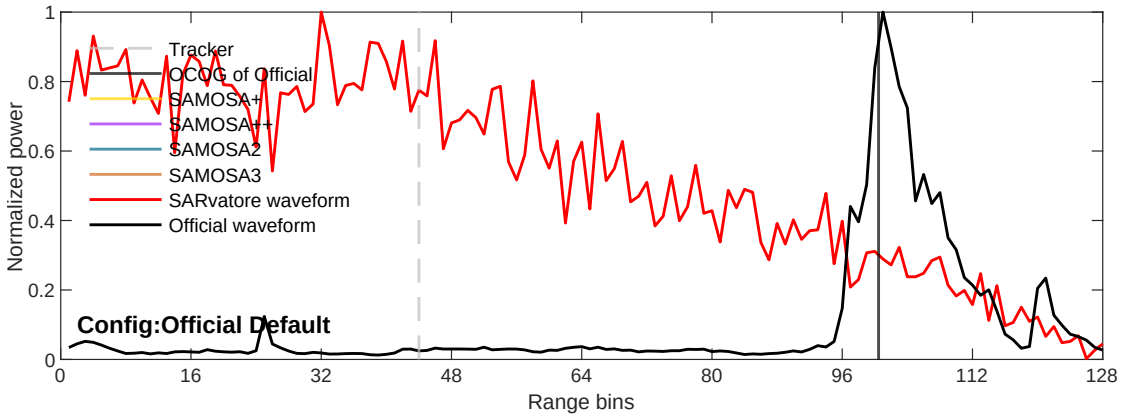

Figure 4.31: *Retracking for SARvatore Waveform of Point 2 from Itaparica*

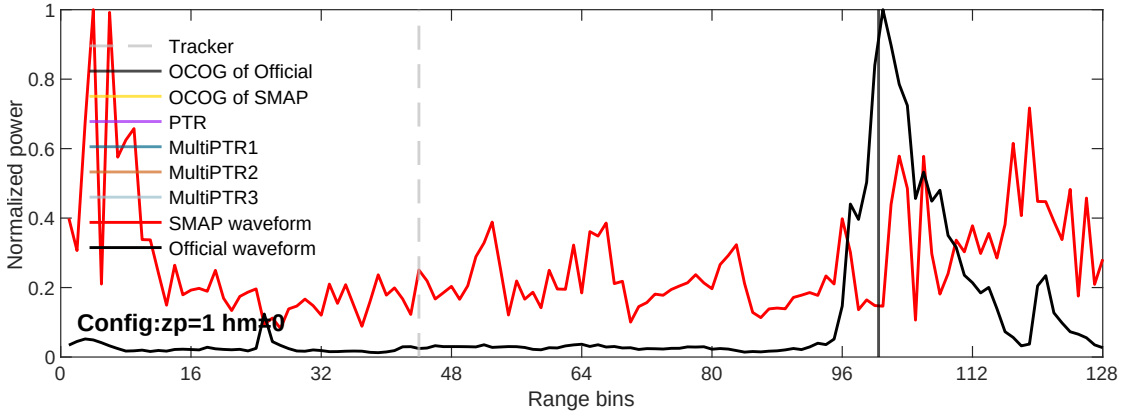

Figure 4.32: *Retracking for SMAP Waveform of Point 2 from Itaparica*

4.2 Mississippi

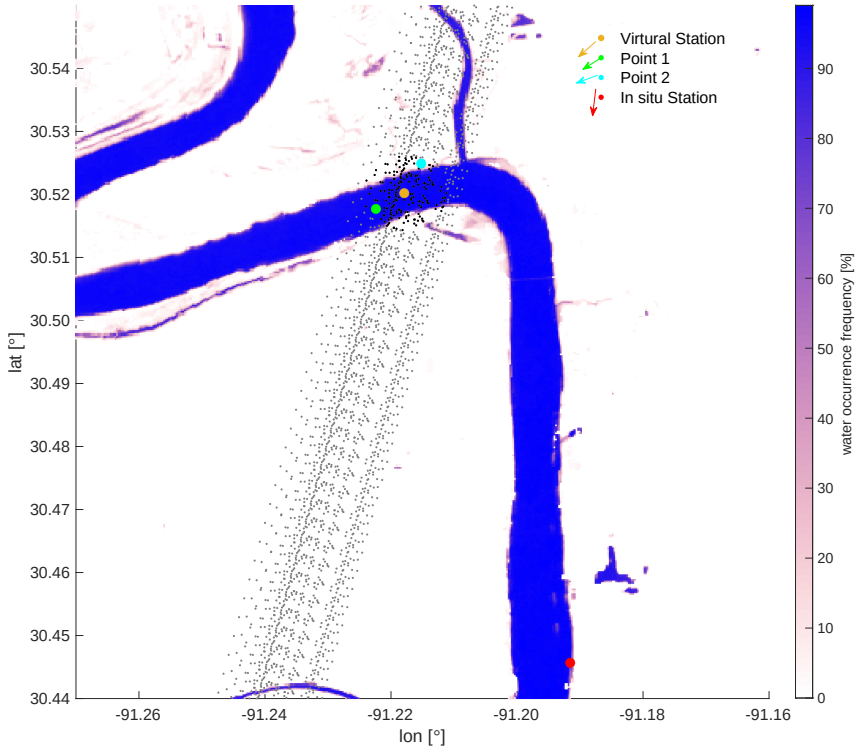

Figure 4.33: *Location of Mississippi*

For river Mississippi, the water level time series from June 2016 to October 2020 are generated. For SARvatore, from Figure 4.34 it can be seen that different retrackers offers similar results for the most of the time. Figure 4.35 shows that Range Walk generates a result which is significantly different from the other configurations. For SMAP, Figure 4.36 reveals that retracker MultiPTR3 and MultiPTR2 offer poor results in comparison to other retrackers and Figure 4.37 shows no distinct difference between different configurations except for mid-2017 and the end of 2019.

Figure 4.39, Figure 4.40 and Figure 4.41 describe the bias, RMSE and correlation for each configuration and each retracker, respectively. From the statistics, it can be seen that MultiPTR2 and MultiPTR3 do not perform well compared to other configurations of SARvatore and SMAP. The best of SMAP is Config 2 without zero padding and hamming window and with retracker PTR. The results of SARvatore are all very similar. On all counts, the best among SARvatore is Default 20 Hz with SAMOSA+. It is to be noticed that the correlations are clearly higher in Mississippi compared to Itaparica, besides the biases and RMSEs between in situ station and virtual station are not as large.

Figure 4.42, Figure 4.43 and Figure 4.44 show the along track profiles of Mississippi.

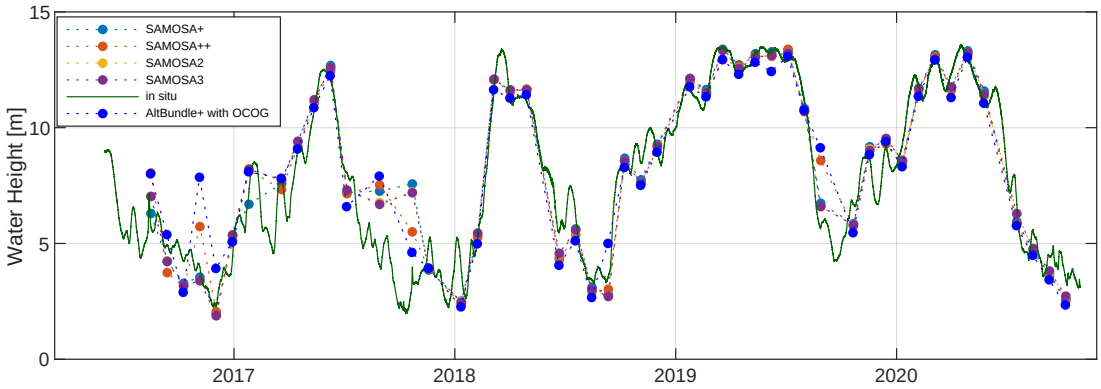

Figure 4.34: *SARvatore with Different Retrackers (Config-Inlandwater 80 Hz) of Mississippi*

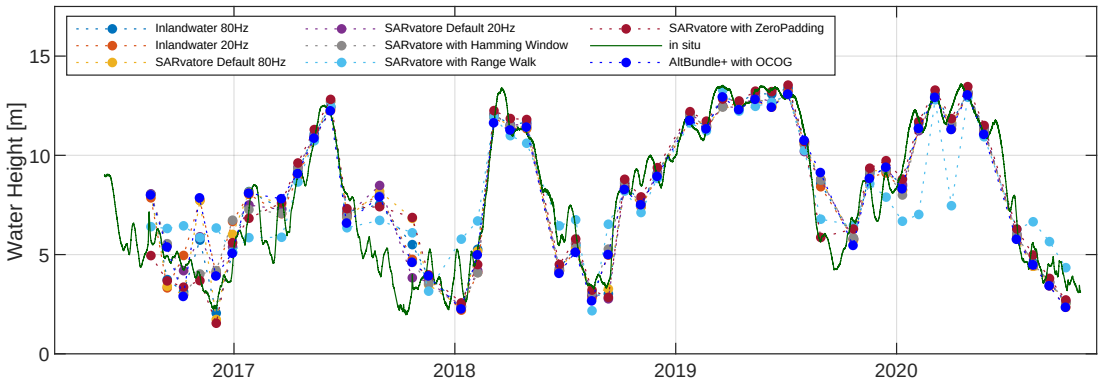

Figure 4.35: *SARvatore with Different Configs (Retracker-SAMOSA++) of Mississippi*

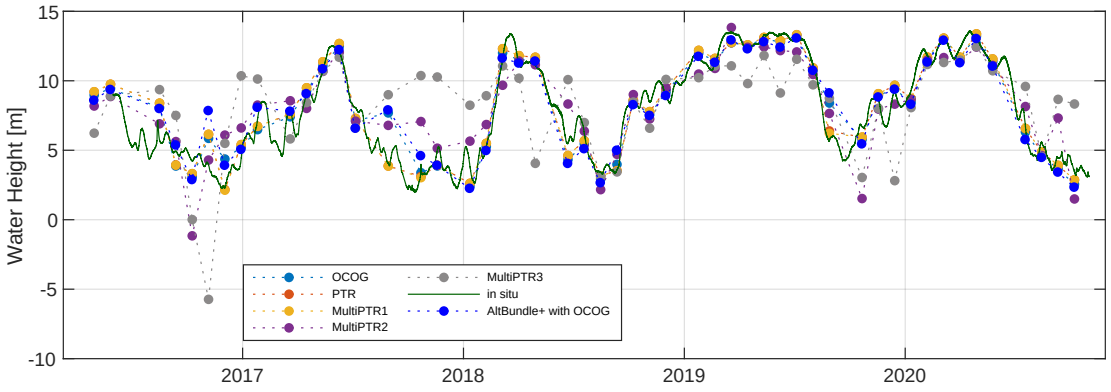

Figure 4.36: *SMAP-FFSAR with Different Retrackers but Same Config zp=2 hm=1 of Mississippi*

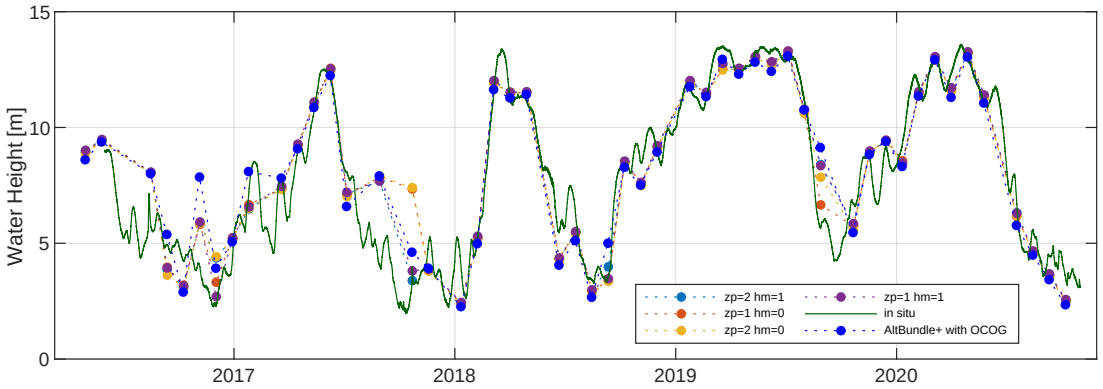

Figure 4.37: *SMAP-FFSAR with Different Configs and Same Retracker OCOG of Mississippi*

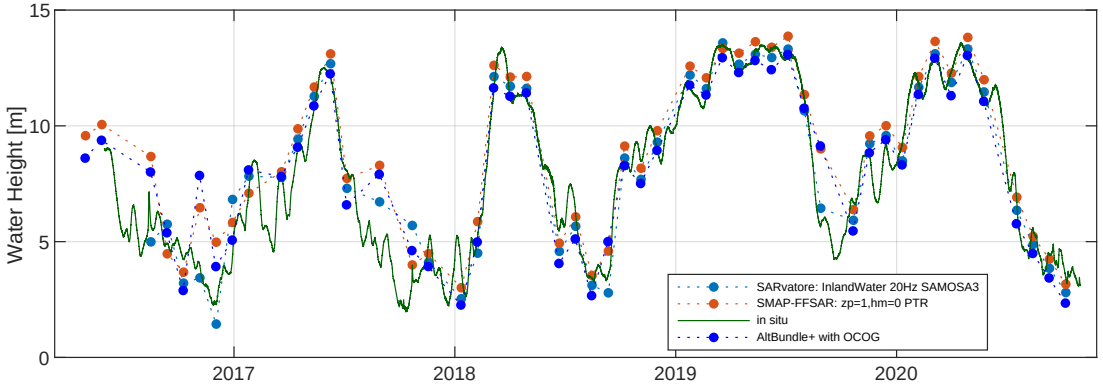

Figure 4.38: *SARvatore versus SMAP of Mississippi*

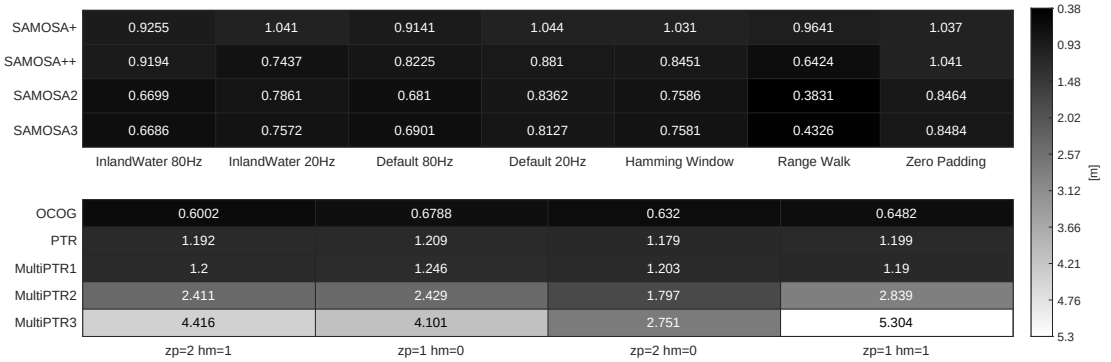

Figure 4.39: *Bias[m] with Different Configs and Different Retrackers of Mississippi (with Official OCOG* 0.4642 *m)*

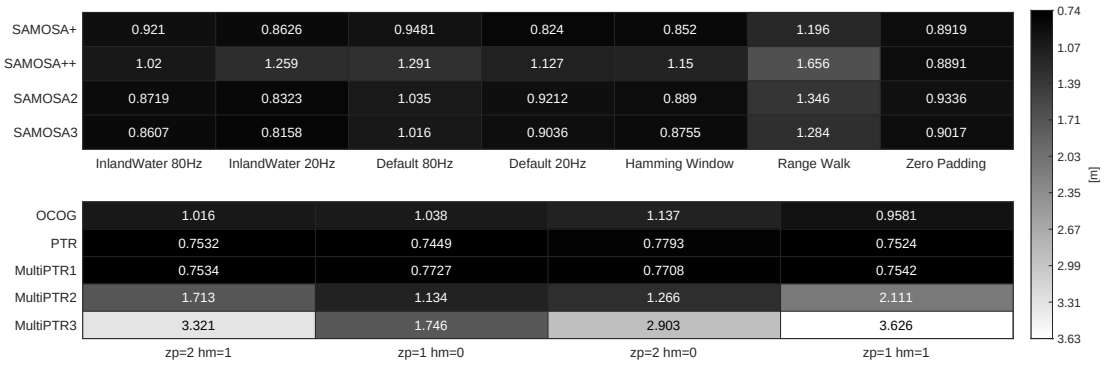

Figure 4.40: *RMSE[m] with Different Configs and Different Retrackers of Mississippi (with Official OCOG* 1.2426 *m)*

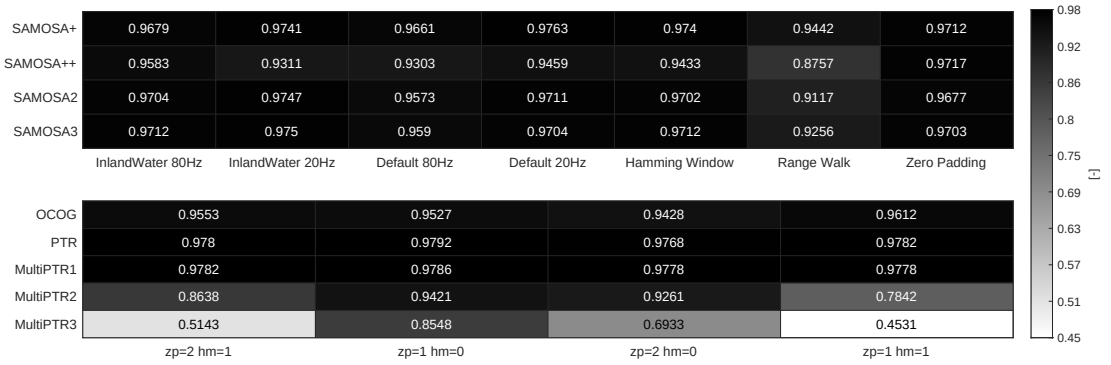

Figure 4.41: *Correlation of In situ Data with Different Configs and Different Retrackers of Mississippi (with Official OCOG* 0.9332*)*

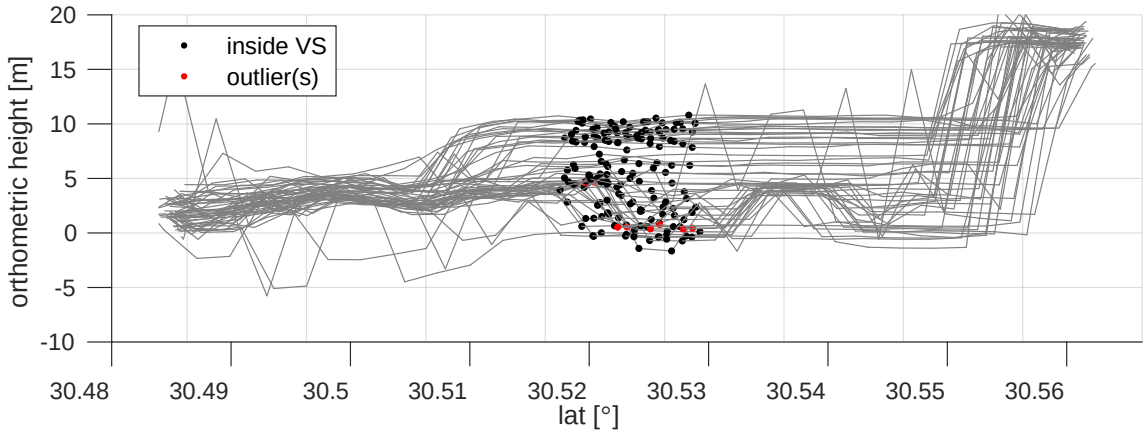

Figure 4.42: *Along Track Profile of Mississippi with Official Product (Retracker: OCOG)*

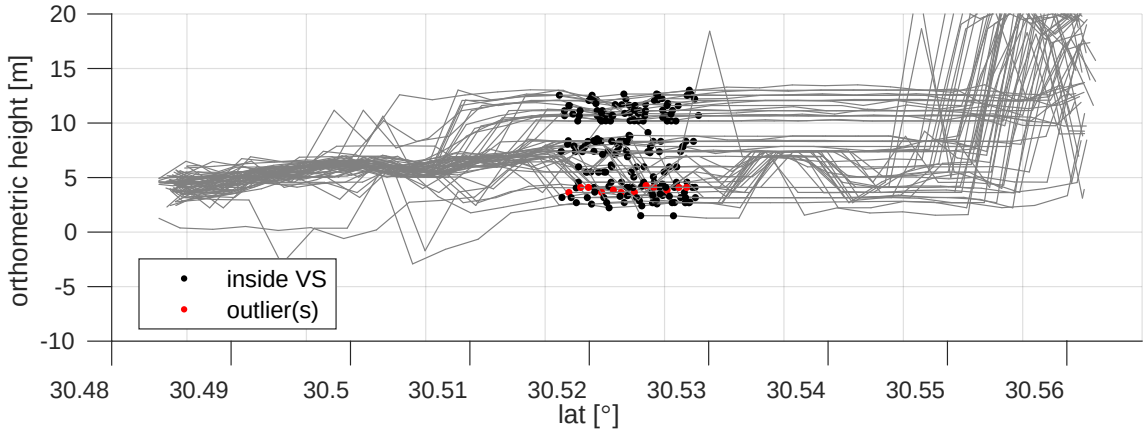

Figure 4.43: *Along Track Profile of Mississippi with SARvatore (Config: Default 20 Hz with SAMOSA++)*

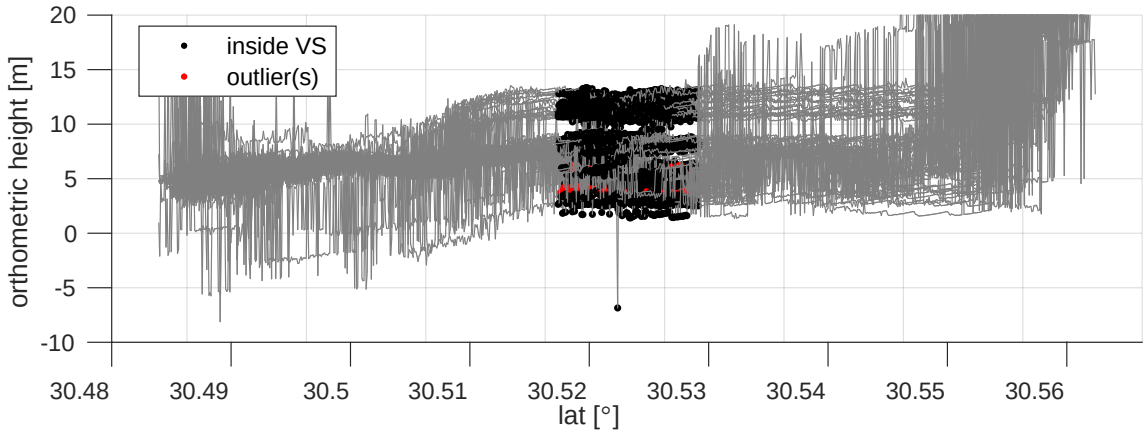

Figure 4.44: *Along Track Profile of Mississippi with SMAP (Config: zp=1, hm=0 with OCOG)*

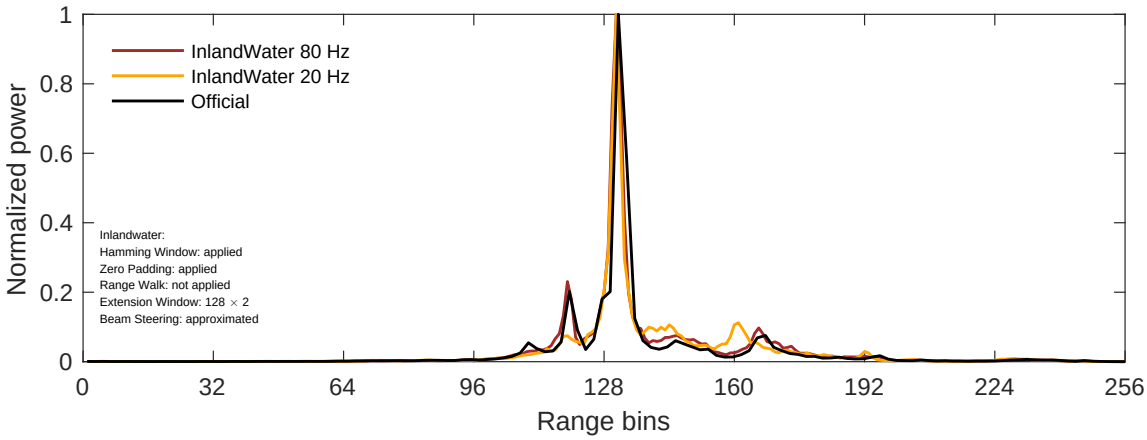

Figure 4.45: *SARvatore Waveform with Config Inlandwater of Point 1 from Mississippi*

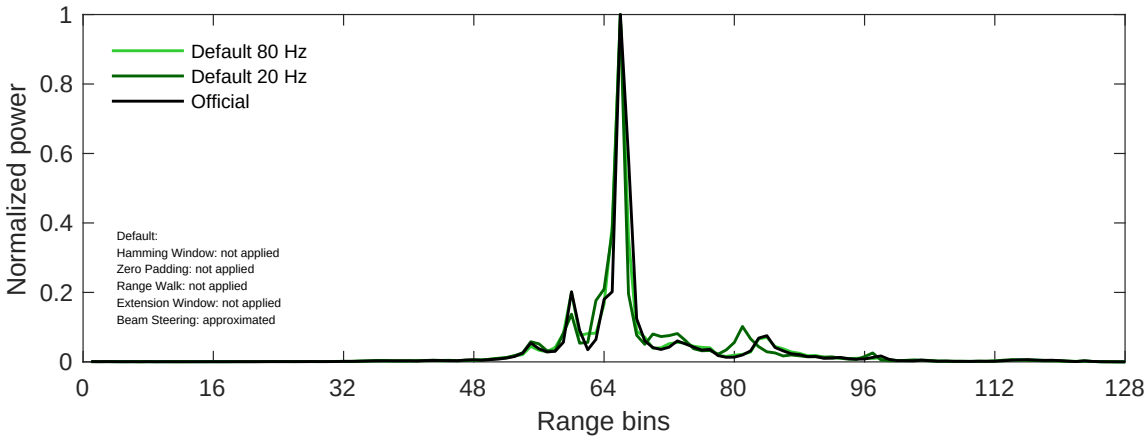

Figure 4.46: *SARvatore Waveform with Default Config of Official S3 Product of Point 1 from Mississippi*

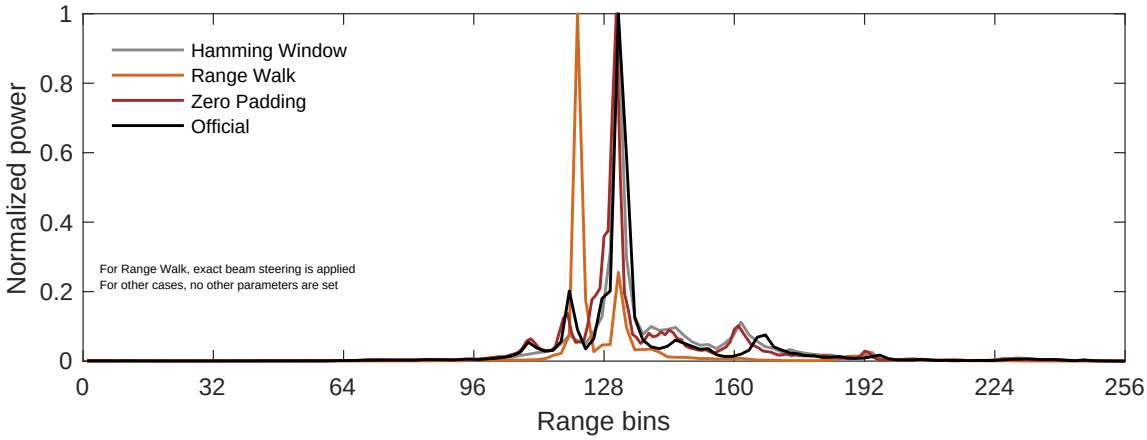

Figure 4.47: *SARvatore Waveform with Different Settings versus the Official Waveform of Point 1 from Mississippi*

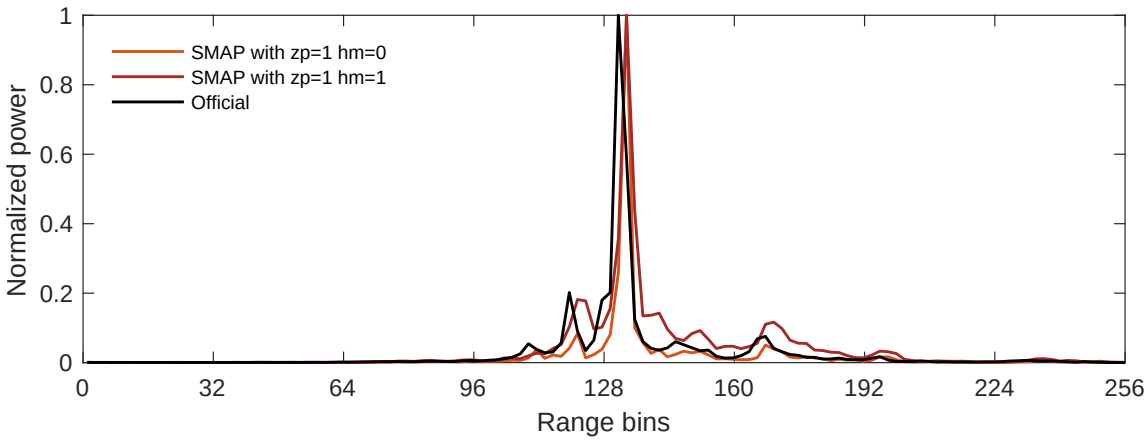

Figure 4.48: *SMAP Waveform With and Without Hamming Window of Point 1 from Mississippi*

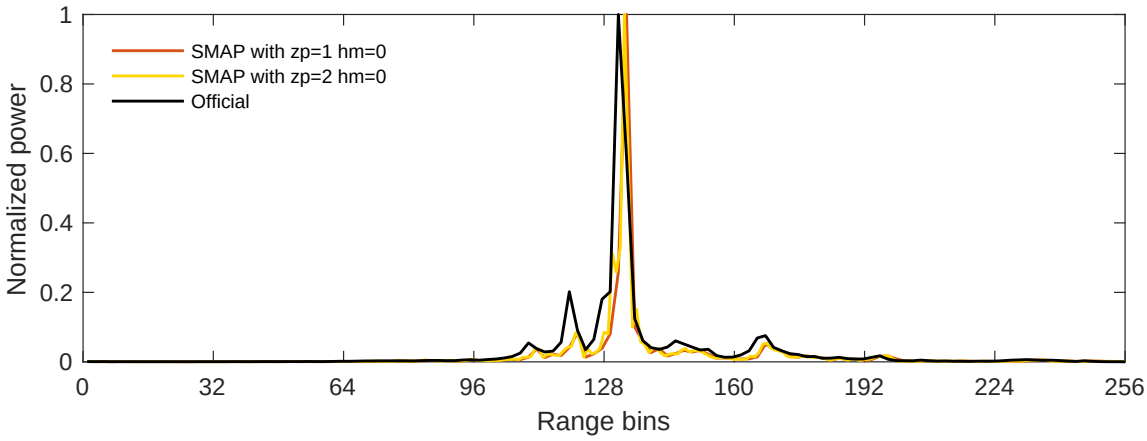

Figure 4.49: *SMAP Waveform With and Without Zero Padding of Point 1 from Mississippi*

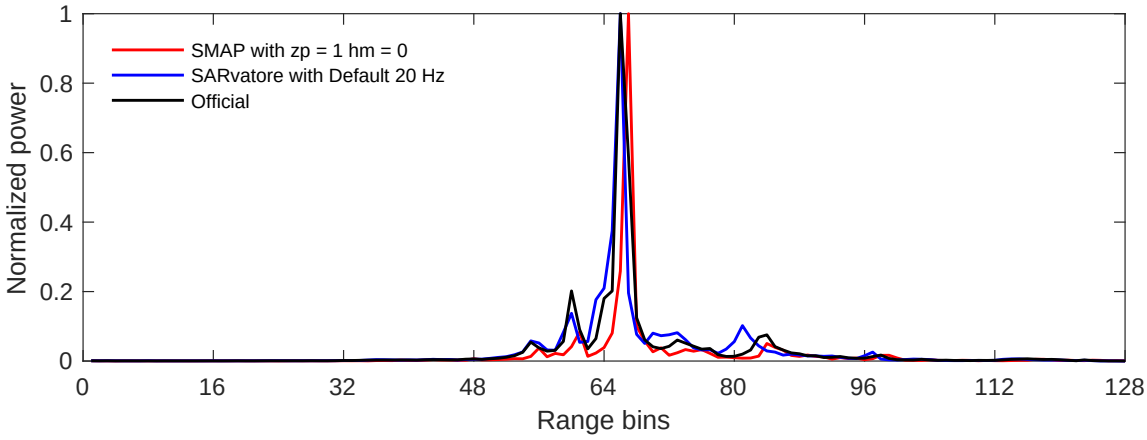

Figure 4.50: *SARvatore Waveform versus SMAP Waveform of Point 1 from Mississippi*

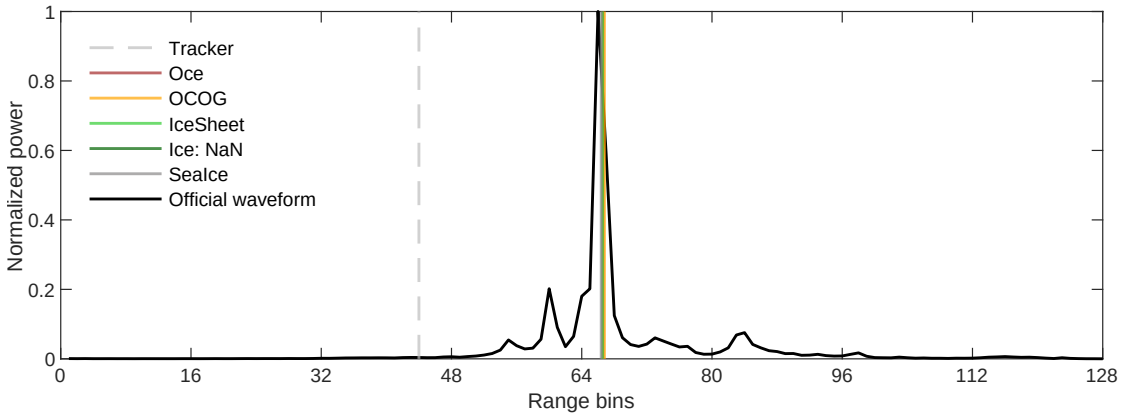

Figure 4.51: *Retracking for Official Waveform of Point 1 from Mississippi*

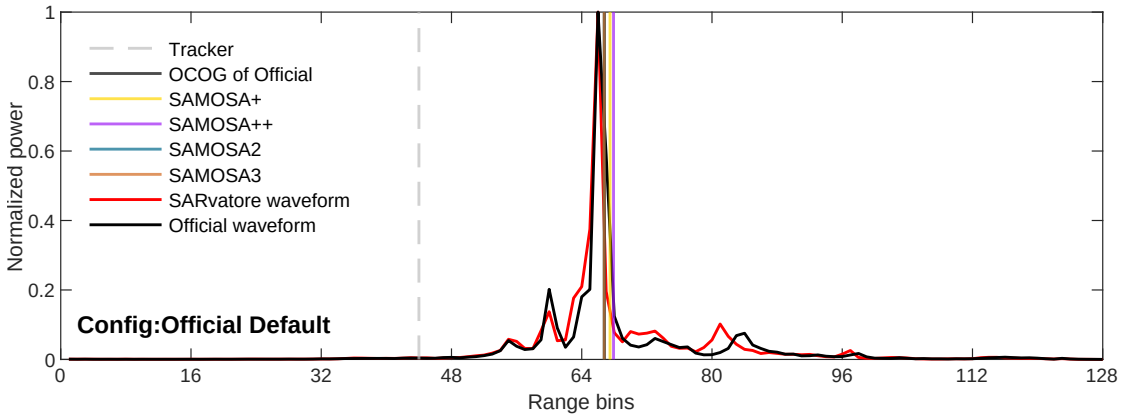

Figure 4.52: *Retracking for SARvatore Waveform of Point 1 from Mississippi*

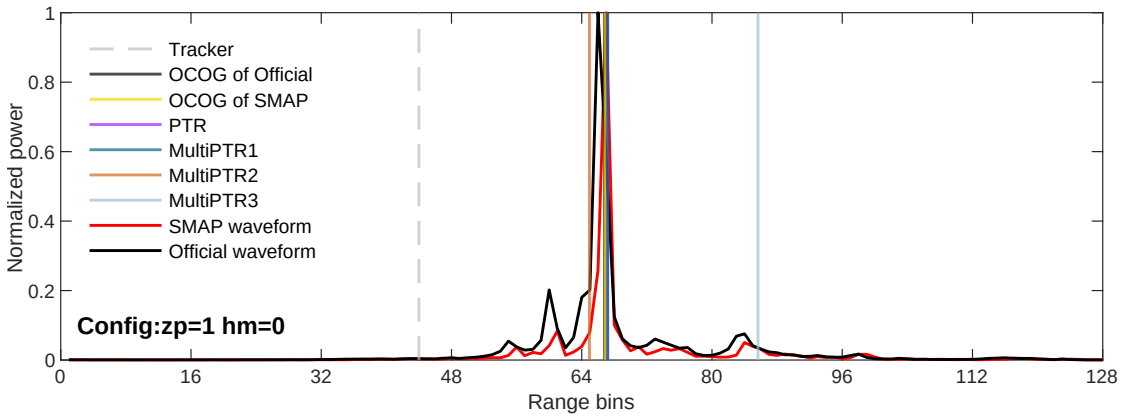

Figure 4.53: *Retracking for SMAP Waveform of Point 1 from Mississippi*

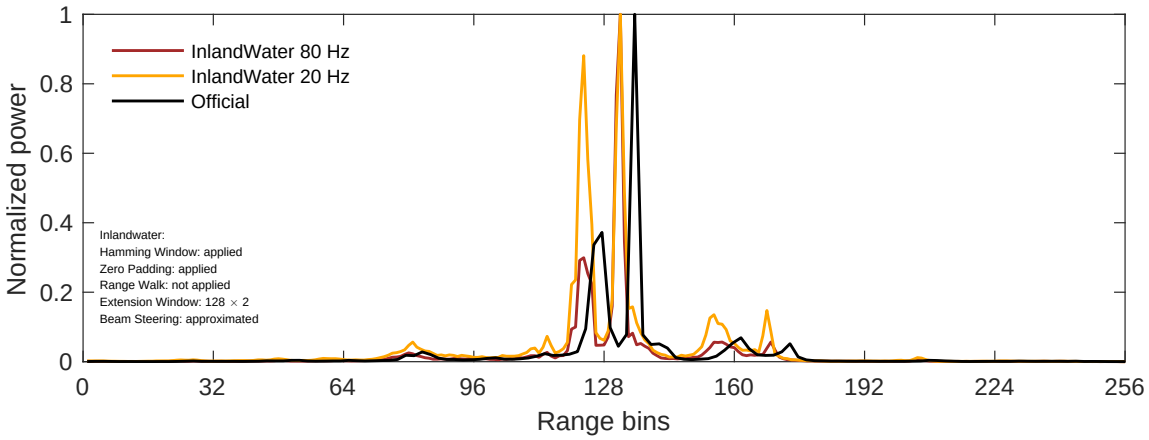

Figure 4.54: *SARvatore Waveform with Config Inlandwater of Point 2 from Mississippi*

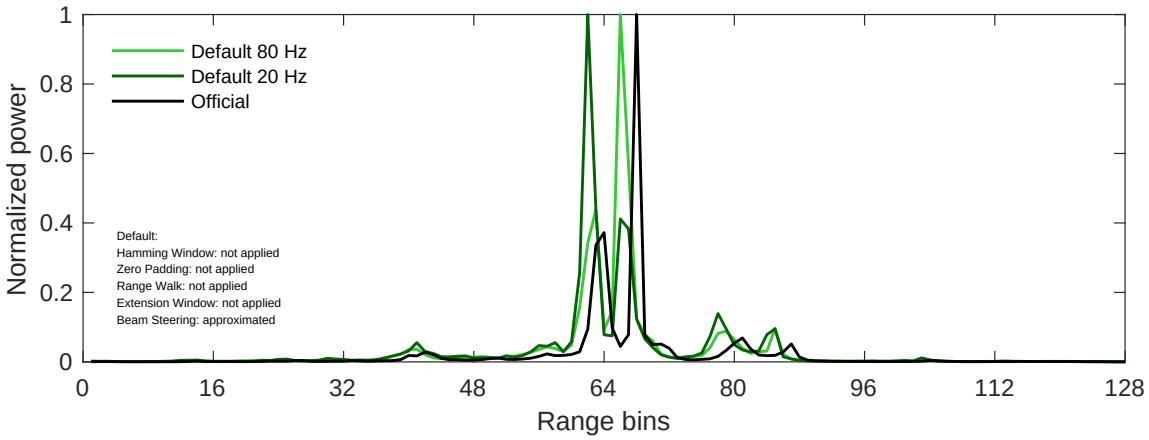

Figure 4.55: *SARvatore Waveform with Default Config of Official S3 Product of Point 2 from Mississippi*

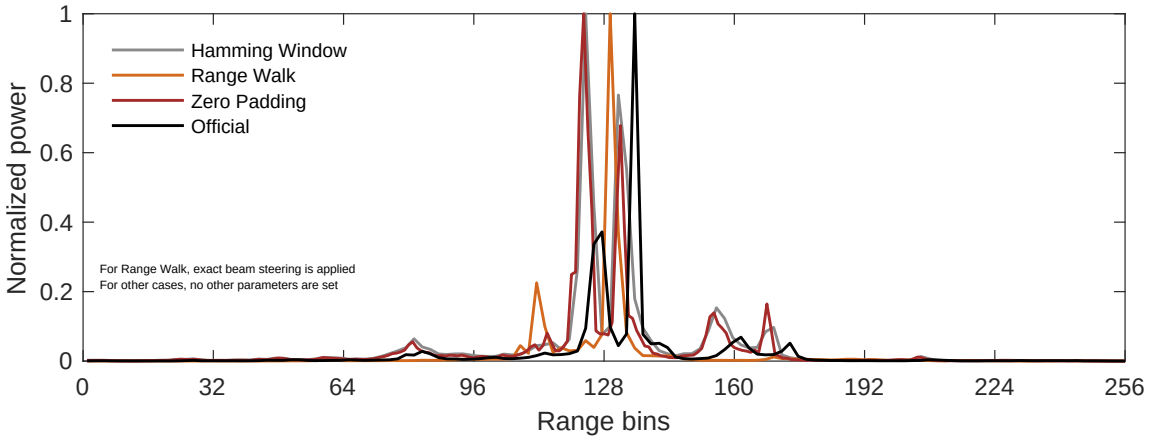

Figure 4.56: *SARvatore Waveform with Different Settings versus the Official Waveform of Point 2 from Mississippi*

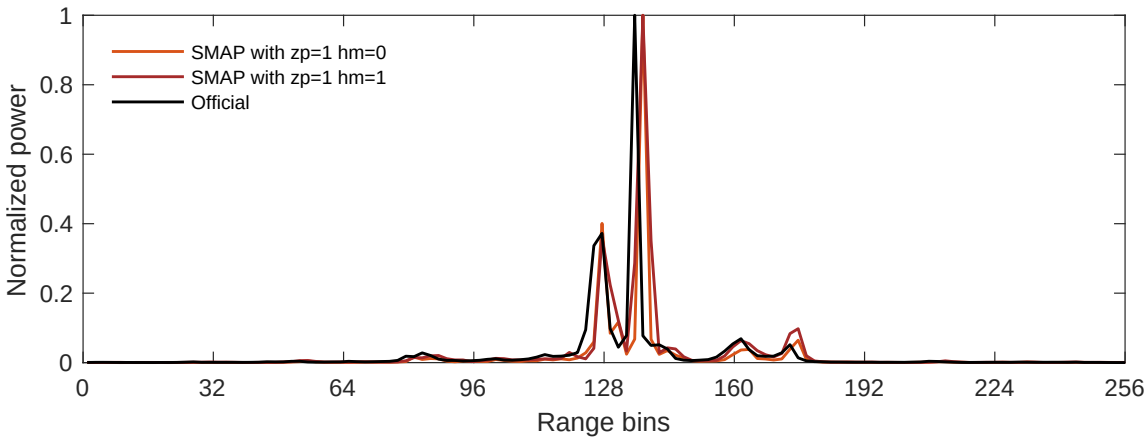

Figure 4.57: *SMAP Waveform With and Without Hamming Window of Point 2 from Mississippi*

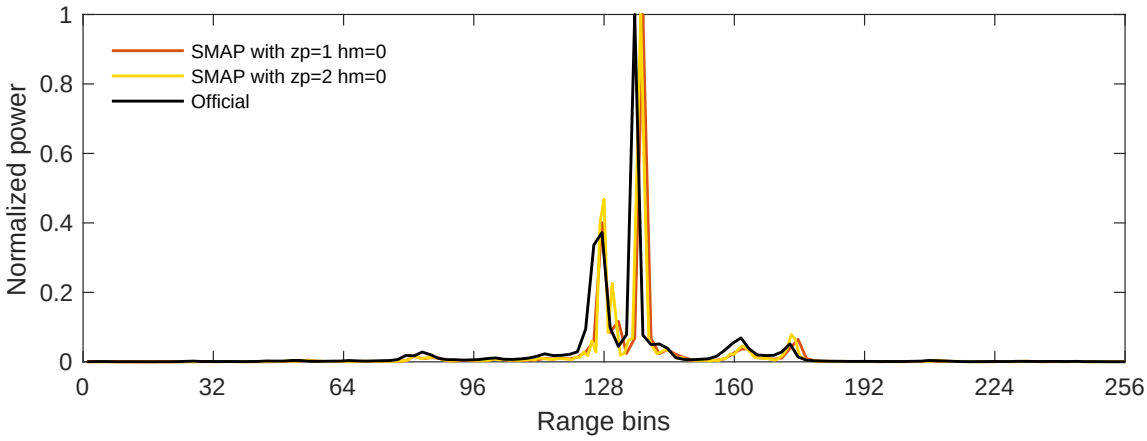

Figure 4.58: *SMAP Waveform With and Without Zero Padding of Point 2 from Mississippi*

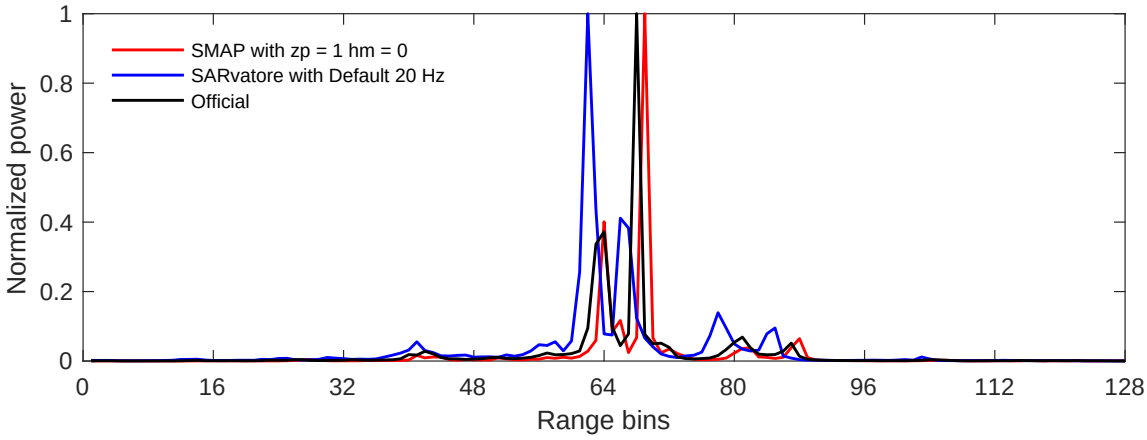

Figure 4.59: *SARvatore Waveform versus SMAP Waveform of Point 2 from Mississippi*

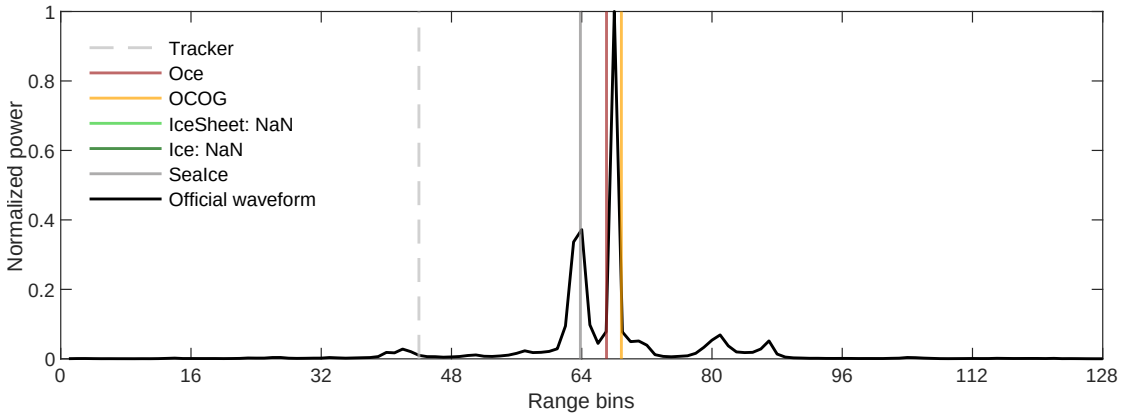

Figure 4.60: *Retracking for Official Waveform of Point 2 from Mississippi*

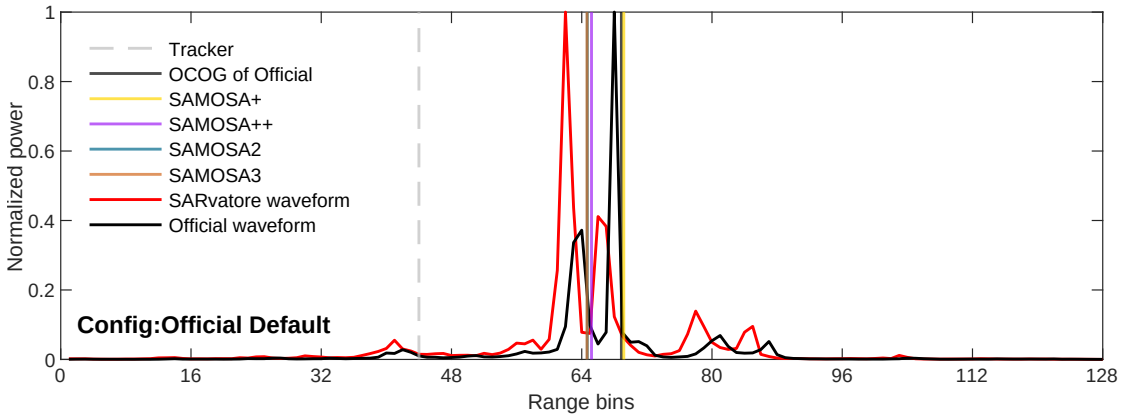

Figure 4.61: *Retracking for SARvatore Waveform of Point 2 from Mississippi*

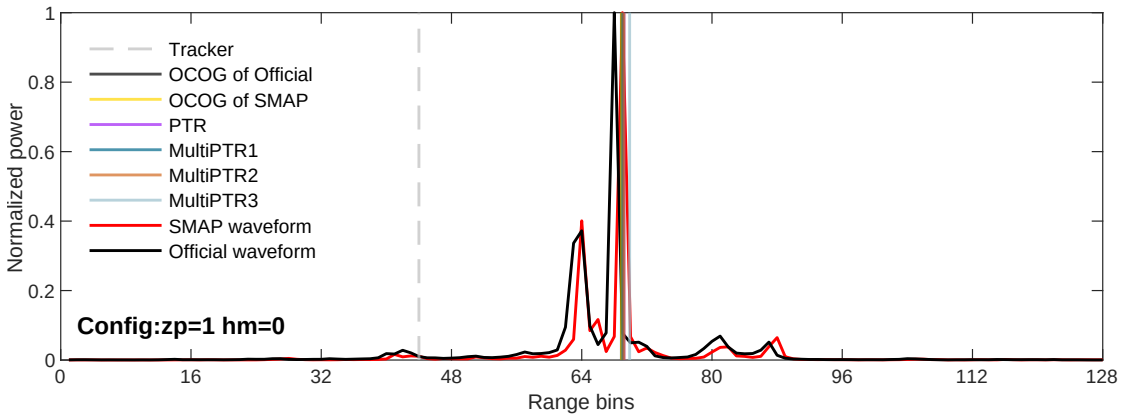

Figure 4.62: *Retracking for SMAP Waveform of Point 2 from Mississippi*

Two points in the river Mississippi are selected to represent their waveforms and retracker bins. The first point is located in the center of the river and the second point at coast area (see Figure 4.33). By comparing Figure 4.45 and Figure 4.54, it can be seen that the waveforms from water area and coast area are quite different. They both exhibit a small rise in front of the leading edge of the waveform; the difference however is that the rise of waveforms in the water area is relatively small, while the rise of waveform at coast area is relatively large. The result is that the retracker bins are pretty much the same in the first case. And in the second case, the retracker bins are much more different (see Figure 4.51 and Figure 4.60).

Figure 4.45 to Figure 4.46 represents the waveforms with different configurations for point 1. Except for Range Walk, all other configurations present the same peak position of the waveform. Unlike point 1, the waveforms of point 2 are all different from each other (see Figure 4.54 to see Figure 4.47). Figure 4.48, Figure 4.49, Figure 4.57 and Figure 4.58 show also the same peak position with differnt SMAP configurations for both point 1 and point 2.

4.3 São Francisco

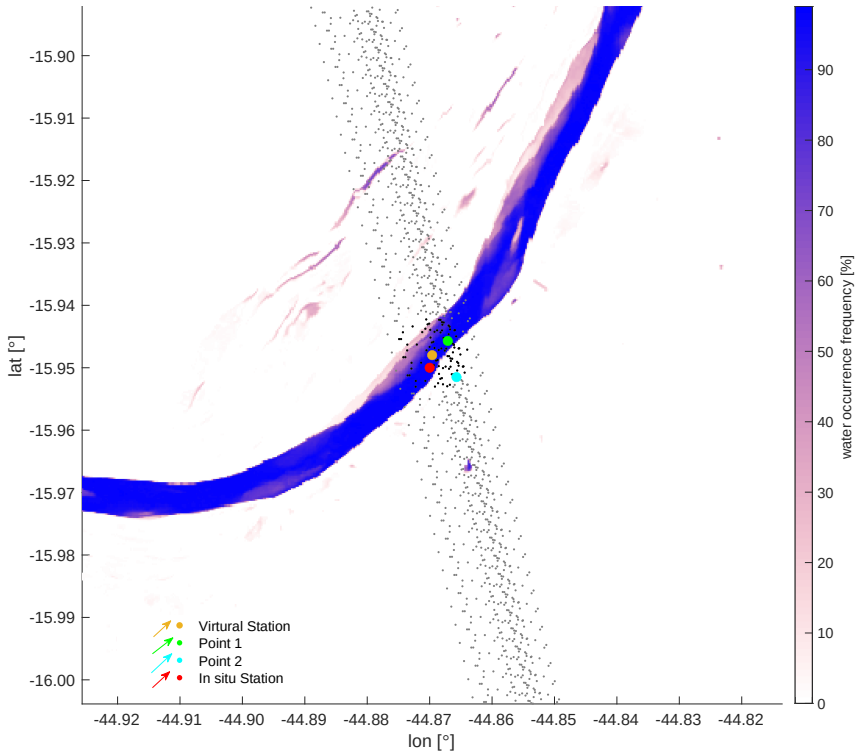

Figure 4.63: *Location of São Francisco*

For São Francisco, the water level time series of São Francisco are from November 2018 to April 2019. Figure 4.64 indicates that the results of SARvatore with different retrackers but same configuration InlandWater 80 Hz are quite comparable most of times. For the second and the forth point after 2019, the results and in situ data are roughly 0.5 m apart, while in the other four months, the results and in situ data are nearly identical. Figure 4.65 demonstrates the result from configuration of Range Walk differs from other configurations. And in case of SMAP, Figure 4.66 reveals that the results of retracker MultiPTR2 and MultiPTR3 are pretty poor compared to other retrackers unter the configuraiton with zero padding and hamming window. And Figure 4.67 indicates the results of different configurations under same retracker OCOG are fairly similar, and same as Figure 4.64, the results differ from the in situ data by roughly 0.5 m for the second and the forth point after 2019. Figure 4.68 represents the comparison between SARvatore and SMAP. It can be seen that overall SMAP results are not as impressive as SARvatore, but in April 2019 provides with the result more close to in situ data.

Figure 4.69 to 4.71 demonstrate the statistics of water level time series. For SARvatore, the results of configuration Range Walk with different retrackers are not comparable to other results. For SMAP, as can be seen from the statistics, the difference between the results of MultiPTR2 and MultiPTR3 is extremely high. The best performer comes from MultiPTR3 with configuration with zero padding but without hamming window, while other three configurations provides the worst results in terms of Bias, RMSE and correlation. Figure 4.72, Figure 4.73 and Figure 4.74 show the along track profiles of São Francisco.

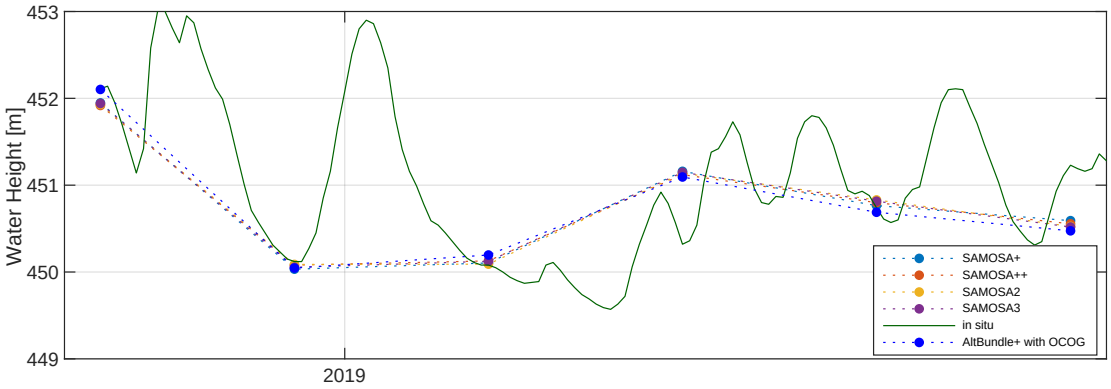

Figure 4.64: *SARvatore with Different Retrackers (Config-Inlandwater 80 Hz) of São Francisco*

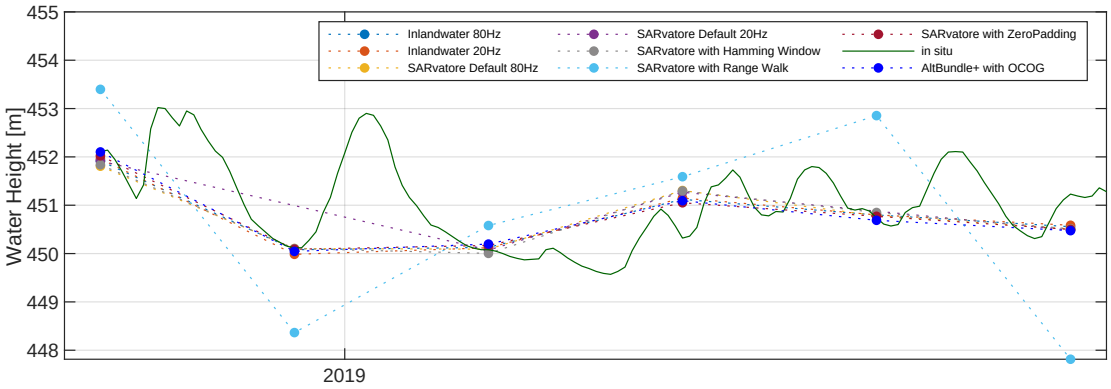

Figure 4.65: *SARvatore with Different Configs (Retracker-SAMOSA++) of São Francisco*

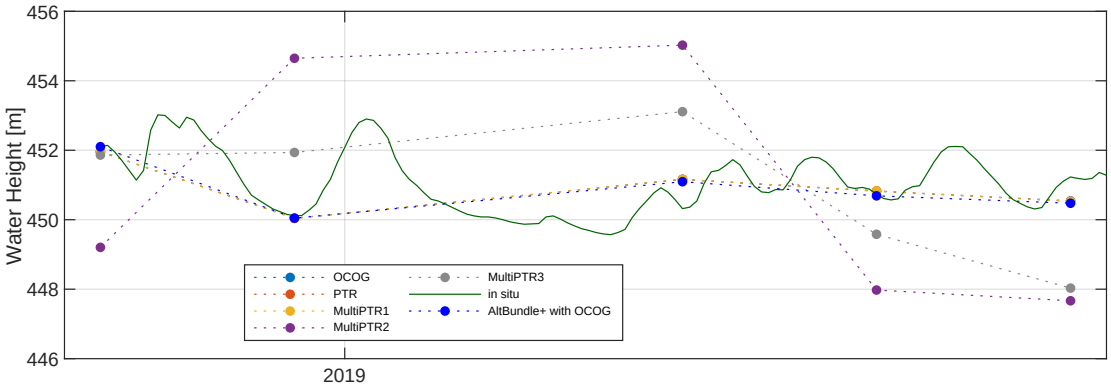

Figure 4.66: *SMAP-FFSAR with Different Retrackers but Same Config zp=2 hm=1 of São Francisco*

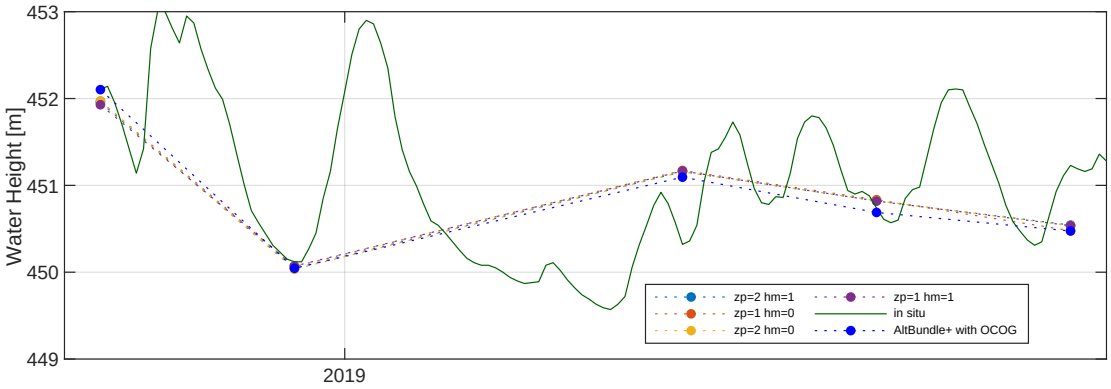

Figure 4.67: *SMAP-FFSAR with Different Configs and Same Retracker OCOG of São Francisco*

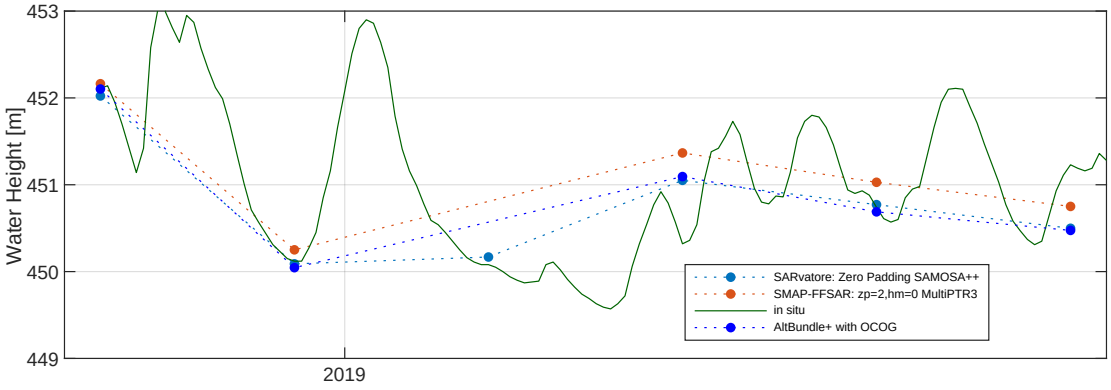

Figure 4.68: *SARvatore versus SMAP of São Francisco*

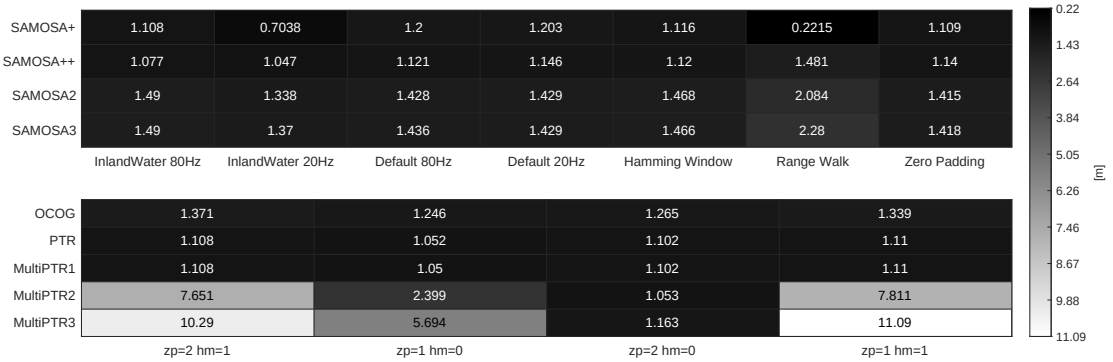

Figure 4.69: *Bias[m] with Different Configs and Different Retrackers of São Francisco (with Official OCOG* 0.4642 *m)*

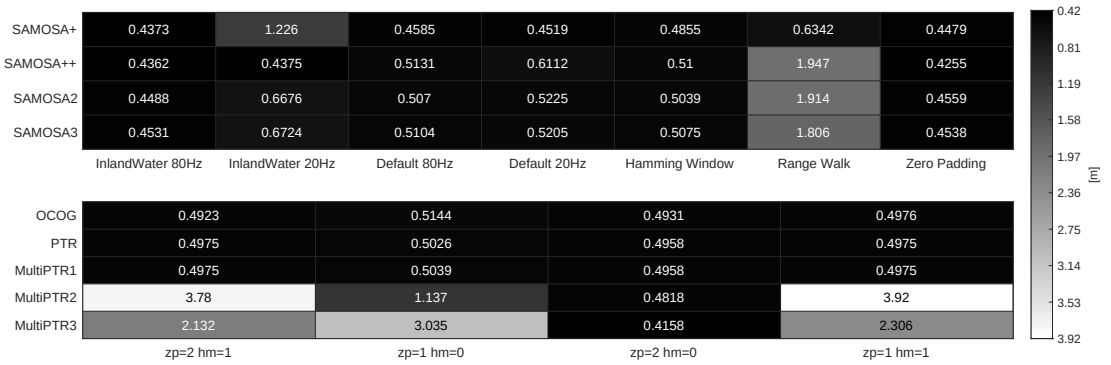

Figure 4.70: *RMSE[m] with Different Configs and Different Retrackers of São Francisco (with Official OCOG* 1.2426 *m)*

Figure 4.71: *Correlation of In situ Data with Different Configs and Different Retrackers of São Francisco (with Official OCOG* 0.9332*)*

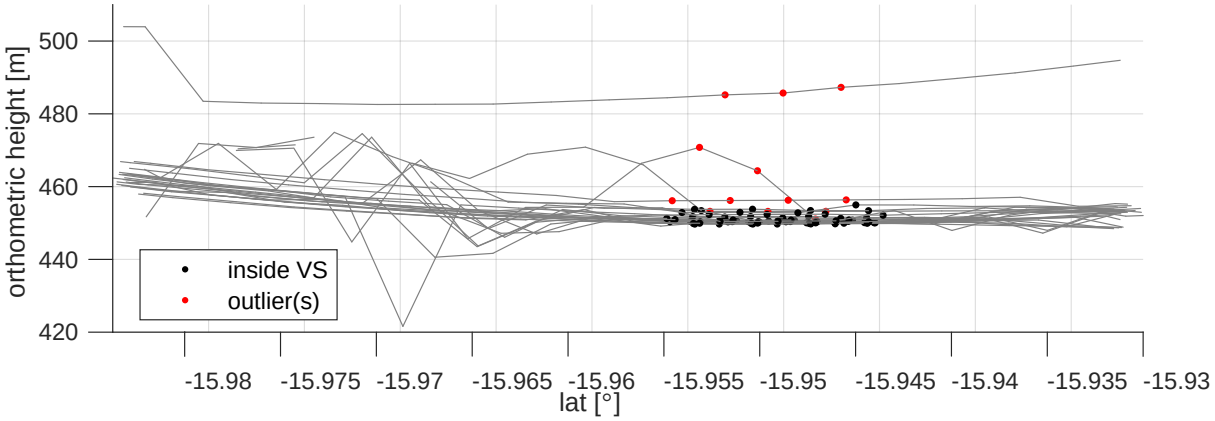

Figure 4.72: *Along Track Profile of São Francisco with Official Product (Retracker: OCOG)*

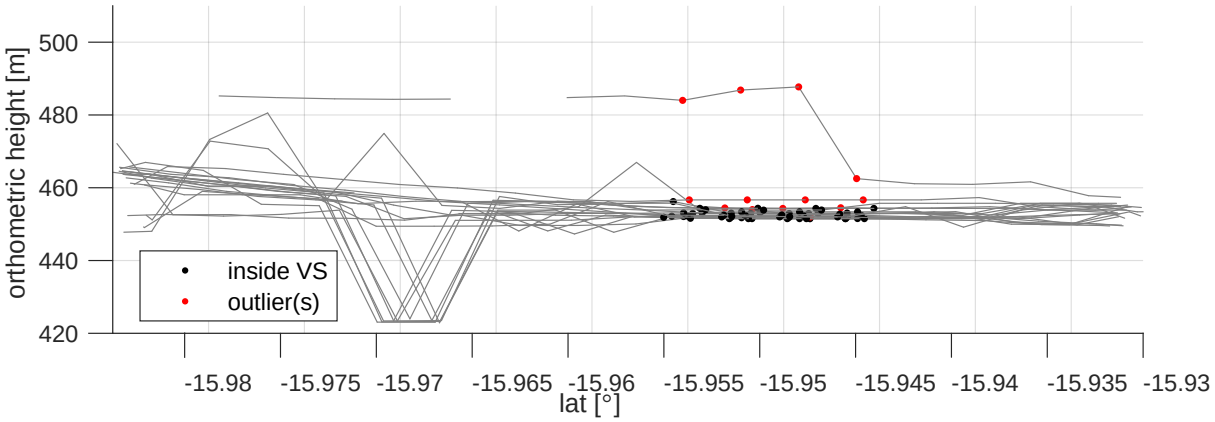

Figure 4.73: *Along Track Profile of São Francisco with SARvatore (Config: Default 20 Hz with SAMOSA++)*

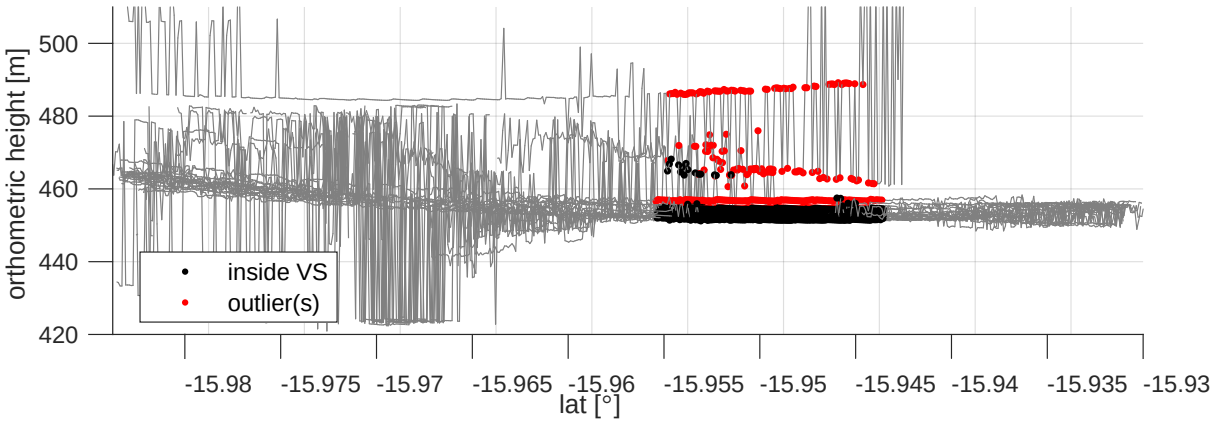

Figure 4.74: *Along Track Profile of São Francisco with SMAP (Config: zp=1, hm=0 with OCOG)*

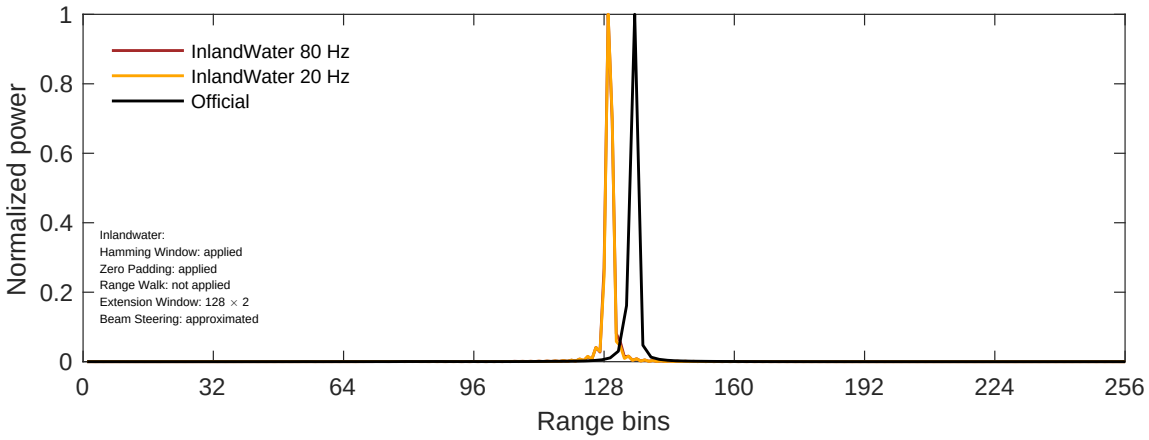

Figure 4.75: *SARvatore Waveform with Config Inlandwater of Point 1 from São Francisco*

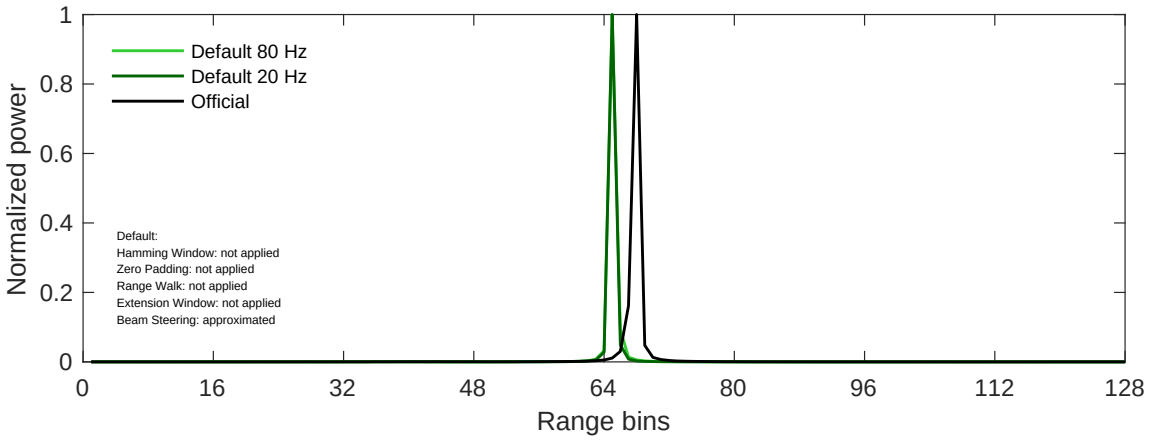

Figure 4.76: *SARvatore Waveform with Default Config of Official S3 Product of Point 1 from São Francisco*

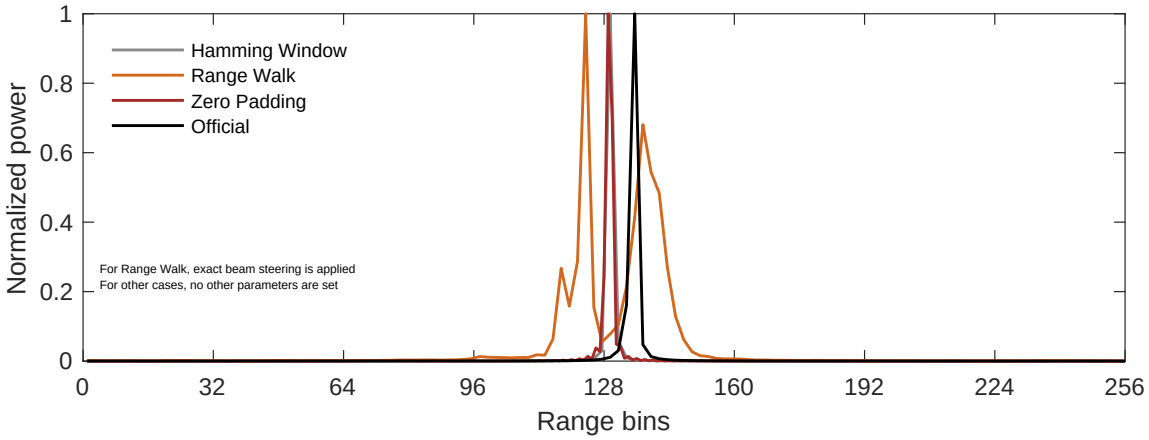

Figure 4.77: *SARvatore Waveform with Different Settings versus the Official Waveform of Point 1 from São Francisco*

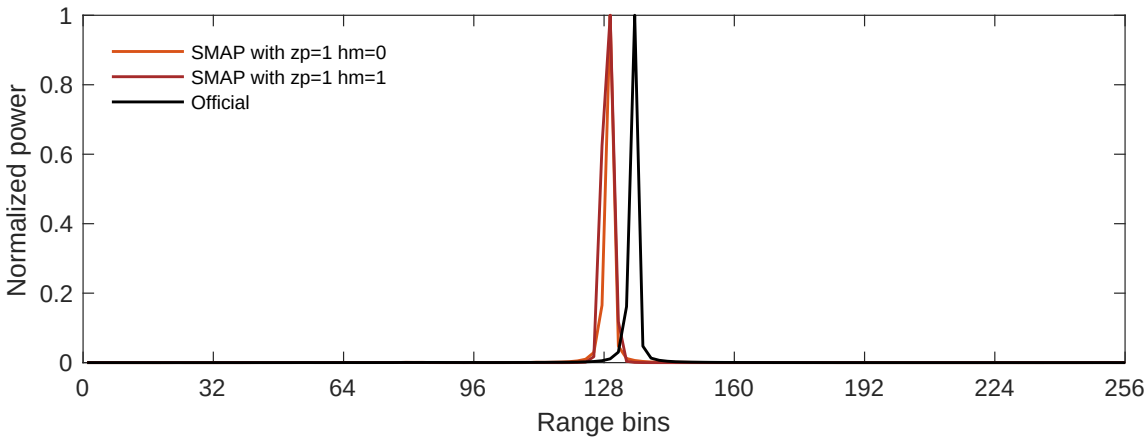

Figure 4.78: *SMAP Waveform With and Without Hamming Window of Point 1 from São Francisco*

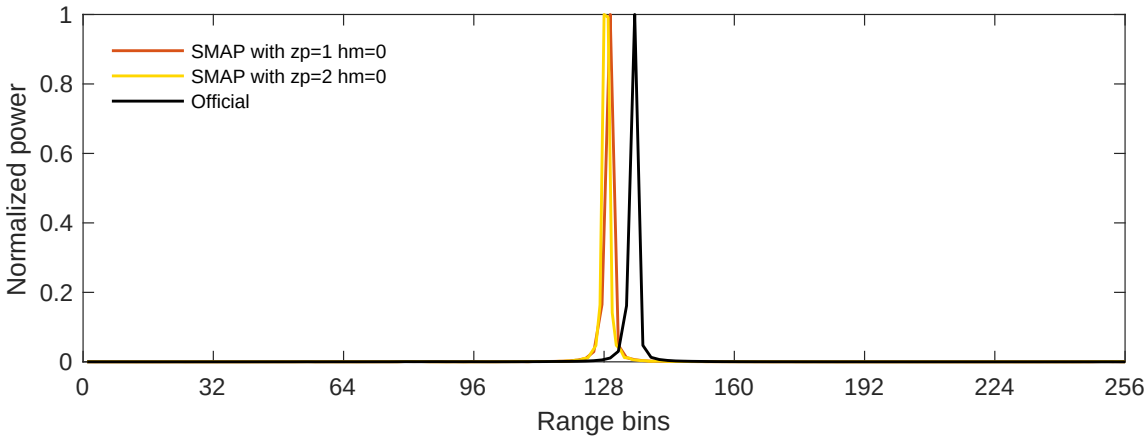

Figure 4.79: *SMAP Waveform With and Without Zero Padding of Point 1 from São Francisco*

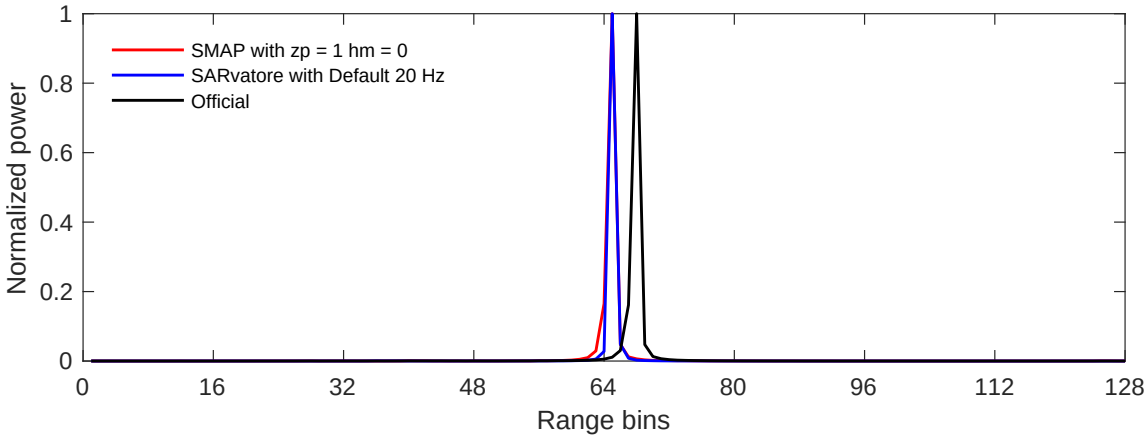

Figure 4.80: *SARvatore Waveform versus SMAP Waveform of Point 1 from São Francisco*

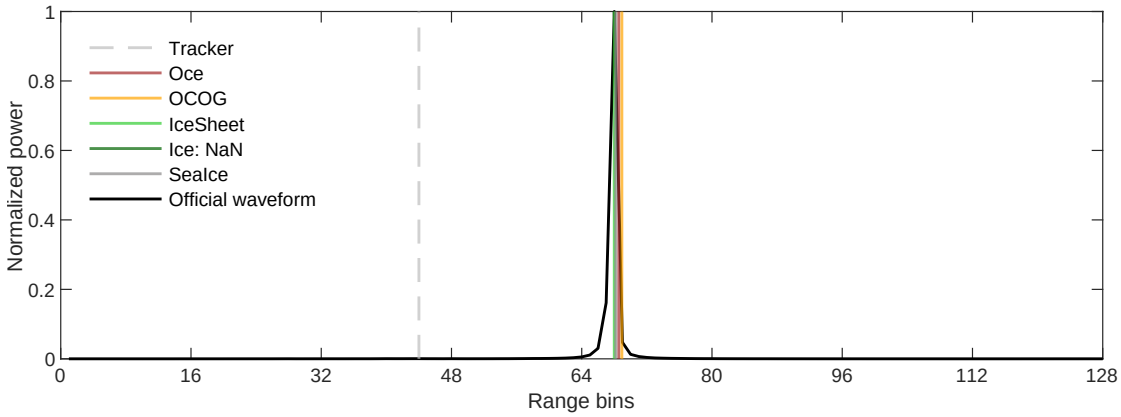

Figure 4.81: *Retracking for Official Waveform of Point 1 from São Francisco*

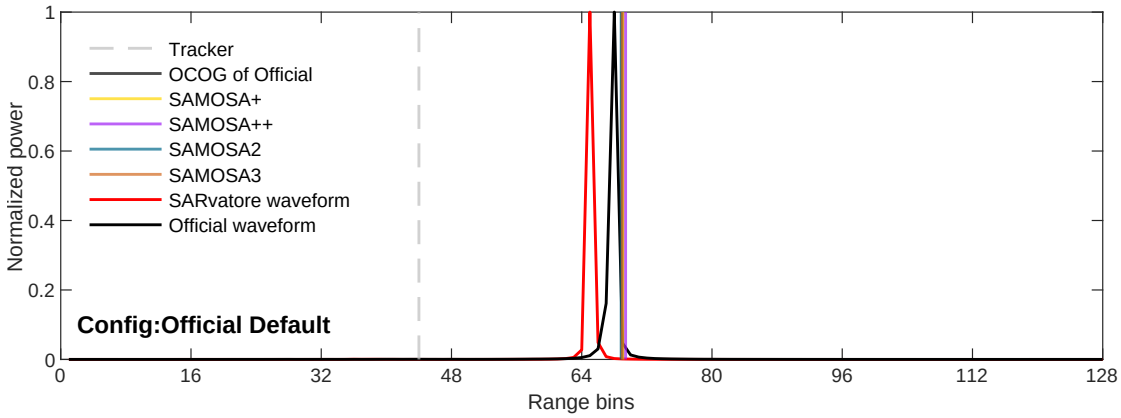

Figure 4.82: *Retracking for SARvatore Waveform of Point 1 from São Francisco*

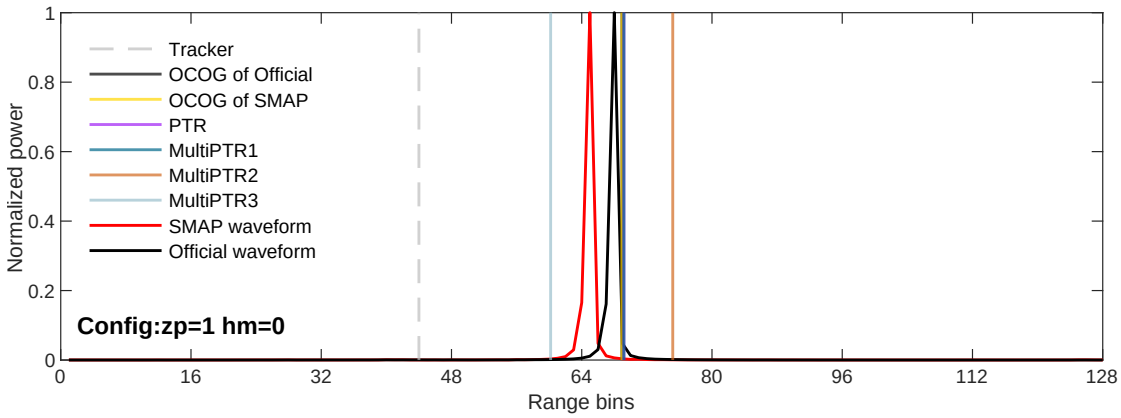

Figure 4.83: *Retracking for SMAP Waveform of Point 1 from São Francisco*

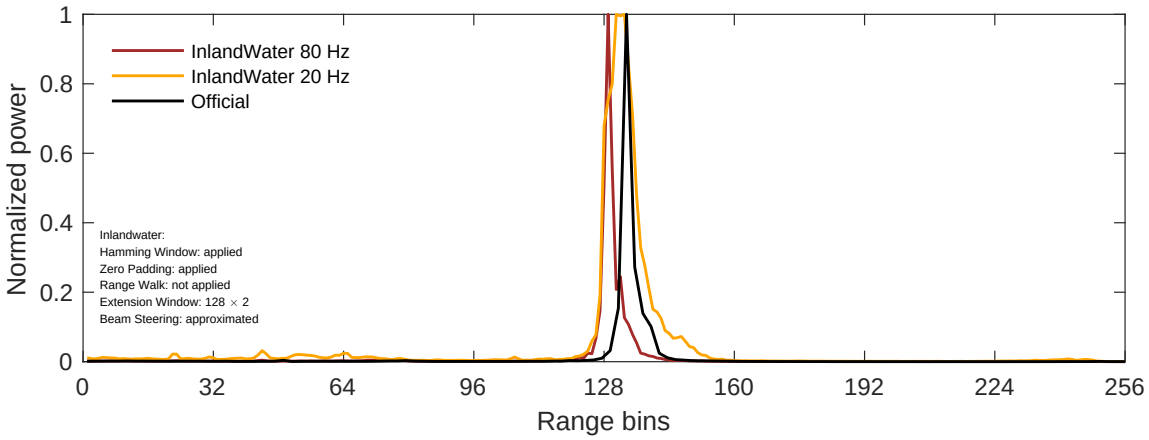

Figure 4.84: *SARvatore Waveform with Config Inlandwater of Point 2 from São Francisco*

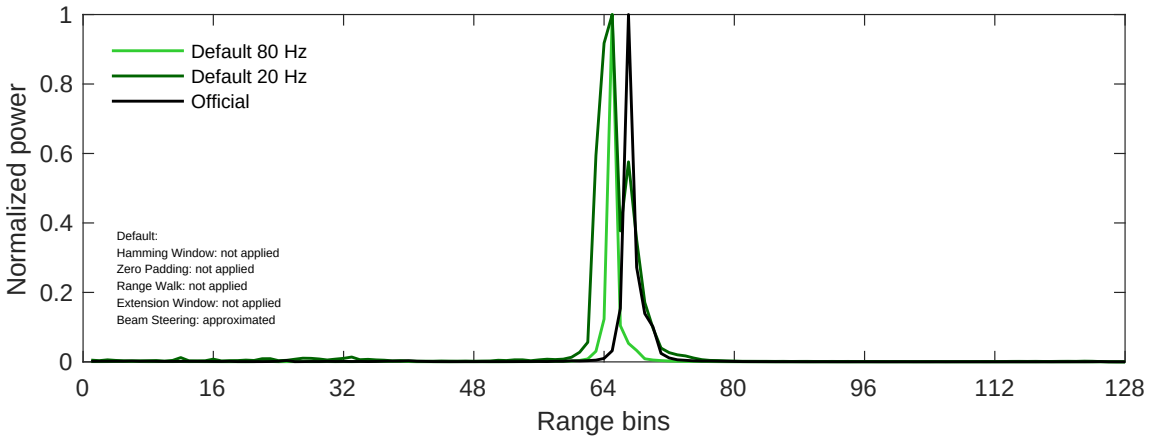

Figure 4.85: *SARvatore Waveform with Default Config of Official S3 Product of Point 2 from São Francisco*

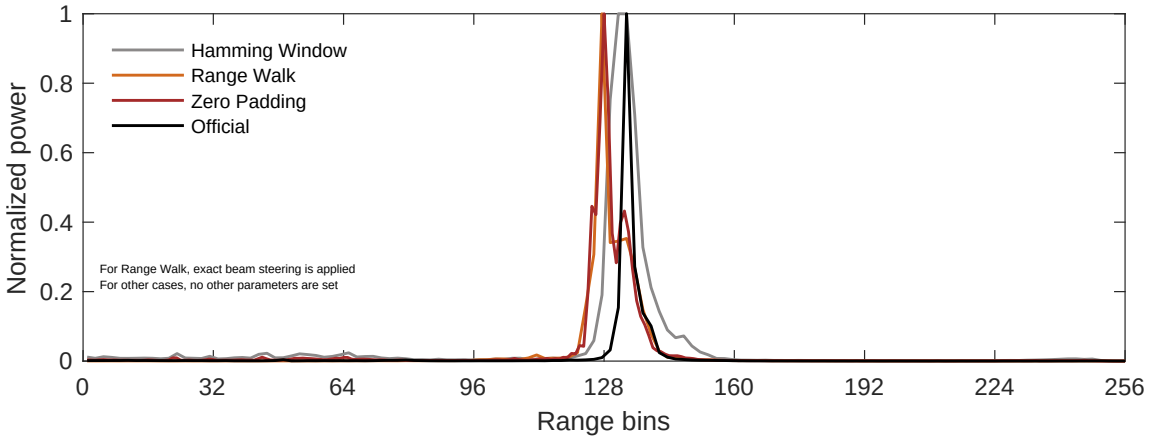

Figure 4.86: *SARvatore Waveform with Different Settings versus the Official Waveform of Point 2 from São Francisco*

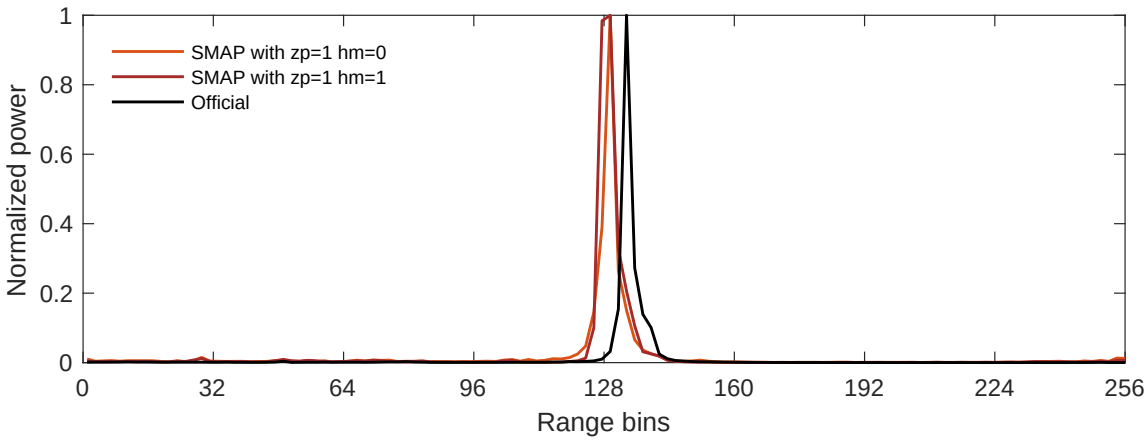

Figure 4.87: *SMAP Waveform With and Without Hamming Window of Point 2 from São Francisco*

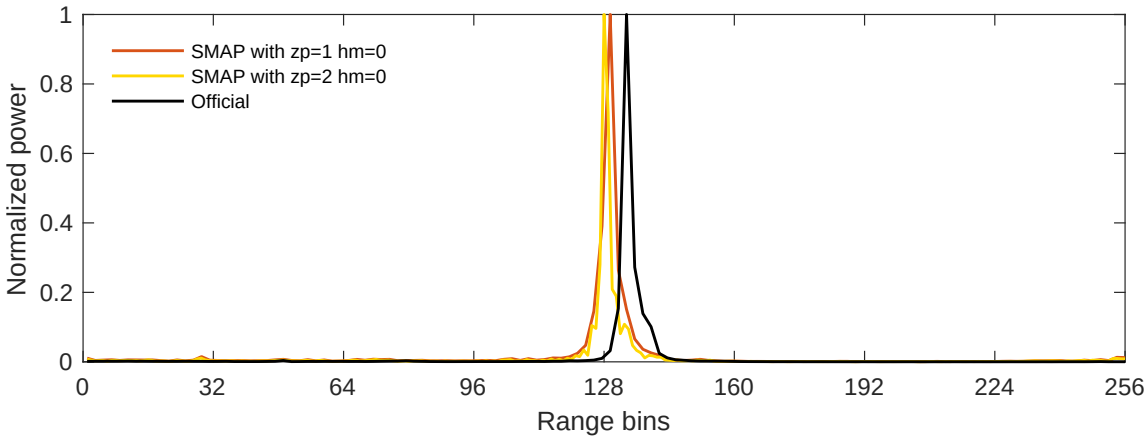

Figure 4.88: *SMAP Waveform With and Without Zero Padding of Point 2 from São Francisco*

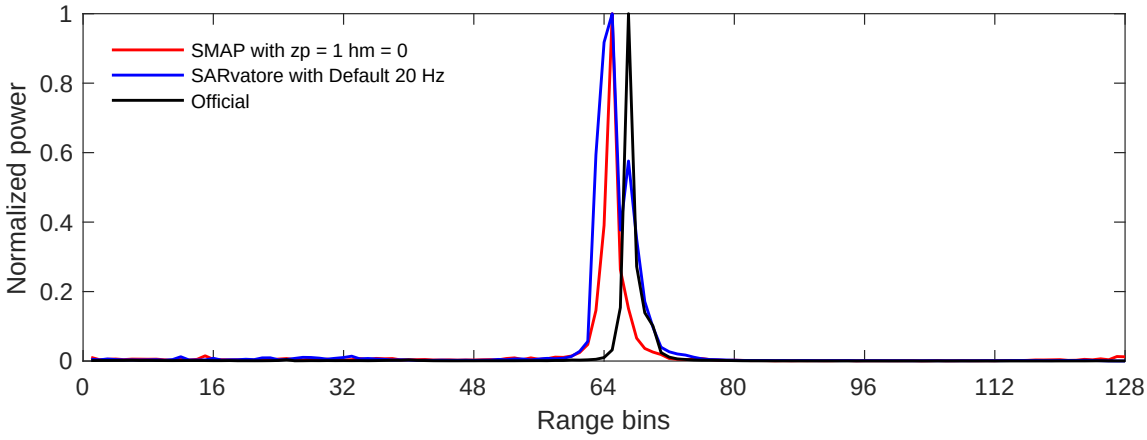

Figure 4.89: *SARvatore Waveform versus SMAP Waveform of Point 2 from São Francisco*

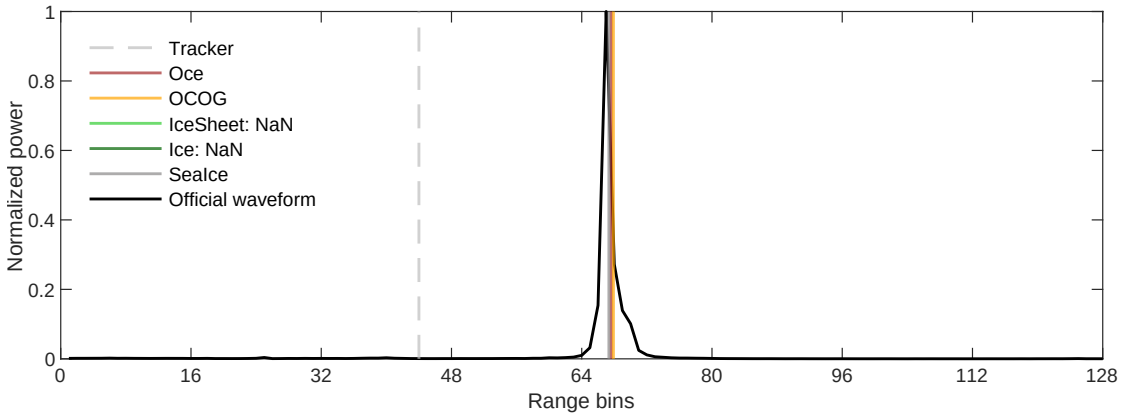

Figure 4.90: *Retracking for Official Waveform of Point 2 from São Francisco*

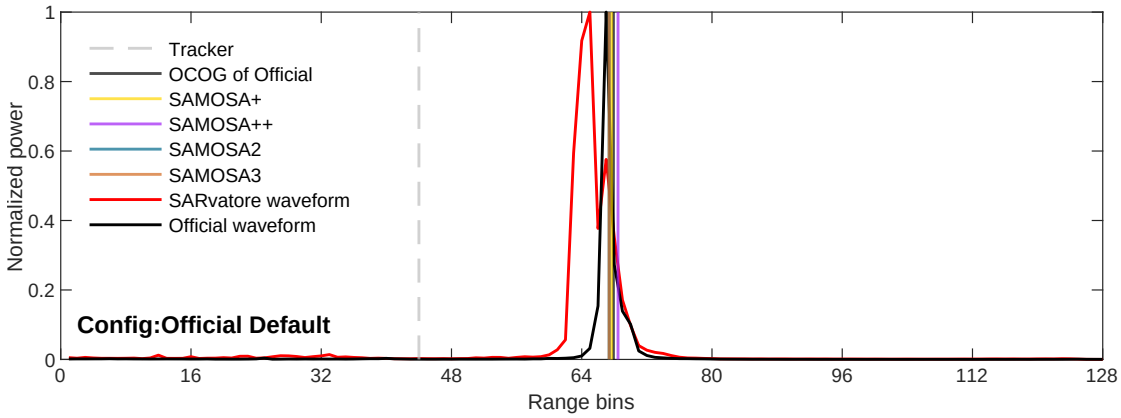

Figure 4.91: *Retracking for SARvatore Waveform of Point 2 from São Francisco*

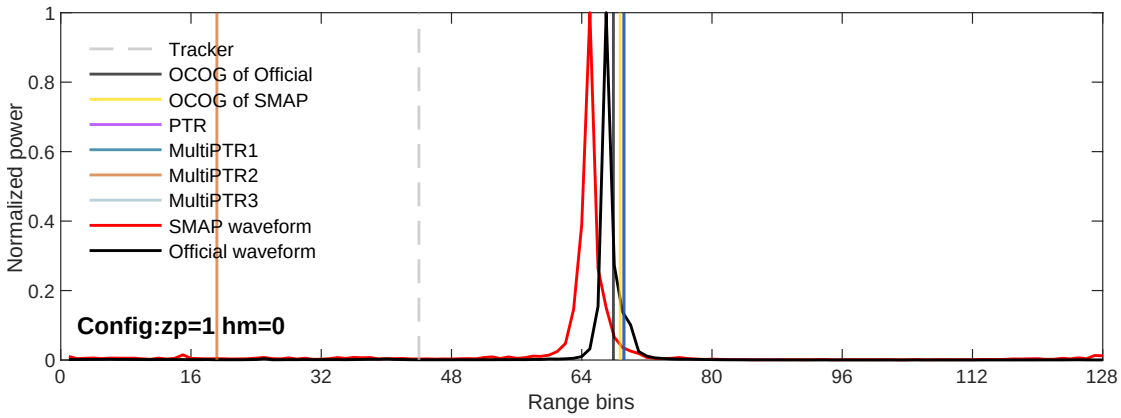

Figure 4.92: *Retracking for SMAP Waveform of Point 2 from São Francisco*

For São Francisco, two points are selected to present their waveforms and retracker bins (see Figure 4.63). Same as for Mississippi, one point in the water area and the other one at coast area. The waveforms produced by the two points of the Mississippi river are not quite similar, and in the case of the São Francisco, the waveforms of the two points are essentially the same (See Figure 4.80 and Figure 4.89). For point 1, the waveforms generated by 80 Hz or 20 Hz have no difference (see Figure 4.75 and Figure 4.76), while the peaks of waveforms of point 2 vary in Figure 4.84 and Figure 4.85. Same as the first two case studies, the generated waveforms from SMAP show no significant difference (see Figure 4.78, Figure 4.79, Figure 4.87 and Figure 4.88). From Figure 4.80 and Figure 4.89 it can be seen that the peaks of waveforms of SARvatore and SMAP are at same location.

For retracker bins, it is apparent that the official product preforms better than SARvatore and SMAP. For both SARvatore and SMAP, all retracker bins are at least 4 bins away from their own peaks, which is more in line with the official product waveform (see Figure 4.81 to Figure 4.83 and Figure 4.90 to Figure 4.92).

Chapter 5

Conclusion

With the development of the satelite altimetry, the measurement principle has evolved from the pulse-limited concept to the now widely applied delay-Doppler principle. Now, the altimetry community is more focused on the improvement of processing steps and the using of fully-focused SAR to obtain more precise results for inland areas. This thesis reviewed the general steps of Level-1B processing and retracking methods for Level-2. Different processing steps of Level-1B and different retracking methods of Level-2 yield different waveforms, retrackings, and therefore, water level estimations.

To study the influence of these configurations, two applications are used in this thesis, which are SARvatore for delay-Doppler altimetry and SMAP for fully-focused SAR. Furthermore, both applications can employ different retracking methods. With Sentinel-3 data, the water level time series, waveforms and retracker bins of three case studies are considered for comparison.

Our results reveal that the situation in inland areas is much more complicated than expected. For SARvatore, in most examples, the waveforms generated by the 80 Hz and 20 Hz configurations are similar, so the difference in water level comes mainly from the application of different retracking methods. In various configurations, Inland Water 80 Hz configuration performs relatively consistently, with decent results in all three case studies. Compared to the Hamming window and zero padding, the range walk exhibits a significant difference in RMSE in the various locations with different retrackers; For river Mississippi and river São Francisco, the difference between the best and worst results is more than 0.5 m. Moreover, the waveforms of the range walk are quite different from the waveforms produced by the other configurations. As for SAMOSA retrackers, sometimes the same retracker bins are given (see Figure 4.22), and on other occasions the results given differ by four bins (see Figure 4.61). In terms of water level time series, the best performers are obtained by SAOMSA+ under Inland Water 80 Hz.

Although the along-track resolution was increased from 300 m to 13 m through the application of SMAP, the results did not improve significantly, and in some cases, were not even as useful as the ones from SARvatore and official products. For SMAP, the different configurations —specifically, with or without zero padding or the Hamming window—had very little impact, with more differences mainly coming from the different retracking methods. As for SMAP's retracking method, it is difficult to conclude which one performs best. In the study, it even appeared that the best-performing retracker (MutliPTR3) for the water level time series at the first location performed the worst at the second case study.

In summary, the following conclusions can be drawn:
- Different configurations and retracking methods can significantly affect the shape of waveforms and their derived range.
- According to this study's experiments, Inland Water 80 Hz with SAMOSA++ offers the best performance
- Our results show that FF-SAR does not bring a significant improvement when applied to Sentinel-3 data.

With the commissioning of Sentinel-6 Michael Freilich, researchers can expect the data to be used in the future for FF-SAR and to present better results than those of Sentinel-3.

It is suggested that more effort be devoted to investigating the internal algorithms of the Level-1B processing and the reatracking, especially SMAP retrackers, as the community is less familiar with them. Doing so will allow a clearer interpretation of the generated waveforms under different configurations can be given.

Bibliography

bitweenie [2021], https://www.bitweenie.com/listings/fft-zero-padding/.

Bouzinac, C., ESA, UCL, ACS, ARESYS and Exprivia [2019], 'CryoSat-2 Product Handbook Baseline D 1.1'.

Brown, G. [1977], 'The average impulse response of a rough surface and its applications', *IEEE Transactions on Antennas and Propagation* **25**(1), 67–74.

Caputi, W. J. [1971], 'Stretch: A Time-Transformation Technique', *IEEE Transactions on Aerospace and Electronic Systems* **AES-7**(2), 269–278.

Cotton, D., Andersen, O., Cipollini, P., Gommenginger, C., Quartly, G., Martin, C., Marquez, J. and Moreno, L. [2008], 'Development of SAR Altimetry Mode Studies and Applications over Ocean, Coastal Zones', p. 13.

Cumming, I. G. and Wong, F. H. [2005], *Digital Processing of Synthetic Aperture Radar Data*, Artech House.

DeDop User manual [2021], https://dedop-core.readthedocs.io/en/latest/introduction.html.

Deng, X. and of Technology. Dept. of Spatial Sciences, C. U. [2003], *Improvement of Geodetic Parameter Estimation in Coastal Regions from Satellite Radar Altimetry*, Curtin University of Technology.
URL: *https://books.google.de/books?id=1AtjYgEACAAJ*

Dinardo, S. [2020], Techniques and Applications for Satellite SAR Altimetry over water, land and ice, PhD thesis, Technische Universität, Darmstadt.
URL: *http://tuprints.ulb.tu-darmstadt.de/11343/*

Dinardo, S., Fenoglio-Marc, L., Buchhaupt, C., Becker, M., Scharroo, R., Joana Fernandes, M. and Benveniste, J. [2018], 'Coastal SAR and PLRM altimetry in German Bight and West Baltic Sea', *Advances in Space Research* **62**(6), 1371–1404. The CryoSat Satellite Altimetry Mission: Eight Years of Scientific Exploitation.
URL: *https://www.sciencedirect.com/science/article/pii/S0273117717308943*

Donlon, C. J., Cullen, R., Giulicchi, L., Vuilleumier, P., Francis, C. R. and et al. [2021], 'The Copernicus Sentinel-6 mission: Enhanced continuity of satellite sea level measurements from space', *Remote Sensing of Environment* **258**, 112395.
URL: *https://www.sciencedirect.com/science/article/pii/S0034425721001139*

earth online —ESA [2021], https://earth.esa.int/eogateway/missions/cryosat.

Egido, A. and Smith, W. H. F. [2017], 'Fully Focused SAR Altimetry: Theory and Applications', *IEEE Transactions on Geoscience and Remote Sensing* **55**(1), 392–406.

ESA [2012], 'Sentinel-3: ESA's Global Land and Ocean Mission for GMES Operational Services'.

Gleason, S. [2006], 'Detecting Bistatically Reflected GPS Signals from Low Earth Orbit Over Land Surfaces', pp. 3086 – 3089.

GPOD User manual [2021], https://wiki.services.eoportal.org/tiki-index.php?page=GPOD+SENTINEL-3+SARvatore+Software+Prototype+User+Manual.

Ilioudis, C. [2021], 'Introduction to radar signal processing', https://udrc.eng.ed.ac.uk/sites/udrc.eng.ed.ac.uk/files/attachments/Introduction%20Radar%20signal%20processing.pdf.

Makhoul-Varona, E., Martin, F., Naeije, M. and Cotton, P. [2020], 'SAR Altimetry Coastal and Open Ocean Performance - Algorithm Theoretical Basis Document (ATBD), D1.3'.

Melo, G., Sobral, M. and Gunkel, G. [2016], *Water Quality Study of the Itaparica Reservoir, SÃ£o Francisco River, Brazil*.

MSSL, UCL and CLS [2019], 'Sentinel-3 Level 2 SRAL MWR Algorithm Theoretical Baseline Definition'.

Raney, R. [1998], 'The delay/Doppler radar altimeter', *IEEE Transactions on Geoscience and Remote Sensing* **36**(5), 1578–1588.

Ray, C., Martin-Puig, C., Clarizia, M. P., Ruffini, G., Dinardo, S., Gommenginger, C. and Benveniste, J. [2015], 'SAR Altimeter Backscattered Waveform Model', *IEEE Transactions on Geoscience and Remote Sensing* **53**(2), 911–919.

Scagliola, M., Recchia, L., Maestri, L. and Giudici, D. [2021], 'Evaluating the impact of range walk compensation in delay/Doppler processing over open ocean', *Advances in Space Research* **68**(2), 937–946. 25 Years of Progress in Radar Altimetry.
URL: *https://www.sciencedirect.com/science/article/pii/S0273117719308403*

Sentinel6 - ESA [2021], https://www.esa.int/Applications/Observing_the_Earth/Copernicus/Sentinel-6.

Sentinel Online —ESA [2021], https://sentinel.esa.int/web/sentinel/user-guides/sentinel-3-altimetry.

THE CEOS DATABASE [2021], http://database.eohandbook.com/database/missionsummary.aspx?missionID=579.

Tourain, C., Piras, F., Ollivier, A., Hauser, D., Poisson, J. C., Boy, F., Thibaut, P., Hermozo, L. and Tison, C. [2021], 'Benefits of the Adaptive Algorithm for Retracking Altimeter Nadir Echoes: Results From Simulations and CFOSAT/SWIM Observations', *IEEE Transactions on Geoscience and Remote Sensing* pp. 1–14.

Tourian, M. [2012], 'Controls on satellite altimetry over inland water surfaces for hydrological purposes'.